EARTHQUAKE CYCLE OF THE NORTH ANATOLIAN FAULT ALONG THE RUPTURE ZONE OF THE AUGUST 17, 1668 GREAT ANATOLIAN EARTHQUAKE

by

Sevil Cansu Yıldırım

B.S., Geomatic Engineering, Istanbul Technical University, 2018

Submitted to the Institute for Graduate Studies in
Science and Engineering in partial fulfillment of
the requirements for the degree of
Master of Science

Graduate Program in Geodesy

Boğaziçi University

2021

ACKNOWLEDGEMENTS

First of all, I would like to express my sincere gratitude and respect to Assoc. Prof. Fatih Bulut for all his support in my personal and academic life, his guidance during my research and his contributions to my education. I also would like to thank the members of my dissertation committee: Prof. Aslı Doğru and Prof. Cenk Yaltırak for spending their valuable time to evaluate my thesis.

This thesis is supported by the research project "Slip deficit along Major Seismic Gaps in Turkey" funded by Bogaziçi University (project number: 18T03SUP4).

I would like to thank each member of the Geodesy Department of the Kandilli Observatory and Earthquake Research Institute, Prof. Dr. Haluk Özener, Prof. Dr. Semih Ergintav, Asst. Prof. Tülay Eken, Asst. Prof. Mahyat Tehrany, Dr. Onur Yılmaz, for their valuable contributions. I am so grateful that I had the chance to be educated here and be a part of this department.

Special thanks go to my colleagues, Kaan Alper Uçan, Müfide Er Elvanlı and Yağızalp Okur for their helps and friendship.

I would like to express my deepest appriciation to my family for always being there to encourage and support me as I build who I am. I would like to thank my parents for their care and love, and my brother for everything he taught me through our lives, and for helping me with my schools.

I would also like to thank all of my very dear friends, but especially Alican Mutlusoy, for always taking care of me and my computer problems.

ABSTRACT

EARTHQUAKE CYCLE OF THE NORTH ANATOLIAN FAULT ALONG THE RUPTURE ZONE OF THE AUGUST 17, 1668 GREAT ANATOLIAN EARTHQUAKE

We investigated the earthquake cycle along the 450-km rupture zone of the August 17, 1668 Great Anatolian Earthquake (M8.1) combining GPS and earthquake data. We elaborated on elastic rebound theory investigating creeping and locked stages of the individual fault segments. We simultaneously estimated segment-based slip rates and locking depths. Slip rates are used to estimate preliminary inter-seismic slip storages assuming fully locked fault segments right after the mainshocks. Misfits between co-seismic slips and preliminary inter-seismic slip storages indicate that the fault does not store slip for a while after major earthquakes. Our analysis shows a partitioning between creeping and locked stages. Only along one segment, the 1943 M7.7 rupture, creep played a minor role during the seismic cycle (0.1%). Along the 1939 M7.9, 1957 M7.0, 1967 M7.2, and 1999 M7.5 ruptures, creep played a considerable role (16.9%, 22.2%, 17.9% and 22.4%, respectively). Along the 1942 M7.1, 1944 M7.4, 1999 M7.1 rupture zones, creep played a substantial role, and covered almost half of the seismic cycle (54.4%, 44.0% and 48.3%, respectively). The segments host currently different earthquake potentials as they have distinctive creeping/locking rates despite the fact that they are exposed to similar deformation rates (between 19.5±0.5 – 24.2±0.3 mm/y). Our results show that slip rates systematically accelerate from the east to the west. Failure of the NAFZ will probably end at the western segments within 239±3 years. The space-time pattern of the earthquakes during the last three complete and the current incomplete cycles confirms that the failure of the NAFZ starts from the east, and systematically migrate to the west deceleratingly.

ÖZET

17 AĞUSTOS 1668 BÜYÜK ANADOLU DEPREMİNİN KIRIĞI BOYUNCA KUZEY ANADOLU FAYININ DEPREM DÖNGÜSÜ

17 Ağustos 1668 Büyük Anadolu Depremi'nin (M8.1) 450-km kırılma zonu boyunca GPS ve deprem verilerini birleştirerek deprem döngüsünü inceledik. Bireysel fay segmentlerinin kayan (krip) ve kilitli aşamalarını elastik geri tepme teorisi ile ayrıntılı bir şekilde inceledik. Segment bazlı kayma oranlarını ve kilitleme derinliklerini eşzamanlı olarak tahmin ettik. Segmentlerin ana şoklardan hemen sonra tamamen kilitlendiğini varsayarak inter-sismik kayma birikmesini tahmin etmek için kayma oranlarını kullandık. Ko-sismik kayma ile biriken inter-sismik kayma arasındaki uyumsuzluklar, fayın büyük bir depremden sonra bir süre kaymayı biriktirmediğini göstermektedir. Analizimiz uzay-zamanda kayan ve kilitli kısımların bulunduğunu göstermiştir. Sadece bir segmentte, 1943 M7.7 kırığı, kayma sismik döngü sırasında küçük (%0,1) bir rol oynamıştır. 1939 M7.9, 1957 M7.0, 1967 M7.2 ve 1999 M7.5 kırıklarında, önemli bir rol oynamıştır (sırasıyla %16.9, %22.2, %17.9 ve %22.4). 1942 M7.1, 1944 M7.4, 1999 M7.1 kırıklarında, sismik döngünün neredeyse yarısını kaplayarak önemli bir rol oynamıştır (sırasıyla %54.4, %44.0 ve %48.3). Segmentler, benzer deformasyon oranlarına (19,5±0,5 – 24,2±0,3 mm/y arasında) maruz kalsalar da, farklı kayma/kilitlenme oranlarına sahip olduklarından farklı deprem potansiyellerine sahiptir. Sonuçlarımız, kayma oranlarının doğudan batıya doğru sistematik olarak hızlandığını göstermektedir. KAFZ' nin kırılması muhtemelen batı segmentlerinde 239±3 yılda sona erecektir. Son üç tamamlanmış ve mevcut tamamlanmamış döngülerdeki depremlerin uzay-zaman modeli, KAFZ'nin kırılmasının doğudan başladığını ve depremlerin yavaşlayarak, sistematik olarak batıya göç ettiğini doğrulamaktadır.

TABLE OF CONTENTS

ACKNOWLEDGEMENTS iii
ABSTRACT iv
ÖZET v
LIST OF FIGURES viii
LIST OF TABLES xiv
LIST OF SYMBOLS xv
LIST OF ACRONYMS/ABBREVIATIONS xvi
1. INTRODUCTION 1
2. EARTHQUAKE HISTORY OF NAFZ 5
2.1. Present incomplete earthquake cycle (1939 - today) 5
2.2. Last complete earthquake cycle (1666 - 1912) 9
2.3. Previous complete earthquake cycle (1419 - 1659) 12
2.4. Penultimate complete earthquake cycle (1236 - 1354) 15
2.5. Overall Behavior of the Seismicity along the NAFZ 16
3. GPS SLIP RATES 19
3.1. Unified Velocity Field 19
3.2. Arctangent Modelling 20
4. EARTHQUAKE CYCLE 36
4.1. Comparison of Inter-seismic Slip Accumulation with Co-seismic Slip Release 36
4.2. Spatio-temporal Partitioning Between Creeping and Locked Stages of the NAFZ 37
4.3. Current Magnitude Potentials along the NAFZ 40
5. DISCUSSIONS 43
6. CONCLUSION 49
REFERENCES 51
APPENDIX A: HISTORICAL EARTHQUAKE CATALOGUE AND PALEO-SEISMIC OBSERVATIONS 65

APPENDIX B: GPS VELOCITIES 72
APPENDIX C: SLIP RATE AND LOCKING DEPTH OBSERVATIONS
ALONG THE NAFZ FROM PREVIOUS STUDIES 92

LIST OF FIGURES

Figure 1.1. North Anatolian Fault Zone transform boundary between the tectonic plates, gray lines are the faults, dark gray line is the NAFZ and black line is our study area, red line is the 450 km rupture zone of the 1668 Great Anatolian earthquake [11]. 3

Figure 2.1. (Upper) Epicenters of migrating major earthquakes during the current earthquake cycle of NAFZ (earthquakes are represented by squares scaled to their magnitude, coast lines are light gray, faults are dark gray). (Lower) Along-fault location of epicenters versus event date. 7

Figure 2.2. Rupture zones along NAFZ (historical earthquakes are squares in gray, rupture area of earthquakes are red lines, coast lines are light gray, faults are dark gray). 8

Figure 2.3. Intensity records (pluses), misfits for the epicenter estimates (contours), and epicenter of the 1668 earthquake for M 8.1 obtained from the grid search. 9

Figure 2.4. (Upper) Epicenters of migrating major earthquakes during the last earthquake cycle of NAFZ (earthquakes are represented by squares scaled to their magnitude, M<7 earthquakes are dark red, earthquakes on inactive branches are blue, coast lines are light gray, faults are dark gray). (Lower) Along-fault location of epicenters versus event date. 10

Figure 2.5. Rupture zones along NAFZ (historical earthquakes are squares in gray, rupture area of earthquakes are red lines, rupture are on inactive branch of NAFZ are blue lines, coast lines are light gray, faults are dark gray). 11

Figure 2.6. Trench sites along NAFZ revealing evidence of 1668 earthquake rupture (historical earthquakes are squares in gray, paleo-seismic trench sites are red circles, trench on southern inactive branches is blue circle, error bars represent the determined temporal window (< 400 y) for paleo-events, coast lines are light gray, faults are dark gray). 12

Figure 2.7. (Upper) Epicenters of migrating major earthquakes during the previous earthquake cycle of NAFZ (earthquakes are represented by squares scaled to their magnitude, M<7 earthquakes are dark red, earthquakes on inactive branches are blue, coast lines are light gray, faults are dark gray). (Lower) Along-fault location of epicenters versus event date. 13

Figure 2.8. Trench sites along NAFZ revealing evidence of previous earthquake cycle ruptures (historical earthquakes are squares in gray, paleo-seismic trench sites are red circles, trenches on southern inactive branches are blue circles, error bars represent the determined temporal window (< 400 y) for paleo-events, coast lines are light gray, faults are dark gray). 14

Figure 2.9. (Upper) Epicenters of migrating major earthquakes during the penultimate earthquake cycle of NAFZ (earthquakes are represented by squares scaled to their magnitude, earthquakes on inactive branches are blue, coast lines are light gray, faults are dark gray). (Lower) Along-fault location of epicenters versus event date. 15

Figure 2.10. Trench sites along NAFZ revealing evidence of penultimate earthquake cycle ruptures (historical earthquakes are squares in gray, paleo-seismic trench sites are red circles, trench on southern inactive branches is blue circle, error bars represent the determined temporal window (< 400 y) for paleo-events, coast lines are light gray, faults are dark gray). 16

Figure 2.11. a) Seismicity migration along NAFZ from 1254 to present (darker red as cycle gets old). b) Cumulative seismicity along NAFZ within a 250-year period. c) Earthquake distribution along NAFZ over 10 years intervals. 17

Figure 2.12. Complete duration of the earthquake cycle along the NAFZ. a) Best fitting exponential function to the historical data. b) Bootstrap error analysis and red dot represents the best solution. 18

Figure 3.1. Velocity field of North Anatolia with respect to Eurasia. Red arrows are the reference velocity field [22], green arrows are [24], blue arrows are [21] and magenta arrows are [23]. 21

Figure 3.2. Right lateral motion and arctangent curve represent fault slip (v) and locking depth (D). 22

Figure 3.3. Density of GPS velocities along NAFZ (Blue to yellow: increasing density of GPS points per 80x80 km^2 grid). 22

Figure 3.4. Slip and depth in profile 1, upper panel: fault perpendicular profile, lower-left panel: red dots represent GPS points, lower-middle panel: best fitting arctangent curve, lower-right panel: black dots represent bootstrap error analysis for 100 resamples and red dot represents the best solution of slip rate and locking depth. 24

Figure 3.5. Slip and depth in profile 2, upper panel: fault perpendicular profile, lower-left panel: red dots represent GPS points, lower-middle panel: best fitting arctangent curve, lower-right panel: black dots represent bootstrap error analysis for 100 resamples and red dot represents the best solution of slip rate and locking depth. 25

Figure 3.6. Slip and depth in profile 3, upper panel: fault perpendicular profile, lower-left panel: red dots represent GPS points, lower-middle panel: best fitting arctangent curve, lower-right panel: black dots represent bootstrap error analysis for 100 resamples and red dot represents the best solution of slip rate and locking depth. 26

Figure 3.7. Slip and depth in profile 4, upper panel: fault perpendicular profile, lower-left panel: red dots represent GPS points, lower-middle panel: best fitting arctangent curve, lower-right panel: black dots represent bootstrap error analysis for 100 resamples and red dot represents the best solution of slip rate and locking depth. 27

Figure 3.8. Slip and depth in profile 5, upper panel: fault perpendicular profile, lower-left panel: red dots represent GPS points, lower-middle panel: best fitting arctangent curve, lower-right panel: black dots represent bootstrap error analysis for 100 resamples and red dot represents the best solution of slip rate and locking depth. 28

Figure 3.9. Slip and depth in profile 6, upper panel: fault perpendicular profile, lower-left panel: red dots represent GPS points, lower-middle panel: best fitting arctangent curve, lower-right panel: black dots represent bootstrap error analysis for 100 resamples and red dot represents the best solution of slip rate and locking depth. 29

Figure 3.10. Slip and depth in profile 7, upper panel: fault perpendicular profile, lower-left panel: red dots represent GPS points, lower-middle panel: best fitting arctangent curve, lower-right panel: black dots represent bootstrap error analysis for 100 resamples and red dot represents the best solution of slip rate and locking depth. 30

Figure 3.11. Slip and depth in profile 8, upper panel: fault perpendicular profile, lower-left panel: red dots represent GPS points, lower-middle panel: best fitting arctangent curve, lower-right panel: black dots represent bootstrap error analysis for 100 resamples and red dot represents the best solution of slip rate and locking depth. 31

Figure 3.12. Slip and depth in profile 9, upper panel: fault perpendicular profile, lower-left panel: red dots represent GPS points, lower-middle panel: best fitting arctangent curve, lower-right panel: black dots represent bootstrap error analysis for 100 resamples and red dot represents the best solution of slip rate and locking depth. 32

Figure 3.13. Slip and depth in profile 10, upper panel: fault perpendicular profile, lower-left panel: red dots represent GPS points, lower-middle panel: best fitting arctangent curve, lower-right panel: black dots represent bootstrap error analysis for 100 resamples and red dot represents the best solution of slip rate and locking depth. 33

Figure 3.14. Left: elastic deformation by the shear stress, right: stretching and sliding together, blue curve represents deformation, red line represents fault, arrows represent direction of the motion [104]. 34

Figure 4.1. Locked/creeping durations along the fault segments; red bars show the creeping stage and blue bars show the locked stage during the seismic cycle. 39

Figure 5.1. Slip rate variations along the NAFZ (red dots are slip rate estimations of this study, red line shows the increment trend from east to west, gray dost are slip rate estimations from others). 44

Figure 5.2. Locking depth variations along the NAFZ (red dots are locking depth estimations of this study, red line shows the decrease trend from east to west, gray dost are locking depth estimations from others). 46

LIST OF TABLES

Table 3.1. Slip and locking depth estimates of 10 profiles along the NAFZ. . . 35

Table 4.1. Observed co-seismic dextral slip, Estimated annual slip and Preliminary inter-seismic slip deficit along the NAFZ segments. 38

Table 4.2. Locked and creeping durations of the NAFZ segments. 39

Table 4.3. Future earthquake potentials along the NAFZ segments. 42

Table A.1. Historical earthquakes along the NAFZ. 65

Table A.2. Paleo-seismic records revealing the 1668 earthquake. 68

Table A.3. Paleo-seismic records revealing the penultimate earthquake cycle. . 70

Table B.1. GPS velocities. 72

Table C.1. Slip rate and locking depth estimations along the NAFZ. 92

LIST OF SYMBOLS

A	Rupture Area
d	Distance
D	Fault Locking Depth
I	Intensity
M	Magnitude
M_0	Seismic Moment
M_w	Moment Magnitude
n	Number of Samples
R	Rotation Vector
S	Fault Slip Rate
v	GPS-derived Velocity
v_e	Easting Velocity
v_n	Northing Velocity
v_{ref}	Velocity from Reference Frame
v_{rot}	Rotated Velocity
v_{tar}	Velocity from Target Frame
v_x	Fault Parallel Velocity
t	t-value
x	Local Cartesian coordinate (abscissa)
y	Local Cartesian coordinate (ordinate)
x'	Transformed Local Cartesian coordinate (abscissa)
y'	Transformed Local Cartesian coordinate (ordinate)
Θ	Azimuth
μ	Shear Modulus
σ	Standart Deviation

LIST OF ACRONYMS/ABBREVIATIONS

2D	Two Dimensional
3D	Three Dimensional
GNSS	Global Navigational Satellite Systems
GPS	Global Positioning Systems
Lat	Latitude
Lon	Longitude
MMI	Modified Mercally Intensity
NAFZ	North Anatolian Fault Zone

1. INTRODUCTION

Earthquake is the sudden release of seismic energy that is accumulated on the crust. Tectonic movement stores strain energy on crustal blocks surrounding the fault, which is locked due to the friction inside. There, rocks distort, bent, change shape elastically during the inter-seismic period. As the critical strain energy reaches and therefore high-friction patches on the fault plane fail plastically, locked fault suddenly releases the strain and generates earthquake slip, when the crustal blocks get back into their initial unstrained position. This cycle is named "elastic rebound theory"; where inter-seismic elastic energy stored since the latest failure of a fault patch/segment is assumed to be completely released as sudden co-seismic slip along the fault during the earthquake [1].

It is still in debate whether an earthquake would entirely release the strain energy stored on the fault plane since its latest failure. Especially for major earthquakes, long recurrence intervals prevent definitive test of elastic rebound. Additionally, the post-seismic period includes a creeping time the fault still discharges energy without locking and needs a time interval to enter the inter-seismic period again. Moreover, there are very few observations on when the fault plane finishes the healing process and starts storing the strain energy within the inter-seismic period [2]. In this frame, elastic rebound theory can be tested by comparing expected cumulative slip within the inter-seismic period and co-seismic slip generated by the earthquake. Quantifying the slip storage on a fault section since its last failure, and therefore forecasting slip of a future earthquake can only be reliable if inter-seismic slip rates, locked depth, and total duration of the locked period of the fault plane are verified.

Global Navigation Satellite Systems (GNSS) is a useful geodetic tool to measure inter-seismic slip rates (tectonic velocities) and locking depths on active faults in millimeter accuracy. We can monitor the very small amount of ground motion on the crust. Main idea behind is to measure the ground displacement of ground points

that their spatial location is known before. Advantages of using GNSS (or referred to as GPS here after) are, it requires a very low budget and provides very precise data covering very large areas. Also, it is possible to obtain the required data in a very short amount of time. For that, we benefit from GPS (Global Positioning Systems) to monitor tectonic plate movement in this study.

There are several misleading factors causing overestimation of future earthquake size, e.g., some fault patches might not be storing energy due to its creep movement, slip might be partitioned into the complex geometrical structures of the fault failing at different events. Investigating elastic rebound theory at a test ground allows verifying these unknowns, such as how long the fault creeps before it starts storing slip, or how slip is distributed between sub-segments of the fault.

North Anatolian Fault Zone (NAFZ hereafter) is a 1500 km long dextral strike-slip fault. It is the transform boundary between Anatolia and Eurasia plates, extending from east to west Anatolia, Northern Turkey (Figure 1.1). As one of the most seismically active faults on the earth, NAFZ operates through highly inhabited regions at an average slip rate of 25.0 mm/yr [3–5], and therefore generates high earthquake hazard risk. Conducting studies about its earthquake potential is a must for preventing inevitable consequences of any major (M7+) future earthquake. Elastic rebound investigation helps to determine its future earthquake potential. Although there are other earthquake clusters [6] or migrating earthquake sequences [7,8] in time and space, NAFZ is unique in terms of providing a perfect test laboratory to study elastic rebound. Because compared to its counterparts, there are many well-documented historical earthquake catalogs before and after the instrumental era, and many paleo-seismic records, revealing its repetitive earthquake clusters.

NAFZ has a characteristic behavior of producing several major earthquakes within approximately 243±3 years [9] starting from the east and migrating to the west with repetitive sequences [10]. The most recent sequence is started in the 20th century with the 1939 Erzincan earthquake and followed by 1942, 1943, 1944, 1957, 1967, 1999 and

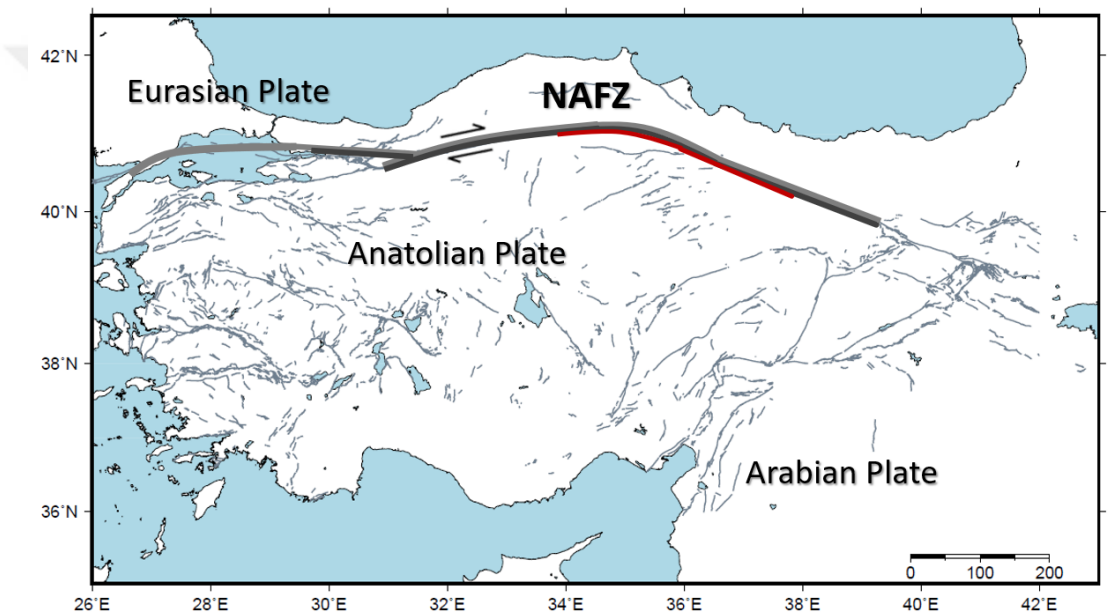

Figure 1.1. North Anatolian Fault Zone transform boundary between the tectonic plates, gray lines are the faults, dark gray line is the NAFZ and black line is our study area, red line is the 450 km rupture zone of the 1668 Great Anatolian earthquake [11].

1999 earthquakes, rupturing 1000 km long segment [11–14]. There are also remarkable records about the previous sequence. It started with the 1666 Erzincan earthquake, and was followed by the 1668 Great Anatolian earthquake, rupturing the same 1000 km long fault segment. Sequence terminated with 1719, 1754, 1766a, 1766b, and 1912 earthquakes in the west [11, 12, 15–19]. Since the same segment of the fault ruptured twice within 20th and 17th centuries, we are able to test elastic rebound theory along this 1000 km section of the NAFZ from Erzincan to Bolu, by using geodetic GPS velocities. Current cycle is statistically incomplete and one or more major earthquakes still could be pending [9]. By testing elastic rebound whether it is applicable or not, forecasting future earthquakes along central NAFZ is possible.

In the scope of this study, we compiled and revisited all available historical earthquake records (earthquake catalogs, Ottoman and/or foreign 17th century documentation, letters, diaries, official reports etc.) and paleo-seismic studies to better constrain 17th century earthquake locations. We determined possible rupture zone and epicenter of the 1668 earthquake with revised intensity distribution, using Modified Mercalli Intensity (MMI) scale modelling approach [20]. To achieve the best possible geodetic dataset, we compiled GPS derived inter-seismic velocities provided by previous studies [21–24] and transform them into a single reference frame following the analysis scheme by [25–27]. This allows removing the artificial effects of having different reference frames while creating a velocity field surrounding NAFZ. By using GPS derived velocities, we obtained annual slip rate and locking depth variations along the fault. To determine the slip variations along the fault in a small scale, we first defined an Euler pole and analyzed NAFZ by dividing it incrementally into 10 fault perpendicular profiles (80 km x 300 km) centering the pole. Using slip rates, we calculated accumulated seismic moment between current and the last earthquake cycles for every rupture area. Using slip rates, we re-produced moment magnitudes of each failed fault segment during the present cycle. We used their residuals to investigate the duration of non-coupled creeping periods. Future earthquake potential is also forecasted for each earthquake rupture zone.

2. EARTHQUAKE HISTORY OF NAFZ

Earth's crust stores the elastic energy that is released during the earthquake in the time between the two successive failures of a fault segment. Validating the elastic rebound theory, therefore requires ensuring exactly when the fault segments failed. In this context, we investigate historical earthquakes along the NAFZ combining instrumental, historical and paleo period earthquake records in order to verify time periods of previous earthquake cycles. We reviewed the literature and compiled all available studies reporting any earthquake during the last half millennium along the target area. Instrumental period records are used to identify the present incomplete earthquake cycle, which has been started in 1939. Historical records are used to identify previous complete earthquake cycles, especially the last one, which occurred within the time period of 1666 – 1912. Paleo-records are used to provide a second line of evidence for previous earthquake cycles (Appendix A). We obtained magnitudes of historical earthquakes applying Equation 2.1 where M is estimated magnitude, I is intensity, and D is the distance from fault [20].

$$M = (I + 3.99 + 0.0206 * D)/1.68 \tag{2.1}$$

2.1. Present incomplete earthquake cycle (1939 - today)

Present incomplete earthquake cycle initiated at 40.0 E° near Karlıova with the 1939 Erzincan (M7.9) earthquake. This event re-activated almost 360 km long section of the NAFZ from Erzincan to Amasya. The 1939 rupture is divided into five fault segments based on their slip distribution as follows: Erzincan, Refahiye, Suşehri, Reşadiye and Ezinepazarı from east to west. Dextral slips range between 2.3 and 10.5 m and slip is not uniform everywhere. The main rupture extends through the NAFZ from Erzincan to Niksar, while its 76 km long section splayed southward towards the Ezinepazarı fault [11, 13, 28]. The 1942 Niksar (M7.1) earthquake re-activated a 50

km long section of the NAFZ with average dextral slip 2.5 m. Right after, a 280 km section of the NAFZ failed during the 1943 Tosya (M7.7) earthquake. Its dextral slips ranged between 4 m and 4.5 m. Another 160 km section of the NAFZ ruptured through the west during the 1944 Gerede (M7.4) earthquake. The 1944 rupture comprised five fault segments based on slip distribution. From west to east, they are called the Bolu, Yeniçağa, Gerede, İsmetpaşa, and Bayramören segments. Dextral offsets ranged between 1 and 3.5 m. This earthquake is followed by the 1957 Abant (M7.0) earthquake reactivating a 30 km section of the NAFZ, where the dextral slip ranged between 1.4 m and 1.6 m. After this, the 1967 Mudurnu (M7.2) earthquake reactivated an 80 km section of the NAFZ, where the dextral slip ranged between 1.4 m and 1.9 m [11, 29–31]. Finally, the 1999 İzmit (M7.5), and the1999 Düzce (M7.1) earthquakes reached the western NAFZ, following its domino-like east-to-west failure of the to the eastern Marmara. These two devastating earthquakes reactivated 145 km and 40 km sections of the NAFZ, respectively. Surface rupture produced 5 segments that are Hersek, Gölcük, İzmit-Sapanca, Akyazı, Karadere during the 1999 İzmit earthquake. The 1999 Düzce earthquake ruptured three segments that are Eften, Dağdibi and Kaynaşlı. Dextral slip ranged between 2 m and 5 m in the case of the 1999 İzmit, and between 3 m and 5 m for the 1999 Düzce earthquakes [32–35]. We provide our catalog in Appendix A, Table A.1.

Figure 2.1 shows the space-time evolution of east-to-west migrating major earthquakes along the NAFZ. Earthquakes reactivated an 8°-degree section (32 – 40 E°) within 5 years (from 1939 to 1944). However, reactivation of a 3° section in the west (29 E° – 30 E°) took 55 years (from 1944 to 1999).

Rupture zones of these earthquakes indicate that the NAFZ has entirely failed from Erzincan to Izmit during the current cycle (1939 - 1999) (Figure 2.2). Earthquake distribution over time verifies that the Marmara region lacks of M7+ earthquakes. There remain un-ruptured fault segments as shown in Figure 2.2. Therefore, earthquake hazard in this region is currently considered much higher than the rest of the NAFZ.

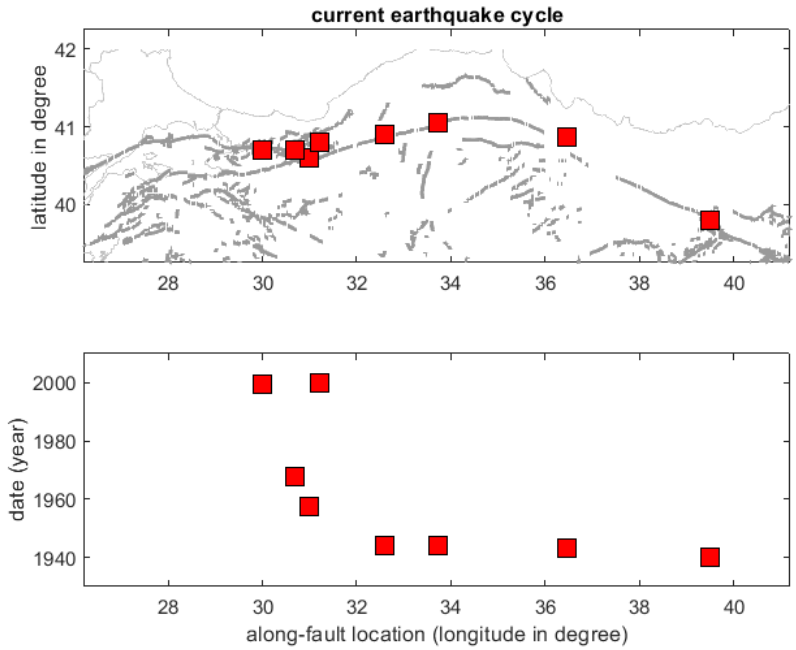

Figure 2.1. (Upper) Epicenters of migrating major earthquakes during the current earthquake cycle of NAFZ (earthquakes are represented by squares scaled to their magnitude, coast lines are light gray, faults are dark gray). (Lower) Along-fault location of epicenters versus event date.

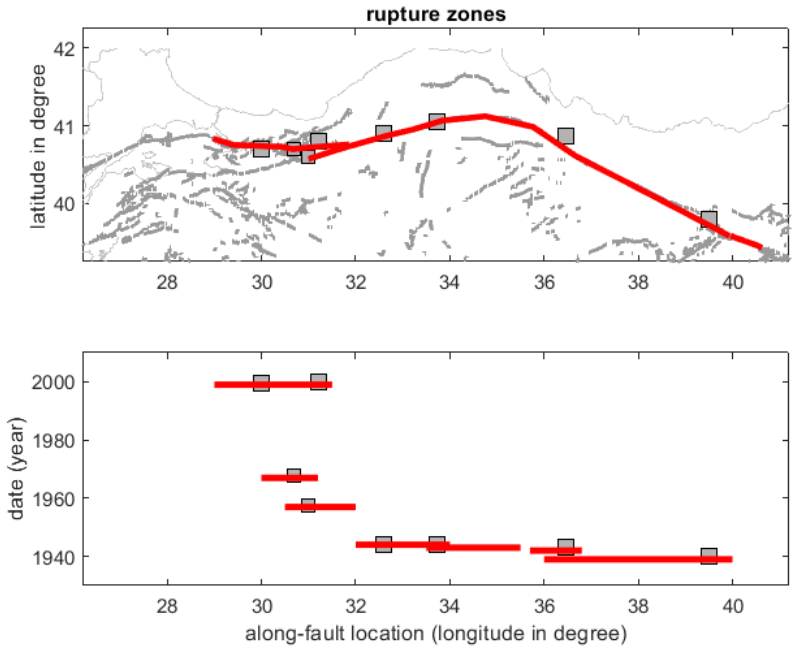

Figure 2.2. Rupture zones along NAFZ (historical earthquakes are squares in gray, rupture area of earthquakes are red lines, coast lines are light gray, faults are dark gray).

2.2. Last complete earthquake cycle (1666 - 1912)

Records show that the last complete earthquake cycle started with the 1666 Erzincan (M7.5) earthquake at the easternmost edge of NAFZ, reactivating a 131 km section of the fault from 39.8 to 41.4 E°. This earthquake is followed by the largest earthquake recorded in Anatolia ever, the 1668 Great Anatolian earthquake (M8.1). Its rupture zone starts from 40 E° and extends for a 450 km section towards the west [15, 16]. The damaged area of the 1668 earthquake covers the whole central NAFZ from Karabük in the west to Erzincan in the east. Following the method of [20], we located the epicentral region of the 1668 earthquake with its magnitude by analyzing its damage zone (Figure 2.3) [20]. Our approach is basically to search for the best fitting location and magnitude of the earthquake comparing the observed and calculated intensity values using Equation 2.1.

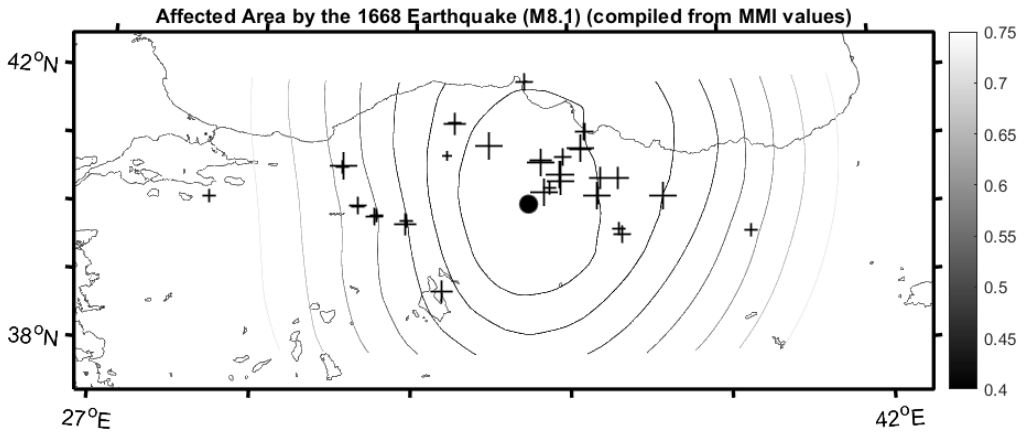

Figure 2.3. Intensity records (pluses), misfits for the epicenter estimates (contours), and epicenter of the 1668 earthquake for M 8.1 obtained from the grid search.

In the last complete cycle, the NAFZ accommodated six further major earthquakes: the 1719 İzmit earthquake (M7.4) rupturing 110 km, the 1766 İstanbul earthquake (M7.3) rupturing 65 km, the 1766 Tekirdağ (M7.4) rupturing 60 km, and the 1912 Ganos earthquake (M7.4) rupturing 55 km [12, 17]. Our compiled catalog shows the the distribution of epicenters along NAFZ in the 17h century earthquake cycle has

a similar spatio-temporal pattern with the current incomplete cycle. (Figure 2.4). We provide our catalog in Appendix A, Table A.1.

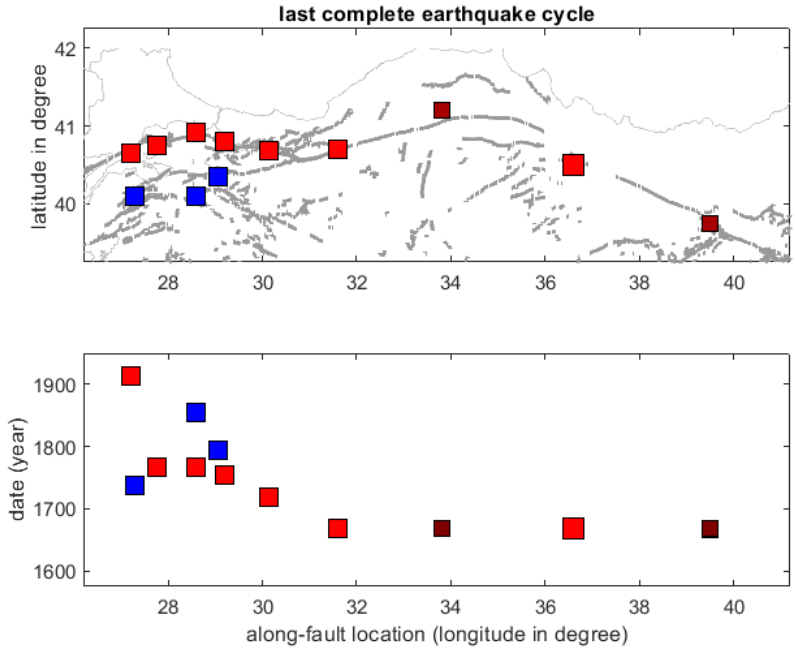

Figure 2.4. (Upper) Epicenters of migrating major earthquakes during the last earthquake cycle of NAFZ (earthquakes are represented by squares scaled to their magnitude, M<7 earthquakes are dark red, earthquakes on inactive branches are blue, coast lines are light gray, faults are dark gray). (Lower) Along-fault location of epicenters versus event date.

It was still in debate if the 1668 earthquake was a sequence of several earthquakes that occurred in a few months [36, 37]. Our combined catalog shows consistent spatio-temporal distribution of all the paleo-seismic trench studies (see Appendix A, Table A.2) that determined events highly correlated with the 1668 earthquake, with all available historical data. NAFZ hosts many multi-segment earthquakes, and our catalog shows 1668 probably was a single multi-segment earthquake (Figure 2.5) consistent with previous studies [19, 38].

Our compiled historical and paleo-seismological record show that, NAFZ sub-

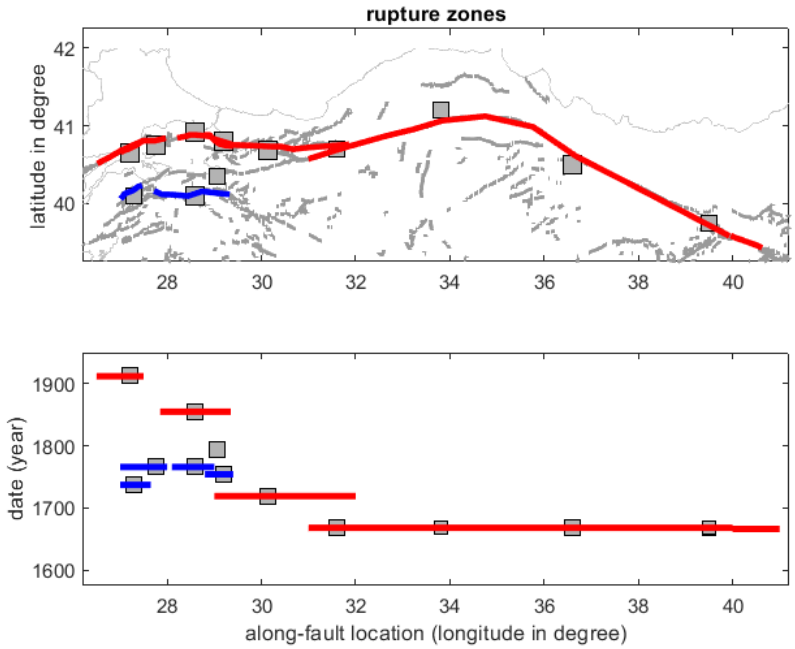

Figure 2.5. Rupture zones along NAFZ (historical earthquakes are squares in gray, rupture area of earthquakes are red lines, rupture are on inactive branch of NAFZ are blue lines, coast lines are light gray, faults are dark gray).

segments failed between 26.4 – 41 E° in last complete earthquake cycle, in consistency with the current incomplete one. Figure 2.6 shows the ruptures from the last complete cycle that are overlapped with current rupture zones, clearly demonstrating the unruptured segment of western NAFZ in Marmara.

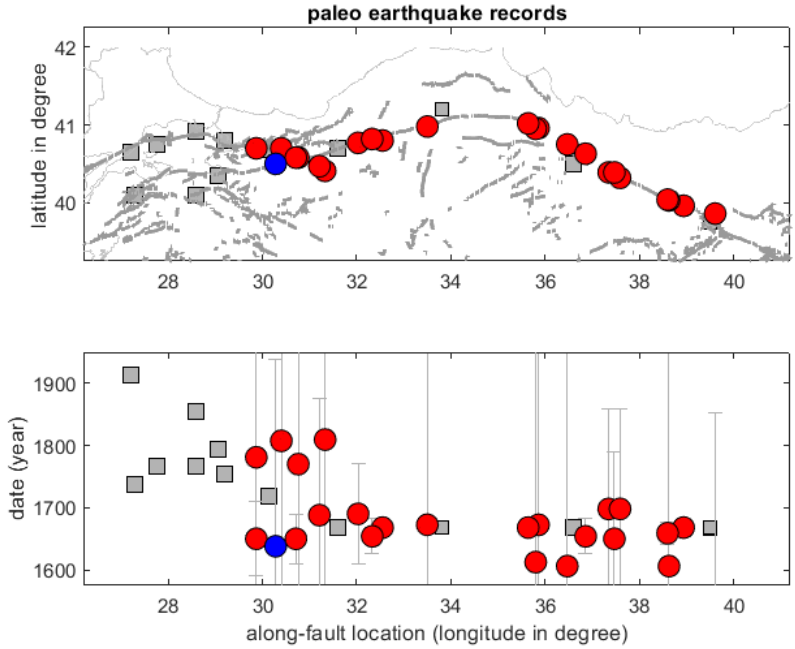

Figure 2.6. Trench sites along NAFZ revealing evidence of 1668 earthquake rupture (historical earthquakes are squares in gray, paleo-seismic trench sites are red circles, trench on southern inactive branches is blue circle, error bars represent the determined temporal window (< 400 y) for paleo-events, coast lines are light gray, faults are dark gray).

2.3. Previous complete earthquake cycle (1419 - 1659)

According to records we compiled, the previous earthquake cycle consists of 10 major earthquakes rupturing the entire NAFZ from east to west. Its failure started with the 1419 earthquake near central Anatolia (M7.5), rupturing 130 km-long segment and it is followed by major earthquakes 1481 (M7.7) with 205 km rupture zone, 1490 (M7.4) with 110 km rupture zone, 1509 (M7.5) with 95 km rupture zone, 1556 (M7.3)

with 65 km rupture zone, 1569 (M7.3) with 60 km rupture zone, 1625 (M7.1) with 53 km rupture zone, 1659 (M7.3) with 55 km rupture zone having the same seismic migration pattern as shown in Figure 2.7 [5,39]. We provide our catalog in Appendix A, Table A.1.

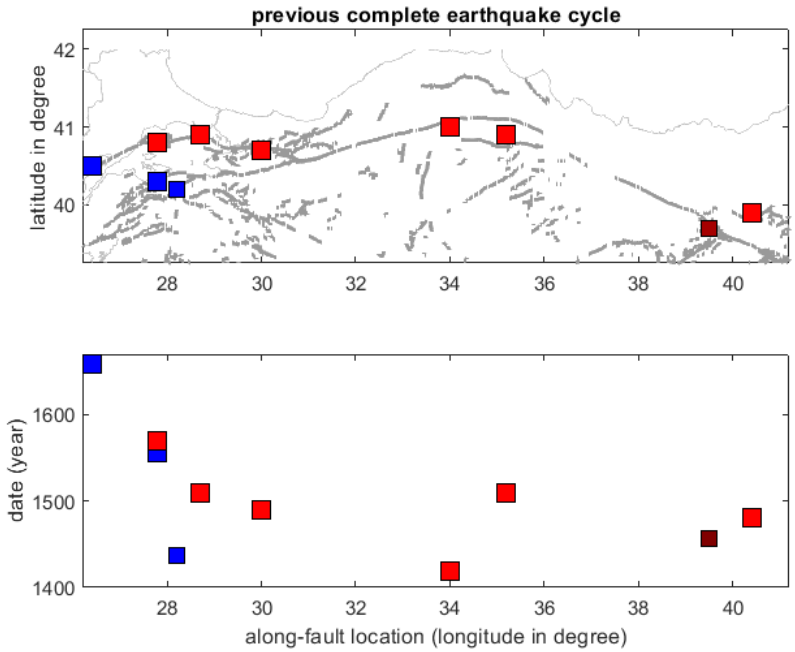

Figure 2.7. (Upper) Epicenters of migrating major earthquakes during the previous earthquake cycle of NAFZ (earthquakes are represented by squares scaled to their magnitude, M<7 earthquakes are dark red, earthquakes on inactive branches are blue, coast lines are light gray, faults are dark gray). (Lower) Along-fault location of epicenters versus event date.

Paleo-records (see Appendix A, Table A.3) support that the NAFZ ruptured the same segments systematically from east to west as the current and previous cycles, providing us a chance to validate elastic rebound for several centuries (Figure 2.8).

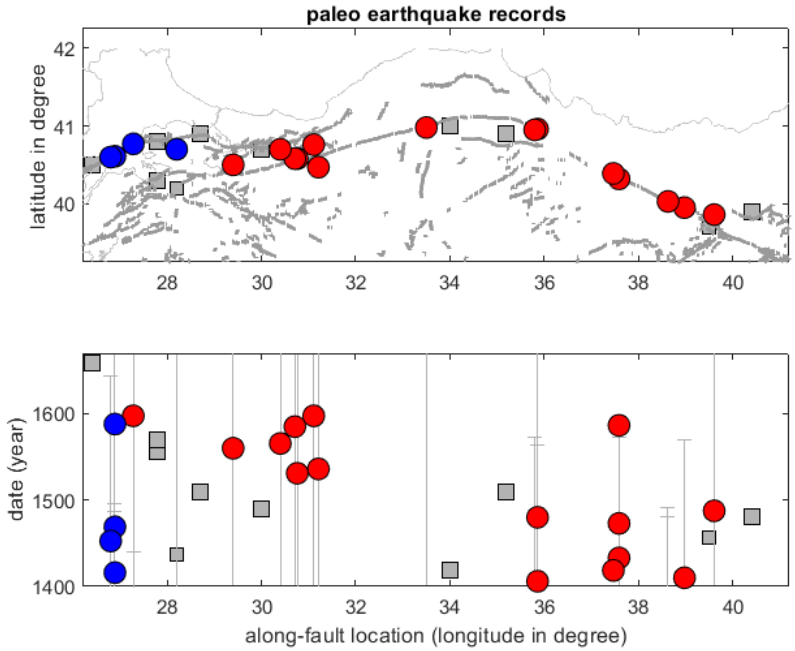

Figure 2.8. Trench sites along NAFZ revealing evidence of previous earthquake cycle ruptures (historical earthquakes are squares in gray, paleo-seismic trench sites are red circles, trenches on southern inactive branches are blue circles, error bars represent the determined temporal window (< 400 y) for paleo-events, coast lines are light gray, faults are dark gray).

2.4. Penultimate complete earthquake cycle (1236 - 1354)

Although historical records are limited as the cycle gets older, our catalog reveals that the NAFZ indicates a similar failure pattern in this earthquake cycle as well. Historical earthquakes provide evidence that the NAFZ failed more than 1000 km in this cycle, starting in the east and continuing in the west. We provide our catalog in Appendix A, Table A.1.

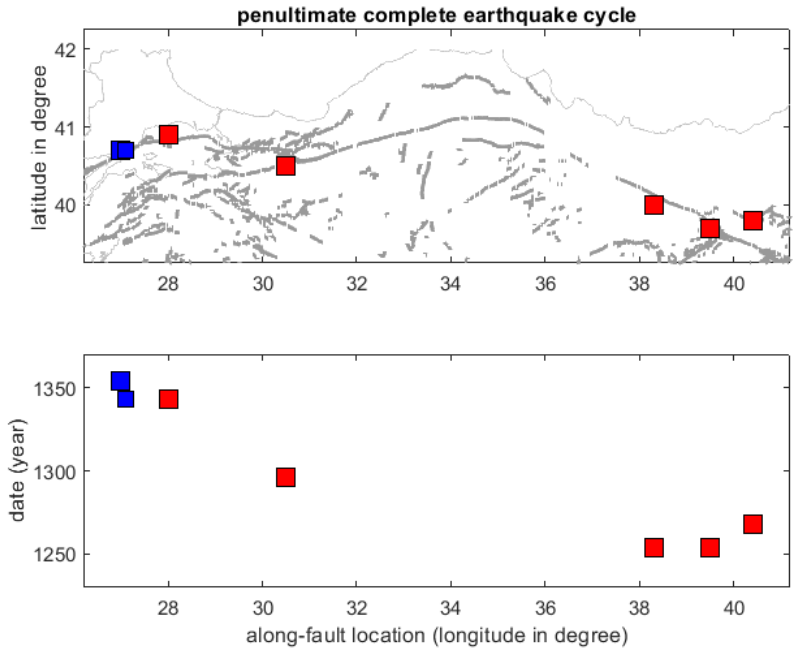

Figure 2.9. (Upper) Epicenters of migrating major earthquakes during the penultimate earthquake cycle of NAFZ (earthquakes are represented by squares scaled to their magnitude, earthquakes on inactive branches are blue, coast lines are light gray, faults are dark gray). (Lower) Along-fault location of epicenters versus event date.

Earthquake catalogs [36, 37] covering central and eastern Anatolia could be incomplete due to social-cultural situation of the region at that era (Figure 2.9 and Figure 2.10). Despite this data gap, the overall pattern is still similar to the following three cycles as paleo-seismic studies provides a second line of evidence (see Appendix A, Table A.3).

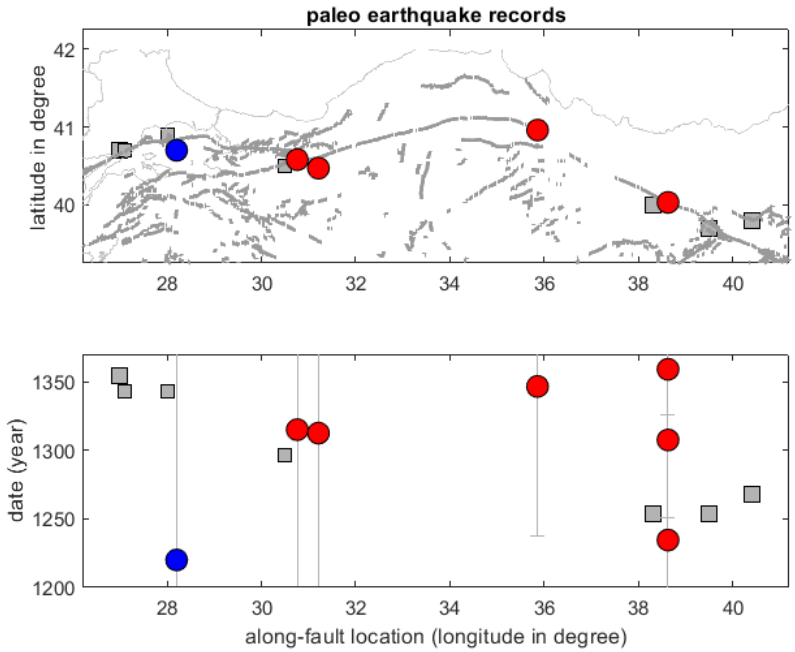

Figure 2.10. Trench sites along NAFZ revealing evidence of penultimate earthquake cycle ruptures (historical earthquakes are squares in gray, paleo-seismic trench sites are red circles, trench on southern inactive branches is blue circle, error bars represent the determined temporal window ($<$ 400 y) for paleo-events, coast lines are light gray, faults are dark gray).

2.5. Overall Behavior of the Seismicity along the NAFZ

Our compiled catalog provides the information that seismicity along NAFZ follows a similar pattern in terms of spatio-temporal distribution of major earthquakes cycling every 239±3 years. The current and previous three earthquake cycles of NAFZ show that the major earthquakes migrate along the fault from east to west, rupturing the same segments with 239 years' intervals. In the first stage of the failure, the section between 30E° - 41E° fails only in a few years. In the second stage, migration velocity decreases dramatically, and the failure of the rest of the fault to the west takes at least two decades. Figure 2.11a shows, current earthquake cycle is still in progress based on the space-time pattern of the seismicity cycling from 1254 to now. Figure 2.11a also shows that the western NAFZ generates more earthquakes rupturing shorter fault

segments compared to the central and the eastern NAFZ.

Figure 2.11b shows that normalized earthquake distribution along longitudes show exponential increase to the west. We analyzed the distribution of major earthquakes along NAFZ for every longitude over a cycle (Figure 2.11c). For ten years intervals, we calculated most probable longitudes to produce major earthquakes. Figure 2.11c shows major earthquakes most likely to occur between 25 – 27 E° longitudes.

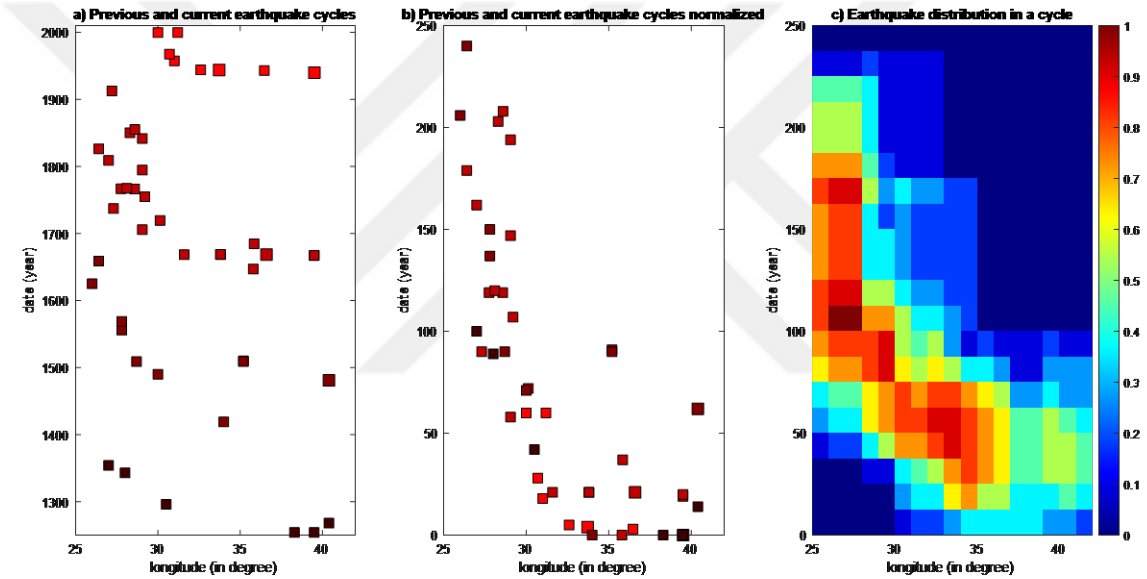

Figure 2.11. a) Seismicity migration along NAFZ from 1254 to present (darker red as cycle gets old). b) Cumulative seismicity along NAFZ within a 250-year period. c) Earthquake distribution along NAFZ over 10 years intervals.

Figure 2.12a shows the best fitting exponential function to the historical data. As we determined using bootstrap error analysis (Figure 2.12b), cycle has the highest probability to be terminated in following 157±3 years. It is clear that earthquakes decelerate throughout to western segments.

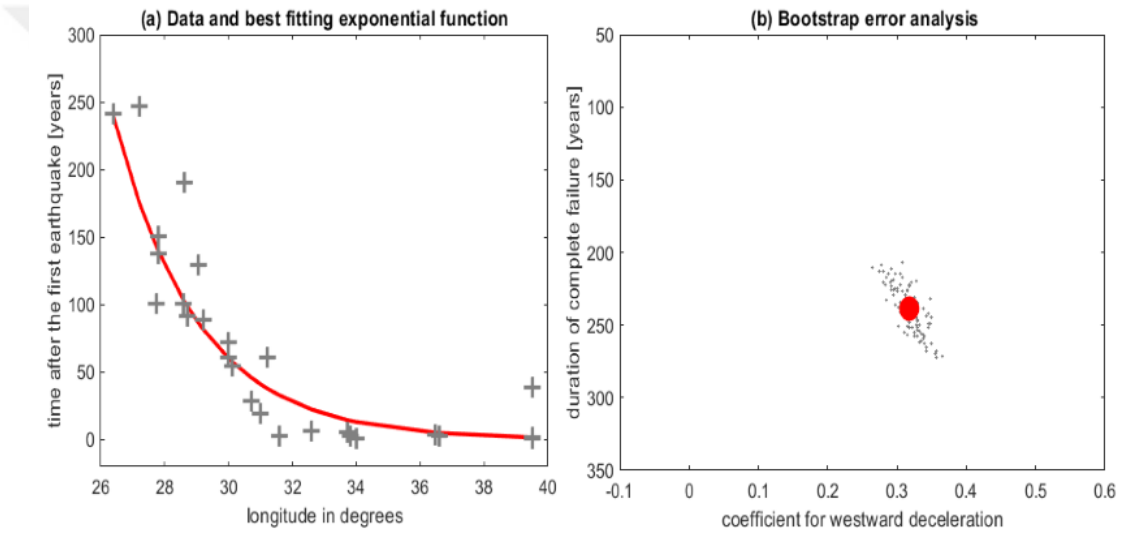

Figure 2.12. Complete duration of the earthquake cycle along the NAFZ. a) Best fitting exponential function to the historical data. b) Bootstrap error analysis and red dot represents the best solution.

3. GPS SLIP RATES

We investigated more than 1000 km section of the NAFZ, which is segmented and therefore fragmentally ruptured with several earthquakes. In this context, we are able to test elastic rebound by comparing potential inter-seismic slip accumulation and co-seismic slips to investigate partitioning between creep and locking in time and space. For this, we used 521 GPS velocities to find inter-seismic slip rates between two successive earthquake cycles and compared them with the co-seismic slips to quantify released and stored seismic slip. We focused on 28 – 40 E°, aiming to intensify GPS coverage especially for central North Anatolia unifying all available GPS measurements following [25]. We subdivided this 12° long fault section into 10 fault perpendicular profiles and estimated slip and locking depth variations along fault following [40].

3.1. Unified Velocity Field

To achieve an intense horizontal velocity field along the target area, we compiled 521 GPS measurements (Appendix B) from previous studies [21–24]. We homogenously integrated compiled GPS measurements following the analysis scheme by [25–27] to avoid artificial effects of different reference frames (Figure 3.1). We aim to demonstrate the westward escape of the Anatolian plate with respect to the Eurasia. Therefore, to transform our GPS velocity field into Eurasia fixed reference frame, we select our reference frame as [22]. Firstly, we determined the common GPS points between our reference frame and the other data sets. In a second step, we defined a rotation vector R by simultaneously calculating the mean difference of north v_n and east v_e components of common velocity vectors using Equation 3.1, where v_{ref} is common GPS vectors from the reference frame and v_{tar} is common vectors obtained from other studies. The rotation vector is then added to the data coming from other data sets v and all vectors became rotated (v_{rot}) (Equation 3.2). In Figure 3.1, the upper panel shows the velocity vectors before unification and the lower panel shows the unified velocity field. Maximum and minimum error limits of our GPS velocities are provided in Appendix B

(between -0.182 and 0.049).

$$R = \begin{bmatrix} v_n \\ v_e \end{bmatrix} = \text{mean}\,(v_{ref} - v_{tar}) \tag{3.1}$$

$$v_{\text{rot}} = v + R \tag{3.2}$$

Homogenously integrated velocity field shows Eurasia fixed movement of the Anatolian plate counterclockwise towards the South-west, as a result of collisional tectonics in eastern Anatolia and extensional regime along the Aegean Sea in the west (Figure 3.1). The Anatolian plate moves to the west 20 mm/y in the east and 24 mm/y in the west [3, 4].

3.2. Arctangent Modelling

We used GPS measurements to simulate a two-dimensional (2D) arctangent model across the fault in order to investigate slip rates and locking depths along the studied section of the NAFZ [40, 41]. The arctangent model has an approximation that the fault is infinitely long through strike direction and has a purely vertical dip to the elastic half space. This model assumes that the slip and locking depth are constant along the fault and ignores the strain asymmetry between the sides of the fault. As a result, an arctangent curve represents this motion at both sides of the fault as a function of fault slip rate and locking depth as shown in Figure 3.2. The figure explains that the ground motion is slower very near to the fault, as a result of rocks locking at a distance from the surface. Surface deformation decreases with an increasing distance away from the fault along the fault-perpendicular profile.

This method allows us to make an overall quantification of horizontal slip and locking depth for strike-slip faults in a simple but reliable manner compared to three-

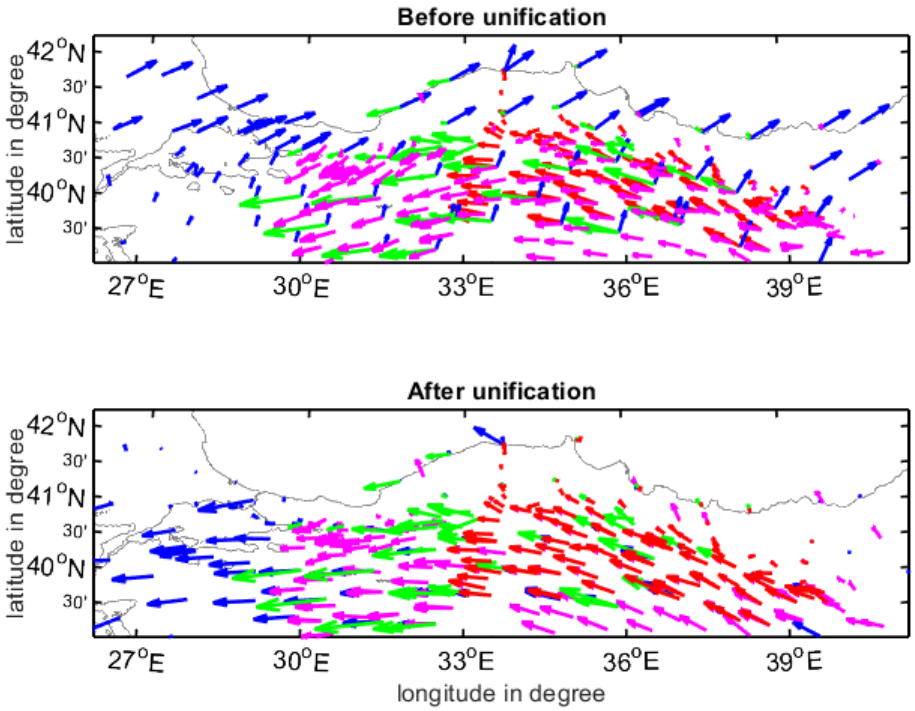

Figure 3.1. Velocity field of North Anatolia with respect to Eurasia. Red arrows are the reference velocity field [22], green arrows are [24], blue arrows are [21] and magenta arrows are [23].

dimensional (3D) slip models. They consist much more unknowns such as geometry and slip direction of the fault. However, NAFZ has varieties of geometry and earthquake producing budgets at different segments. Fault slip and locking depth differ at every longitude. Besides, implementing 3D models requires denser and homogeneous GPS coverage, yet our compiled GPS velocity field is not perfectly distributed over our target section of the NAFZ as shown in Figure 3.3. We investigated the 28 – 40 E° and as shown in figure, 30 – 31 E° encloses 30 GPS points, in contrast, GPS points are poor in terms of density at central NAFZ (34 – 35 E°) compared to eastern and western segments of the fault. For that, it is more convenient to apply the 2D arctangent model.

To stimulate variations of slip and locking depth along NAFZ, we applied a 2D

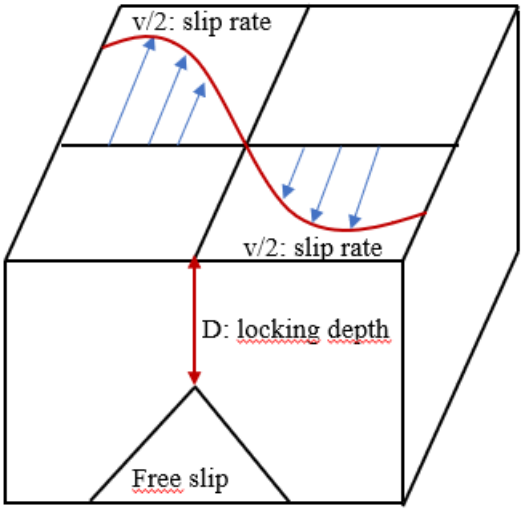

Figure 3.2. Right lateral motion and arctangent curve represent fault slip (v) and locking depth (D).

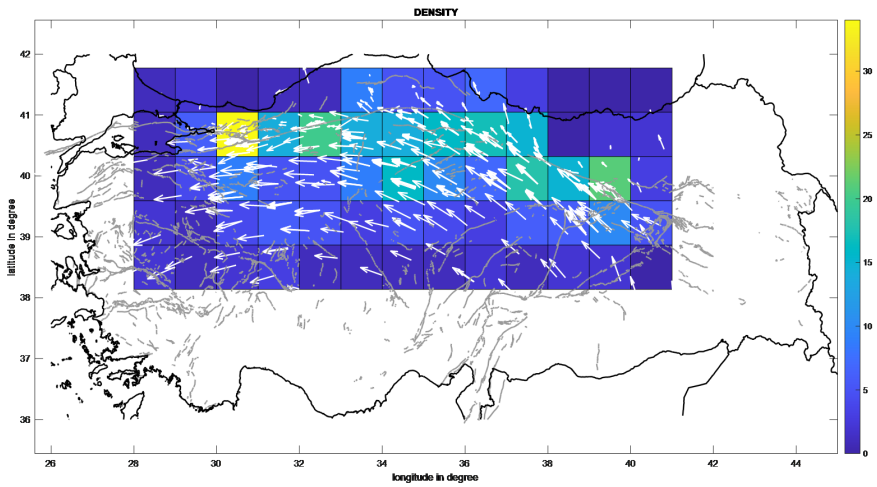

Figure 3.3. Density of GPS velocities along NAFZ (Blue to yellow: increasing density of GPS points per 80x80 km^2 grid).

arctangent model covering nearly the entire fault framing 10 equal fault-perpendicular profiles. It allows us to make an incremental investigation of the slip and the locking

depth along the fault. We estimated slip and locking depth parameters for every profile by using Equation 3.3 where v_x is GPS-derived fault-parallel ground velocity, S is the slip of the fault, which is far field velocity, X is the distance of the GPS point from the fault and D is locking depth. To minimize the misfit between model and data, we simultaneously searched for all potential locking depths and slip rates in the ranges of 0-40 km and 0-40 mm/y, respectively. We followed a bootstrap error analysis scheme to calculate the uncertainty of slip rate and locking depth [42]. We repeated solutions of Equation 3.3 for 100 resamples, then calculated the uncertainty for 95 percent confidence level by multiplying standard error (standard deviation (σ) divided by the square root of the number of samples (n) with corresponding t-value (t) (1.984 for our case of 100 samples). To summarize, uncertainty for 95 percent confidence level is calculated by dividing the standard deviation by 5.04 in the case of 100 bootstrap solutions as shown in Equation 3.4.

$$v_x = \frac{S}{\pi} \tan^{-1} \frac{X}{D} \tag{3.3}$$

$$\text{Confidence Level } (95\%) = \frac{\sigma}{\sqrt{n}} * t \tag{3.4}$$

We analyzed every profile using corresponding GPS measurements. Side-by-side profiles slightly overlaps each other to provide smooth transition along the fault. The profiles are defined perfectly perpendicular to the fault, and therefore fault parallel GPS velocities are used as fault-parallel ground velocity. To achieve this, we defined corner points of our profiles for an arbitrary pole at 33 E° and 28 S°, by giving the near edge and far edge distances of the profile from the pole. We transform points' coordinates into local cartesian coordinates x and y . Finally, we rotate the coordinate system by the azimuth (θ) of the profile and we find east-west (x') and north-south (y') velocities of the GPS sites as explained in Equation 3.5 for positive θ and 3.6 for

negative θ values.

$$\begin{bmatrix} x' \\ y' \end{bmatrix} = \begin{bmatrix} \cos\emptyset & -\sin\emptyset \\ \sin\emptyset & \cos\emptyset \end{bmatrix} \times \begin{bmatrix} x \\ y \end{bmatrix} \tag{3.5}$$

$$\begin{bmatrix} x' \\ y' \end{bmatrix} = \begin{bmatrix} \cos\emptyset & \sin\emptyset \\ -\sin\emptyset & \cos\emptyset \end{bmatrix} \times \begin{bmatrix} x \\ y \end{bmatrix} \tag{3.6}$$

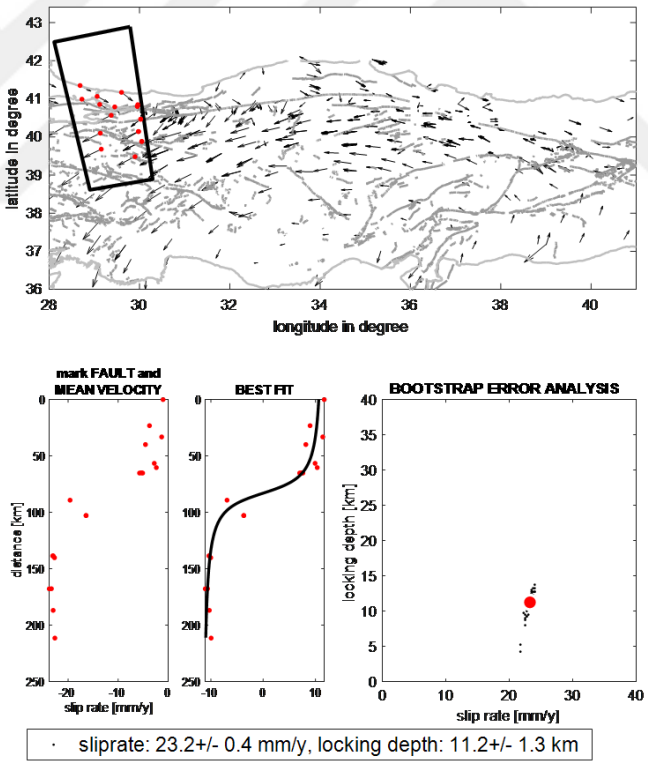

Figure 3.4. Slip and depth in profile 1, upper panel: fault perpendicular profile, lower-left panel: red dots represent GPS points, lower-middle panel: best fitting arctangent curve, lower-right panel: black dots represent bootstrap error analysis for 100 resamples and red dot represents the best solution of slip rate and locking depth.

We define a fault perpendicular profile between 28.11 and 29.79 E° as shown in the upper panel and used 16 GPS points as shown in the lower-left panel in Figure 3.4. The best fitting arctangent curve in the lower-middle panel represents elastic deformation and strain accumulation in this region. The figure in the lower-right panel shows slip and locking depth calculation with bootstrap error analysis. We calculated slip rate 23.2±4.4 mm/y to the east and locking depth 11.2±1.3 km.

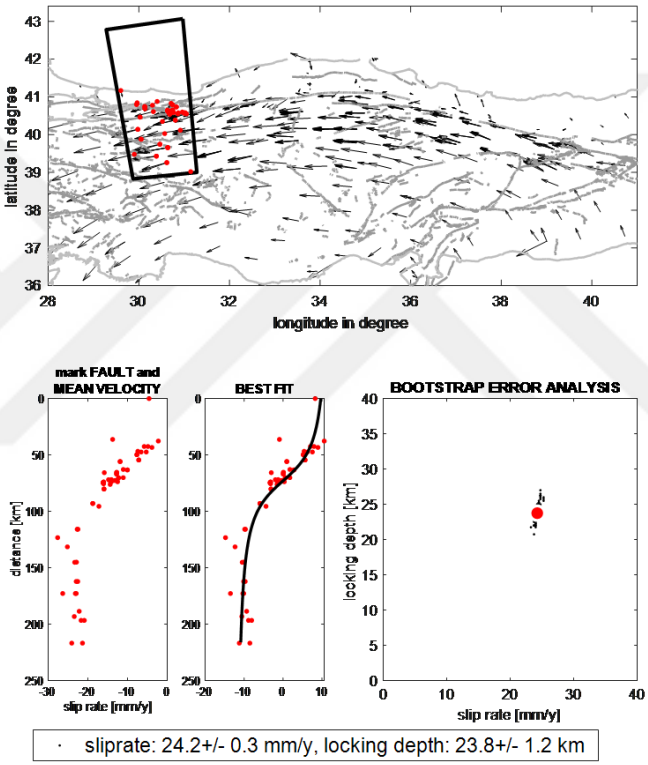

Figure 3.5. Slip and depth in profile 2, upper panel: fault perpendicular profile, lower-left panel: red dots represent GPS points, lower-middle panel: best fitting arctangent curve, lower-right panel: black dots represent bootstrap error analysis for 100 resamples and red dot represents the best solution of slip rate and locking depth.

We define a fault perpendicular profile between 29.28 and 30.97 E° as shown in the upper panel and used 50 GPS points as shown in the lower-left panel in Figure 3.5. We calculated slip rate 24.2±0.3 mm/y to the east and locking depth 23.8±1.2 km. Among

all the profiles, NAFZ has the biggest slip rate and locking depth in this profile. The arctangent curve in the lower-middle panel represents the highest elastic deformation and therefore, the highest strain accumulation among all the profiles. The lower-right panel shows slip and locking depth estimates with bootstrap error analysis. Compared to profile 1, profile 2 has smaller error bounds for slip and locking depth. In the last incomplete earthquake cycle, this section was ruptured during the 1999 İzmit (M7.4) earthquake.

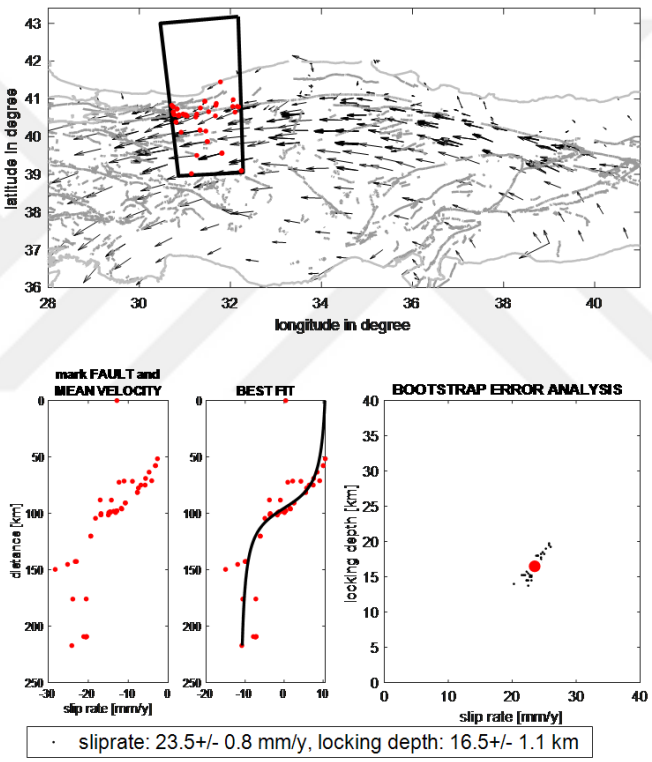

Figure 3.6. Slip and depth in profile 3, upper panel: fault perpendicular profile, lower-left panel: red dots represent GPS points, lower-middle panel: best fitting arctangent curve, lower-right panel: black dots represent bootstrap error analysis for 100 resamples and red dot represents the best solution of slip rate and locking depth.

We define a fault perpendicular profile between 30.46 and 32.17 E° as shown in the upper panel and used 40 GPS points as shown in the lower-left panel in Figure 3.6. The

lower-middle panel shows that similar to profile 2, profile 3 has an elastic deformation with a higher slip rate compared to other profiles. Bootstrap error analysis shows a scattered error boundary compared to other profiles. The reason behind this is the outlier GPS points, however, our bootstrap analysis resulted in a 23.5±0.8 mm/y slip rate and 16.5±1.1 km locking depth consistent with the neighboring profiles. major earthquakes that occurred in this region during the current incomplete earthquake cycle are the 1957 Abant (M7.0), 1967 Mudurnu (M7.2) earthquake, and 1999 Düzce (M7.1) earthquake.

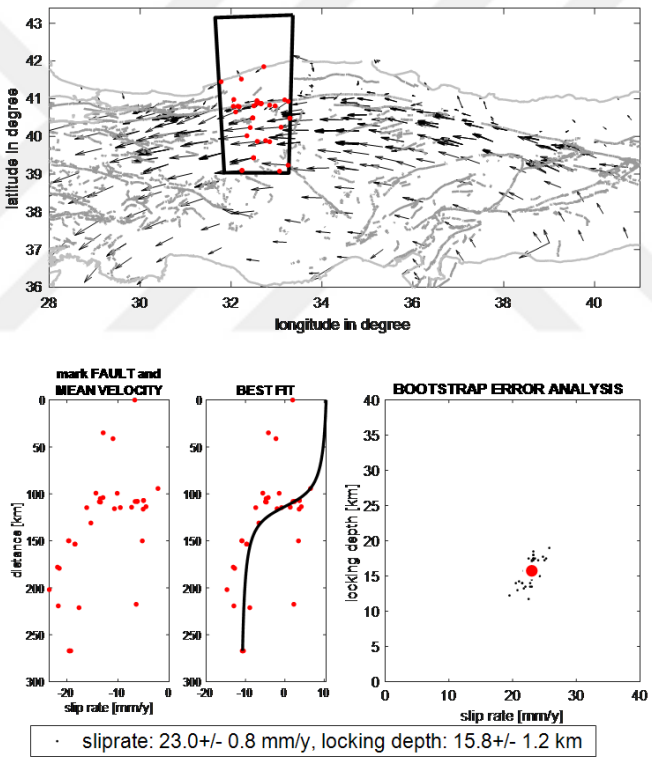

Figure 3.7. Slip and depth in profile 4, upper panel: fault perpendicular profile, lower-left panel: red dots represent GPS points, lower-middle panel: best fitting arctangent curve, lower-right panel: black dots represent bootstrap error analysis for 100 resamples and red dot represents the best solution of slip rate and locking depth.

We define a fault perpendicular profile between 31.65 and 33.36 E° as shown in

the upper panel and used 34 GPS points as shown in the lower-left panel in Figure 3.7. The lower-middle panel shows profile 4 also has an elastic deformation with a higher slip rate compared to other profiles. Bootstrap error analysis shows a scattered error boundary for both slip rate and locking depth compared to other profiles. The reason behind is that this region has the most sparse distribution of GPS stations among all the profiles. However out bootstrap analysis resulted in a 23.0±0.8 mm/y slip rate and 15.8±1.2 km locking depth consistent with the neighboring profiles. The latest major earthquake that occurred in this region is the 1944 Bolu-Gerede (M7.4) earthquake.

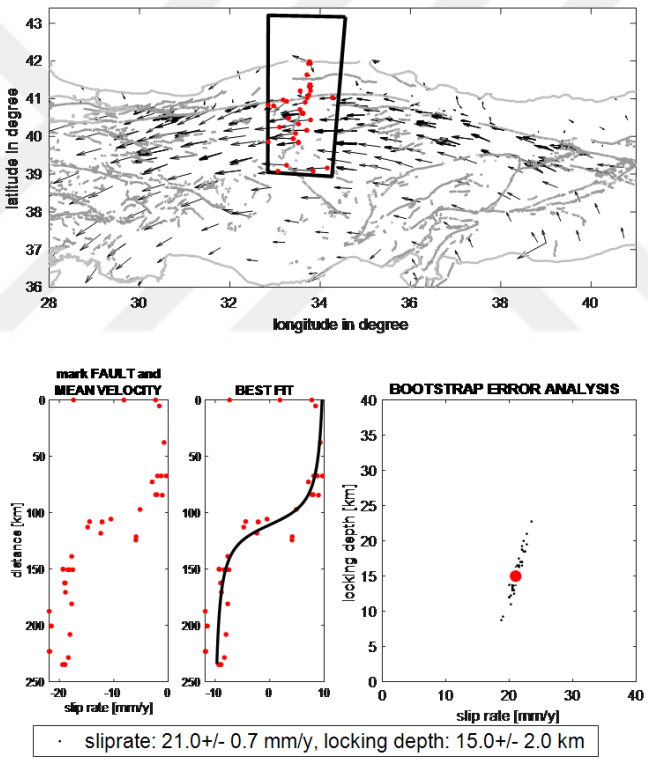

Figure 3.8. Slip and depth in profile 5, upper panel: fault perpendicular profile, lower-left panel: red dots represent GPS points, lower-middle panel: best fitting arctangent curve, lower-right panel: black dots represent bootstrap error analysis for 100 resamples and red dot represents the best solution of slip rate and locking depth.

We define a fault perpendicular profile between 32.85 and 34.56 E° as shown in

the upper panel and used 40 GPS points as shown in the lower-left panel in Figure 3.8. Arctangent curve in the lower-middle panel shows plastic deformation compared to other profiles. Slip rate decreases drastically in this region. In profile 5, transition from elastic deformation to plastic deformation becomes significant. Bootstrap error analysis shows a scattered error boundary compared to other profiles. However, our bootstrap analysis resulted in a 21.0±0.7 mm/y slip rate and 15.0±2.0 km locking depth consistent with the neighboring profiles. The latest major earthquakes that occurred in this region during the current incomplete earthquake cycle is 1943 Tosya-Ladik (M7.7) earthquake.

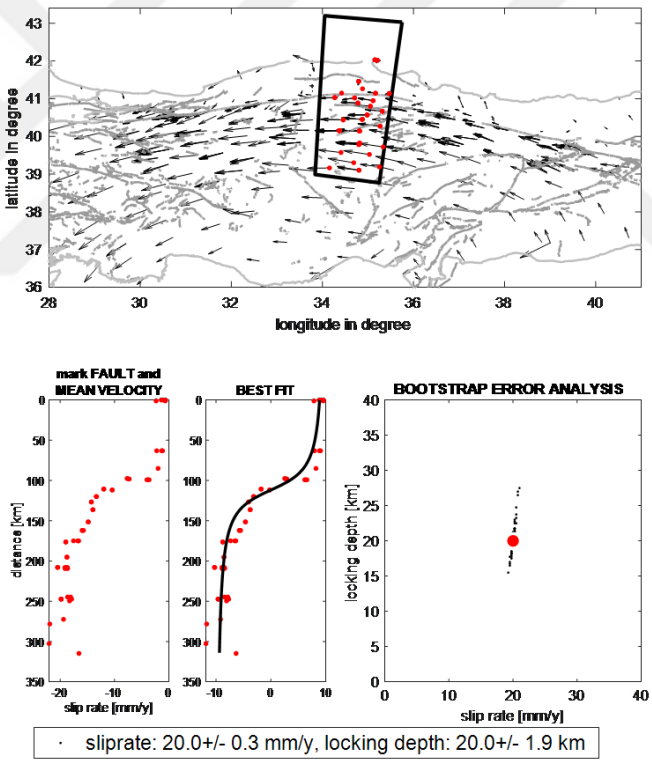

Figure 3.9. Slip and depth in profile 6, upper panel: fault perpendicular profile, lower-left panel: red dots represent GPS points, lower-middle panel: best fitting arctangent curve, lower-right panel: black dots represent bootstrap error analysis for 100 resamples and red dot represents the best solution of slip rate and locking depth.

We define a fault perpendicular profile between 34.05 and 35.75 E° as shown in the upper panel and used 49 GPS points as shown in the lower-left panel in Figure 3.9. The lower-middle panel shows profile 6 also has a transition from elastic deformation to plastic deformation. Slip rate and decreases and locking depth increases in this region compared to other profiles. Bootstrap error analysis shows a scattered error boundary for locking depth in particular. Our bootstrap analysis resulted in a 20.0±0.3 mm/y slip rate and 20.0±1.9 km locking depth.

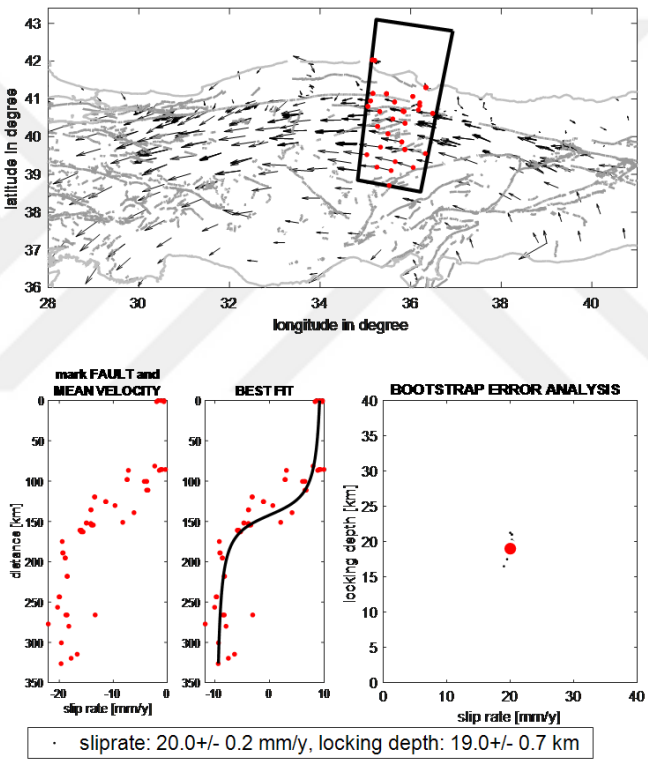

Figure 3.10. Slip and depth in profile 7, upper panel: fault perpendicular profile, lower-left panel: red dots represent GPS points, lower-middle panel: best fitting arctangent curve, lower-right panel: black dots represent bootstrap error analysis for 100 resamples and red dot represents the best solution of slip rate and locking depth.

We define a fault perpendicular profile between 35.24 and 36.93 E° as shown in the upper panel and used 53 GPS points as shown in the lower-left panel in Figure 3.10.

The lower-middle panel shows the best fitting arctangent curve that represents plastic deformation with a lower slip rate compared to other profiles. Bootstrap error analysis shows a narrow error boundary compared to other profiles. Our bootstrap analysis resulted in a 20.0±0.2 mm/y slip rate and 19.0±0.7 km locking depth consistent with the neighboring profiles. This section of NAFZ was lastly ruptured during the 1942 Tokat-Erbaa (M7.1) earthquake.

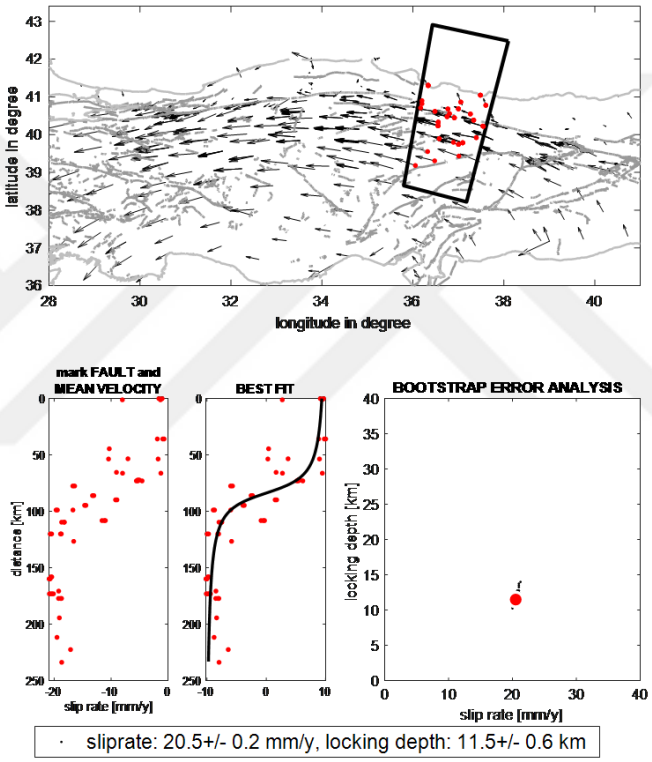

Figure 3.11. Slip and depth in profile 8, upper panel: fault perpendicular profile, lower-left panel: red dots represent GPS points, lower-middle panel: best fitting arctangent curve, lower-right panel: black dots represent bootstrap error analysis for 100 resamples and red dot represents the best solution of slip rate and locking depth.

We define a fault perpendicular profile between 36.43 and 38.10 E° as shown in the upper panel and used 56 GPS points as shown in the lower-left panel in Figure 3.11. The lower-middle panel shows the best fitting arctangent curve represents a deformation

zone more likely to be plastic. The region has a lower elastic deformation rate compared to other profiles. Bootstrap error analysis shows the narrowest error boundary among other profiles. We calculated the most precise slip rate and locking depth in this region, compared to other profiles; 20.5±0.2 mm/y and 11.5±0.6 km respectively.

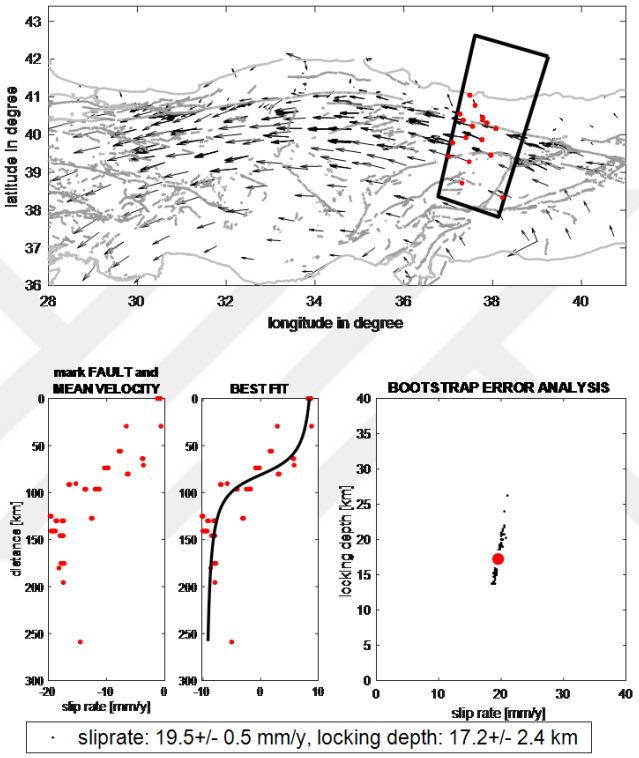

Figure 3.12. Slip and depth in profile 9, upper panel: fault perpendicular profile, lower-left panel: red dots represent GPS points, lower-middle panel: best fitting arctangent curve, lower-right panel: black dots represent bootstrap error analysis for 100 resamples and red dot represents the best solution of slip rate and locking depth.

We define a fault perpendicular profile between 37.60 and 39.25 E° as shown in the upper panel and used 45 GPS points as shown in the lower-left panel in Figure 3.12. The lower-middle panel shows profile 9 also is a transition between elastic and plastic deformation zones. Bootstrap error analysis shows a scattered error boundary compared to other profiles. However, our bootstrap analysis resulted in 19.5±0.5 mm/y

slip rate and 17.2±2.4 km locking depth consistent with the neighboring profiles.

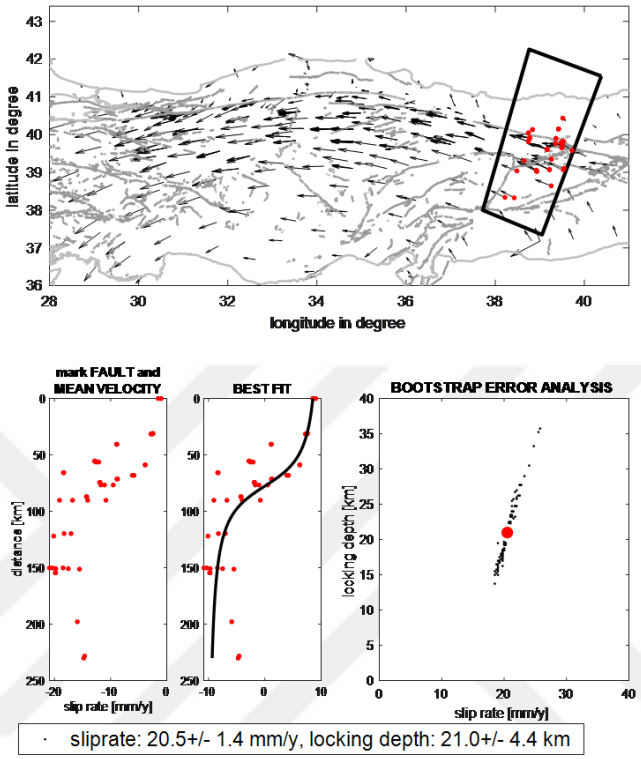

Figure 3.13. Slip and depth in profile 10, upper panel: fault perpendicular profile, lower-left panel: red dots represent GPS points, lower-middle panel: best fitting arctangent curve, lower-right panel: black dots represent bootstrap error analysis for 100 resamples and red dot represents the best solution of slip rate and locking depth.

We define a fault perpendicular profile between 38.76 and 40.38 E° as shown in the upper panel and used 45 GPS points as shown in the lower-left panel in Figure 3.13. The lower-middle panel shows the best fitting arctangent curve that represents the transition from elastic deformation to plastic deformation. We calculated slip rate 20.5±1.4 mm/y and locking depth 21.0±4.4 km for this region. Compared to other profiles, slip rate and locking depth have the biggest error boundary. This is a result of poor and heterogeneous GPS coverage and outlier GPS points in the region. The current incomplete earthquake cycle is initiated in this region with the 1939 Erzincan

(M7.9) earthquake.

Slip rate and locking depth estimates are given below in Table 3.1. Table summarizes that slip is increasing westward. Fault locking depth is not homogeneous everywhere, but it is decreasing eastward on average. We observed that fault is stretching at western segment and the deformation is distributed. However, as we investigate towards the east, stretching is accompanied by the slide, which means deformation is discrete along the fault. Different amounts of internal friction of the fault, different amount of shear stress and, variant lithologic properties of the sides of the fault causes this diverse motion along different profiles. Stretch and slide motions are explained in Figure 3.14 for a right lateral strike-slip fault. In figure, left panel indicates higher slip and deeper locking depth. Right panel indicates that slip and locking depth decreases, consequently strain accumulation decreases too. The transition from stretch to slide is remarkable from the west to the east along the fault. Transition of elastic deformation to plastic deformation is clearly seen in our profiles.

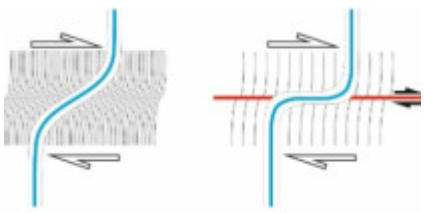

Figure 3.14. Left: elastic deformation by the shear stress, right: stretching and sliding together, blue curve represents deformation, red line represents fault, arrows represent direction of the motion [104].

Table 3.1. Slip and locking depth estimates of 10 profiles along the NAFZ.

Profile No	**Slip Rate (mm)**	**Locking Depth (km)**	**Last Rupture (year)**
1	23.2 ± 0.4	11,2 ± 1,3	1999
2	24.2 ± 0.3	23.8 ± 1.2	1999
3	23.5 ± 0.8	16.5 ± 1.1	1999-1967-1957
4	23.0 ± 0.8	15.8 ± 1.2	1944
5	21.0 ± 0.7	15.0 ± 2.0	1944
6	20.0 ± 0.3	20.0 ± 1.9	1943
7	20.0 ± 0.2	19.0 ± 0.7	1943
8	20.5 ± 0.2	11.5 ± 0.6	1942
9	19.5 ± 0.5	17.2 ± 2.4	1939
10	20.5 ± 1.4	21.0 ± 4.4	1939

4. EARTHQUAKE CYCLE

We test elastic rebound theory for the fault segments that ruptured during the previous successive earthquake cycles of the NAFZ. According to elastic rebound theory, released co-seismic energy must be equivalent to the amount of strain energy that has accumulated on the fault during the inter-seismic period [1]. In this context, we obtained slip rates and locking depths along the fault, and we calculated accumulated slip during the inter-seismic period, then compared them with the observed co-seismic slips. Difference between observed co-seismic and calculated cumulative inter-seismic slips verify the spatiotemporal partitioning between fault creep and locking. This is because the earthquake energy budget of a fault consists of the energy stored on the locked part inside the crust for centuries. The fault stores the strain energy along its locked patches during the time period that they are not creeping. Multiplying the annual slip energy amount with the time since the last major earthquake determines the maximum cumulative slip that can be accumulated along the investigated segment. The misfit between the maximum inter-seismic slip accumulation and the observed co-seismic slip estimates the partitioning between the creep and the locking that occurred in time and space on the segment failed by the two successive earthquakes. This partitioning between the creep and the locking allows estimating the current earthquake potential of the investigated segments.

4.1. Comparison of Inter-seismic Slip Accumulation with Co-seismic Slip Release

We used arctangent modeling approach to obtain slip rates and locking depths along the NAFZ using 10 across-fault profiles. We used estimated slip rates to calculate cumulative slip accumulation along individual rupture zones of the earthquakes that occurred in the current incomplete earthquake cycle. In this context, we determine the corresponding profiles with rupture zones of the last earthquakes, and we distributed slip rates individually for each segment. In a second step, we determine

the particular time between two successive failures of the same rupture zone. Since we estimated annular slip rates, we can calculate cumulative slip between two earthquake cycles. For our calculations, this time is measured from 1666 or 1668 to the last earthquake rupturing the same segment during the current earthquake cycle. We test if accumulated inter-seismic slip since the last complete earthquake cycle is equal to the released energy during the last earthquakes, meaning that the fault segment is locked immediately following the earthquake, or there is a misfit between the accumulated inter-seismic and co-seismic slips, suggesting that the fault segment creeps for a while until it gets locked. Table 4.1 shows inter-seismic, co-seismic, and cumulative slips for different segments.

4.2. Spatio-temporal Partitioning Between Creeping and Locked Stages of the NAFZ

Based on slip accumulation calculations, we determine that different fault segments have different properties of slip accumulation and release durations. Each segment has a different potential to produce co-seismic slip and according to Table 4.2. Every segment produces less dextral offset compared to the maximum potential of accumulated slip. The reason behind that is the segments need a particular time interval to be locked again after a drastic energy released during the earthquake. Until the fault is locked again, we assume that the rocks creep and slide steady state. Creep movements do not release seismic energy, and therefore its duration must be determined to estimate future earthquake potential correctly. This free creeping time is named the post-seismic stage and we calculated the duration of this stage of the fault based on the ratio of accumulated inter-seismic slip and released co-seismic slip for individual segments of the NAFZ. Calculated locking and creeping stages of the NAFZ segments are given in Table 4.2 and shown in Figure 4.1 below.

Table 4.1. Observed co-seismic dextral slip, Estimated annual slip and Preliminary inter-seismic slip deficit along the NAFZ segments.

Year	**Month**	**Day**	**M**	**Oberved co-seismic dextral slip (m)**	**Reference**	**Previous rupture**	**Estimated annual Slip (mm/y)**	**Preliminary[a] inter-seismic slip deficit (m)**
1939	12	26	7.9	4.50	[11]	1666	19.83 ± 0.7	5.41 ± 0.2
1942	12	20	7.1	2.50	[11]	1668	20.00 ± 0.2	5.48 ± 0.1
1943	11	26	7.7	3.80	[11]	1668	13.83 ± 0.4	3.80 ± 0.1
1944	2	1	7.4	3.40	[11]	1668	22.00 ± 0.7	6.07 ± 0.2
1957	5	26	7.0	1.50	[11]	1719	08.10 ± 0.2	1.93 ± 0.1
1967	7	22	7.2	1.65	[11]	1719	08.10 ± 0.2	2.01 ± 0.1
1999	8	17	7.5	3.50	[32]	1719	16.10 ± 0.2	4.51 ± 0.1
1999	11	12	7.1	3.00	[43]	1754	23.70 ± 0.3	5.81 ± 0.1

[a]The cumulative slip deficit without any creeping period

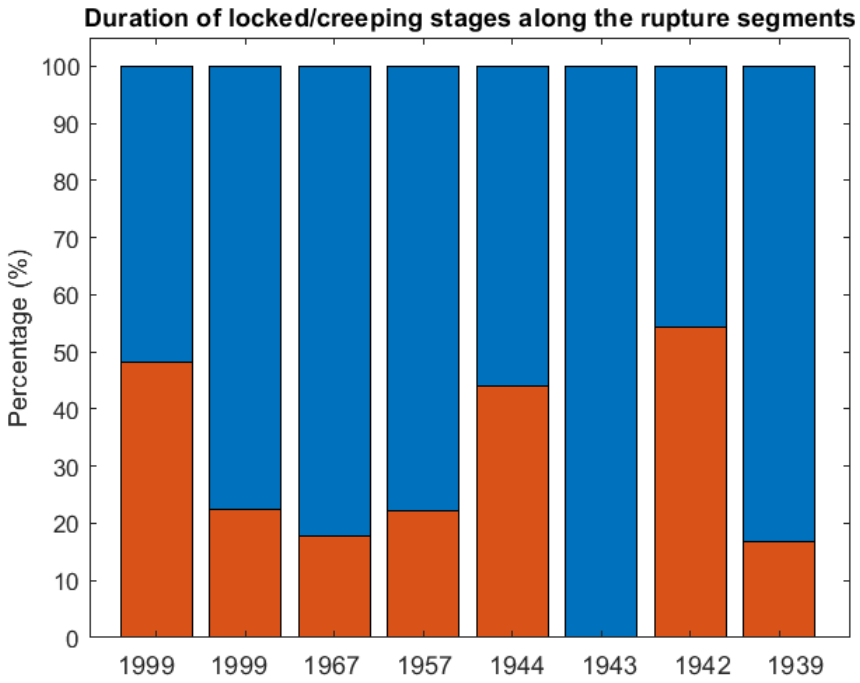

Figure 4.1. Locked/creeping durations along the fault segments; red bars show the creeping stage and blue bars show the locked stage during the seismic cycle.

Table 4.2. Locked and creeping durations of the NAFZ segments.

The date of the last failure of the segment			**Inter-seismic reaction to the tectonic slip on the fault**	
Year	**Month**	**Day**	**Locked (%)**	**Creeping (%)**
1939	12	26	83.1	16.9
1942	12	20	45.6	54.4
1943	11	26	99.9	00.1
1944	2	1	56.0	44.0
1957	5	26	77.8	22.2
1967	7	22	82.1	17.9
1999	8	17	77.6	22.4
1999	11	12	51.7	48.3

4.3. Current Magnitude Potentials along the NAFZ

By determining the duration of creeping/locked stages of the segments, we calculate current earthquake potentials along the NAFZ. The current cumulative slip on a fault segment determines the magnitude of the earthquake it can presently generate.

The moment magnitude (M_w) is the scale that directly quantifies the energy released during an earthquake [44]. This magnitude scale, in contrast to other empirical magnitude scales, describes the earthquake size based on direct physical observations, such as the size of the rupture and the amount of the slip.

Seismic moment (M_0) is the quantity that describes the size of an earthquake based on the rupture plane, the average amount of slip and the shear modulus that is the force overcoming the initial friction of the rocks as explained in Equation 4.1. In this equation, μ is the shear modulus assumed to be 34 GPa for Earth's crust; A is the rupture plane, and it is calculated by the multiplication of rupture length and rupture depth (which we estimated as locking depth); d is the average cumulative slip since the last earthquake in meters.

$$M_0 = \mu * A * d \tag{4.1}$$

M_w is calculated based on the (M_0). It is explained as follows in Equation 4.2 [44].

$$M_w = \frac{2}{3} \log M_0 - 16.1 \tag{4.2}$$

We first re-calculated the magnitudes of earthquakes in the current incomplete earthquake cycle to validate our estimation of post-seismic stages of the fault segments. Our magnitude estimations are consistent with the previous studies as shown in Table 4.3. In this step, we show that elastic rebound theory is applicable only if

partitioning between creeping and locked stages of the fault segments are characterized. If so, it is possible to quantify cumulative slip along the fault segments and therefore forecast the magnitude of future earthquakes.

Table 4.3 lists the current earthquake potential of each segment along the NAFZ. As shown in the table, different segments have the potential to generate earthquakes in different sizes. Our results indicate that the 1939 rupture has currently the potential to generate M7.6 earthquakes at the eastern edge of the NAFZ. The 1942 rupture has the potential only to produce M6.9 earthquakes. The 1943 and the 1944 ruptures have currently the potential to generate M7+ earthquakes along the central NAFZ. Along the western NAFZ, the 1957, 1967, 1999 ruptures have the potential to generate only M6.5+ earthquakes.

Table 4.3 summarizes that the current maximum cumulative slip (tectonic loading amount) varies over the segments of NAFZ. Despite this variation, the entire NAFZ has the potential to generate M6.0 + earthquakes. Eastern segments accumulated energy in a longer inter-seismic time compared to the western segments. As a result, the current maximum cumulative slip decreases to the west, and therefore earthquake potential tends to decrease from east to west.

Table 4.3. Future earthquake potentials along the NAFZ segments.

Segment	**Month**	**Day**	**Reference**	**Current Maximum Cumulative Slip (m)**	**Future EQ Potential (M_w)**
1939	12	26	[11]	1.50	7.6
1942	12	20	[11]	0.72	6.9
1943	11	26	[11]	1.08	7.3
1944	2	1	[11]	0.95	7.2
1957	5	26	[11]	0.40	6.5
1967	7	22	[11]	0.36	6.8
1999	8	17	[32]	0.28	6.8
1999	11	12	[43]	0.27	6.4

5. DISCUSSIONS

Our model shows that the annual slip rate is not uniform along the NAFZ indicating a systematic east-to-west increase (Figure 5.1). This increase is supported by the results we compiled from previous studies (Appendix C). Slip rate might vary along the fault zone as it depends on variable features such as the operation age, geometry of the fault, rheology and elasticity of the Crust, liquid and heat flow beneath [45].

Previous studies investigating the slip rates shows that the paleo-slip rates are considerably lower (30%) than the geodetic slip rates. This was interpreted to represent the post-seismic healing process discharging the tectonic loading for a specific time period after the major earthquakes, noting that the intraplate deformation should be taken into account [18, 46, 47].

However, previous geologic and geodetic studies mainly exhibited the systematic east-to-west increase of slip rates along the NAFZ as shown in Figure 5.1. They explained that slip variations along the NAFZ mainly depend on two neo-tectonic settings since late Miocene; push of the Arabian plate from south-east to north-west with 20±3 mm/y rate at the eastern part of the Anatolian plate; and pull of Hellenic Arc placed under the Mediterranean Sea at the western part of the Anatolian plate with the extension rate 14±5 mm/y [4, 48]. The evolution of the NAFZ depends on these plate tectonics and being the transform boundary between Eurasia and Anatolian plates, tectonic push and pull forces cause the Anatolian plate to move westward with respect to the Eurasian plate with an approximate slip rate of 24 - 26 mm/y [3, 5, 25, 49, 50]. Eastern NAFZ exhibits a linear and well-developed fault trace compared to western NAFZ that splayed into many branches. Discontinuities such as fault step overs are interpreted to represent lower slip rates along the eastern segments compared to the western segments [5, 13].

In summary, there is an east-to-west systematic increase in slip rates along the

NAFZ, verified by the results we compiled from the previous studies (Appendix C). We interpret that slip variation along the NAFZ probably depends on the tectonic settings of Anatolian plate, the fault age and geometry that is not linear and well-developed at every longitude. Slip rate variation from east to west is a result of coherent plate rotation and various fault mechanisms evolved on the different sub-segments. The NAFZ sub-segments produce systematically increasing slip rates from east to west in the range of 19.5±0.5 – 24.2±0.3 mm/y. In future studies, fault geometry and segmentation could be examined to better characterize slip rate variation.

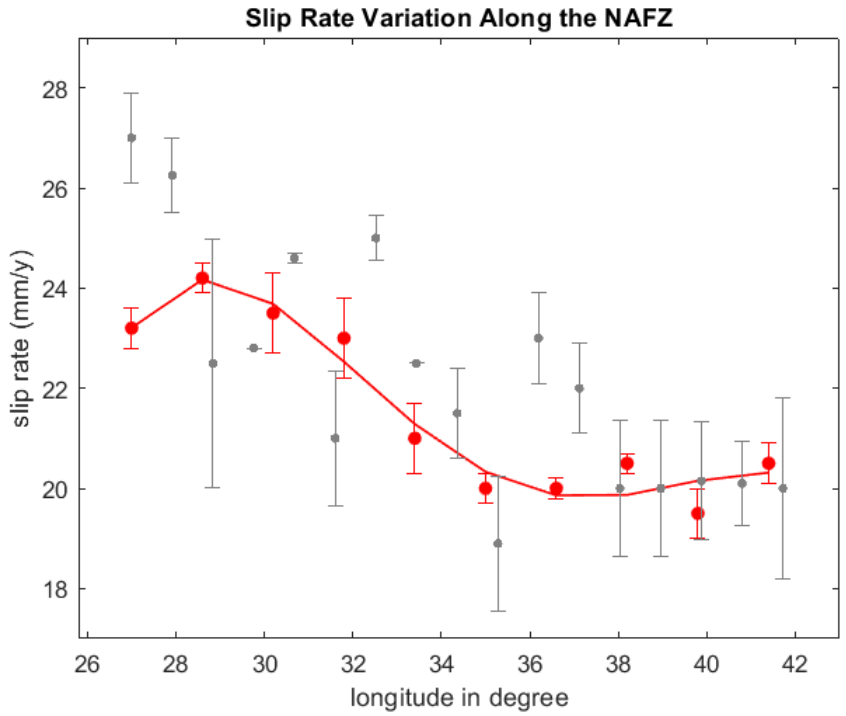

Figure 5.1. Slip rate variations along the NAFZ (red dots are slip rate estimations of this study, red line shows the increment trend from east to west, gray dost are slip rate estimations from others).

Similar to the slip rate, locking depth varies along the NAFZ. Locking depth is a parameter that mostly depends on the transition between brittle and ductile zones of the crust. However, crustal thickness, and therefore the depth of this transition is not homogeneous along the NAFZ. Our GPS derived locking depth results have relatively

larger error bounds compared to slip rates. However, even in these error bounds, it is clear that the locking depth tends to be deeper along central NAFZ. It shows its deepest depths at the 28 – 30 E$^\circ$ longitudes as shown in Figure 5.2. The eastern NAFZ also has a relatively deeper locking depth compared to other segments. But at 38°E longitude and at western segment between 26 – 28°E, it drastically decreases. Previous studies also suggested a variety of locking depths for the eastern, the central, and the western NAFZ (Appendix C). We compiled the locking depth estimations from previous studies as shown in Figure 5.2. Previous studies argue that the locking depth has an increasing trend along the central NAFZ, while it varies at eastern and western segments. Locking depth variations is a result of crust thickness. Crustal thickness is 30 km assumed to be on average, and the seismo-genic zone is assumed to be thinner for North Anatolia [35,51]. However, its thickness differs from east to west, and it is greater in eastern Anatolia [52]. Our results indicate that the locking depths tend to increase through central NAFZ, it is above the average on eastern NAFZ, are the highest at the 28 – 30 E$^\circ$ and the lowest at the 26 – 28 E$^\circ$. Shallow locking depths that we estimate can be due to the NAFZ being within the early inter-seismic period of the earthquake cycle, as the locking depth increases throughout the seismic cycle [53]. Additionally, it should be considered that the NAFZ exhibits aseismic creep at shallow depths especially along the 1944 earthquake rupture zone around 29 – 30 E$^\circ$ longitudes.

The 10 profiles we analyzed revealed that the fault zone accommodates both elastic and plastic deformation. However, the profiles showed deformation amount substantially vary through the sub-segments. For example, profile 2, (28 - 30° longitudes) shows the highest elastic deformation, as well as profile 3 (28 - 30° longitudes), compared to others. It is seen that the slip rate is also the highest at this profile. Because the NAFZ is at a different stage of the seismic cycle at different sub-segments, which leads to different fault coupling rates, deformation types vary tending to be plastic at currently creeping-like segments, or elastic at currently locked segments.

Our results reveal that the inter-seismic slip storage does not match perfectly with

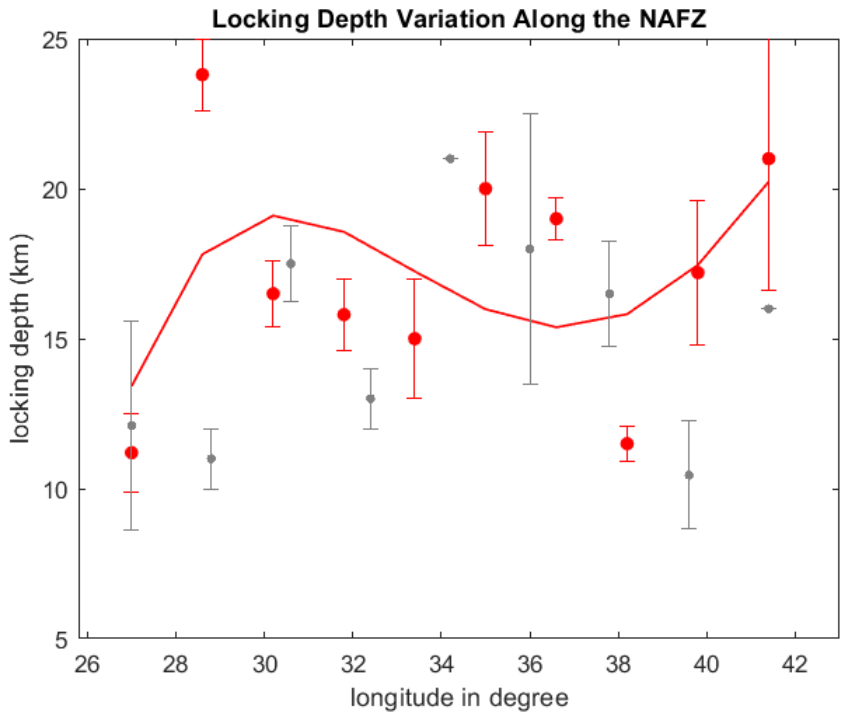

Figure 5.2. Locking depth variations along the NAFZ (red dots are locking depth estimations of this study, red line shows the decrease trend from east to west, gray dost are locking depth estimations from others).

the co-seismic slip release without a sliding post-seismic stage. We calculated that the NAFZ locks in different time amounts after a major earthquake. Exceptionally, the NAFZ immediately locks after a major earthquake along the 1943 (M7.7) rupture zone. The 1939 (M7.9), 1957 (M7.0), 1967 (M7.2), 1999 (M7.5) rupture zones, however, are locked after a certain amount of time following the earthquakes. On the other hand, the 1942 (M7.1), 1944 (M7.4), 1999 (M7.1) rupture zones have relatively longer post-seismic duration. On average, the NAFZ continues to creep after a major earthquake for the 57,38% of the time period between two successive earthquakes rupturing the same fault section, basically the entire earthquake cycle. Post-seismic deformation along the NAFZ is investigated by previous studies. NAFZ western segment was monitored for 7 years and a post-seismic creep is determined 10 – 12 mm/y [54]. Logarithmically decaying post-seismic afterslip at a significant level 10 – 15 mm/y, after 20 years of 1999 (M7.5) earthquake at the western NAFZ is also determined [55]. Studies suggest that after the major earthquakes, fault creep continues until the post-seismic relaxation time is complete. However, temporal resolution and extend of these studies are not enough to investigate the partitioning between creep and locked, in other words, between post-seismic and co-seismic stages along with the entire earthquake cycle.

Our study reveals that elastic rebound theory represent the entire generation processes of an earthquake only if durations of post-seismic and inter-seismic stages are determined reasonably. According to elastic rebound theory, inter-seismic energy released with an immediate co-seismic rupture. Using historical earthquake records as well as GPS slip rates, our results validated that the difference between the released co-seismic slip and cumulative inter-seismic slip gives the duration of post-seismic stage. Because post-seismic duration varies along the fault, determining this parameter separately for every fault section allowed us to better forecast produce future earthquake potentials for sub-segments.

As one of the major outcomes of this study, we verified the present state of the NAFZ in terms of inter-seismic slip accumulation and future earthquake potential. Currently, the NAFZ segments have the potential to produce M7+ earthquakes along

1939 (M7.9), 1943 (M7.7) and 1944 (M7.4) earthquakes' rupture zone. Moreover, 1942 (M7.1), 1957 (M7.0), 1967 (M7.2) and 1999 (M7.5) segments have the potential to produce M6.5+ earthquakes. 1999 (M7.1) segment currently has the potential to produce M6+ earthquake. Considering the population distribution along the NAFZ and the current earthquake potentials, the NAFZ earthquake hazard needs further investigation in light of our results.

In this study, we investigated four earthquake cycles along the NAFZ, and calculated the cycle duration using paleo, historical and instrumental records. Our results verify the previous observation of east-to-west systematic failure of NAFZ [9, 10, 29, 56–58]. We reveal the failure of the NAFZ will be complete in 239±3 years in the west and will probably restart from the easternmost segment again. Thus, the NAFZ has stochastically a potential to produce major earthquakes along the NAF, especially along its western segments that have not been reactivated for the last 250 years, before its current incomplete earthquake cycle is finished [39, 59].

Additionally, as our results indicate, slip rate and locking depth, as well as post-seismic duration vary along the fault, verifying the sub-segmentation of the NAFZ. For this reason, investigating the sub-segments of the NAFZ is indispensable to elaborate on potential of future earthquakes along the entire fault. To achieve successful forecasting of future earthquakes, we determined durations of post- and inter-seismic stages investigating the partitioning between creep and fault locking in time and space. We determined the post-seismic duration of the fault segments along the entire NAFZ and have observed that some of the fault segments that failed during the current incomplete cycle have already started to accumulate inter-seismic energy while some segments are still in post-seismic stage.

6. CONCLUSION

We investigated the earthquake cycle along the NAFZ, focusing on the rupture zone of the 1668 Great Anatolian Earthquake based on the historical earthquake records we compiled as well as the GPS measurements we modeled. In this context, we tested elastic rebound theory and earthquake generation processes investigating the partitioning between the creeping post-seismic stage and locked inter-seismic stage.

Based on the misfits between released co-seismic slips and presumed cumulative inter-seismic slip storage, we observed that the fault segments do not spend the entire seismic cycle in the fully-locked stage.

Only in one case, along the 1943 rupture zone, a very short part of the seismic cycle was in the creeping stage (0.1%). Along the 1939 (M7.9), 1957 (M7.0), 1967 (M7.2), and 1999 (M7.5) rupture zones, creeping stage played non-negligibly major role (16.9%, 22.2%, 17.9% and 22.4%, respectively). Along the 1942 (M7.1), 1944 (M7.4), 1999 (M7.1) rupture zones, creeping stage played substantially major role (54.4%, 44.0% and 48.3%, respectively).

The segments have currently different earthquake potentials as they have different creeping-locking rates throughout the seismic cycle although they are exposed to similar tectonic deformation rates (ranging between 19.5±0.5 – 24.2±0.3 mm/y).

Currently, the NAFZ segments have the potential to produce M7+ earthquakes along the 1939 (M7.9), 1943 (M7.7), and 1944 (M7.4) rupture zones. Moreover, the 1942 (M7.1), 1957 (M7.0), 1967 (M7.2), and 1999 (M7.5) rupture zones have the potential to produce M6.5+ earthquakes. The 1999 (M7.1) rupture zone currently has the potential to produce an M6+ earthquake.

GPS-derived slip rates on the individual fault segments indicate and east-to-west

acceleration along the NAFZ. GPS-derived locking depths, however, do not outline a clear trend. They are deeper along the Central NAFZ.

Space-time relation between the historical earthquakes indicates that the NAFZ fails through east-to-west migrating and decelerating earthquakes. Complete failure of the NAFZ lasts 239±3 years based on the historical data we analyzed covering the last three complete and currently incomplete seismic cycles.

REFERENCES

1. Reid, H. F., "Elastic rebound theory", *University of California Publ, Bulleetin of Deptartment of Geo. Sci.*, Vol. 6, pp.413-433, 1910.

2. Field, E. H., "Aftershock statistics constitute the strongest evidence for elastic rebound in large earthquakes?", In *AGU fall meeting abstracts,* Vol. 2011, pp. S22B-08, 2011.

3. McClusky, S., S. Balassanian, A. Barka, C. Demir, S. Ergintav, I. Georgiev, O. Gurkan, M. Hamburger, K. Hurst, H. Kahle, K. Kastens, G. Kekelidze, R. King, V. Kotzev, O. Lenk, S. Mahmoud, A. Mishin, M. Nadariya, A. Ouzounis, D. Paradissis, Y. Peter, M. Prilepin, R. Reilinger, I. Sanli, H. Seeger, A. Tealeb, M. N. Toksöz, and G. Veis, "Global Positioning System constraints on plate kinematics and dynamics in the eastern Mediterranean and Caucasus", *Journal of Geophysical Research*, Vol. 105, No. B3, pp. 5695–5719, 2000.

4. Reilinger, R., S. McClusky, P. Vernant, S. Lawrence, S. Ergintav, R. Cakmak, H. Ozener, F. Kadirov, I. Guliev, R. Stepanyan, M. Nadariya, G. Hahubia, S. Mahmoud, K. Sakr, A. ArRajehi, D. Paradissis, A. Al-Aydrus, M. Prilepin, T. Guseva, E. Evren, A. Dmitrotsa, S. V. Filikov, F. Gomez, R. Al-Ghazzi, and G. Karam, "GPS constraints on continental deformation in the Africa-arabia-eurasia continental collision zone and implications for the dynamics of plate interactions", *Journal of Geophysical Research*: Solid Earth, Vol. 111, No. B5, 2006.

5. Bohnhoff, M., P. Martínez-Garzón, F. Bulut, E. Stierle, and Y. Ben-Zion, "Maximum earthquake magnitudes along different sections of the North Anatolian Fault Zone", *Tectonophysics*, Vol. 674, pp. 147–165, 2016.

6. Kagan, Y., and D. D. Jackson, "Long-term earthquake clustering", *Geophysical Journal International*, Vol. 104, No. 1, pp. 117–134, 1991.

7. Kasahara, K., "Earthquake mechanics", Cambridge University Press, *Geological Magazine*, Vol. 119, No. 4, pp. 423–423, 1982.

8. Mogi, K., W. Thatcher, "Seismology in Japan: earthquake prediction", *Science*, Vol. 232, No. 4748, pp. 408–409, 1986.

9. Bulut, F. and A. Doğru, "Time Frame for future large earthquakes near İstanbul based on east-to-west decelerating failure of the North Anatolian Fault", *Turkish Journal of Earth Sciences*, Vol. 30, No. 2, pp. 204–214, 2021.

10. Toksöz, M. N., A. F. Shakal, and A. J. Michael, "Space-time migration of earthquakes along the North Anatolian Fault Zone and seismic gaps", *Earthquake Prediction and Seismicity Patterns*, pp. 1258–1270, 1979.

11. Barka, A., "Slip distribution along the North Anatolian fault associated with the large earthquakes of the period 1939 to 1967", *Bulletin of the Seismological Society of America*, Vol. 86, No. 5, pp. 1238-1254, 1996.

12. Ambraseys, N. N., and J. A. Jackson, "Faulting associated with historical and recent earthquakes in the Eastern Mediterranean region", *Geophysical Journal International*, Vol. 133, No. 2, pp. 390–406, 1998.

13. Emre, Ö., H. Kondo, S. Özalp, and H. Elmacı, "Fault geometry, segmentation and slip distribution associated with the 1939 erzincan earthquake rupture along the North Anatolian Fault, Turkey", *Geological Society, London, Special Publications*, Vol. 501, No. 1, pp. 23–70, 2020.

14. Zabci, C., H. S. Akyüz,V. Karabacak, T. Sançar, E. Altunel, H. Gürsoy, and O. Tatar, "Palaeoearthquakes on the Kelkit Valley segment of the North Anatolian Fault, Turkey: Implications for the surface rupture of the historical 17 August 1668 Anatolian earthquake", *Turkish Journal of Earth Sciences*, Vol. 20, No. 4, pp. 411-427, 2011.

15. Ambraseys, N. N., and C. F. Finkel, "The Anatolian earthquake of 17 August 1668", In *Symposium on historical seismograms and earthquakes*, pp. 173-180, 1988.

16. Ambraseys, N. N., and C. F. Finkel, *The seismicity of Turkey and adjacent areas: A historical review, 1500-1800.* Istanbul: Eren, 1995.

17. Ambraseys, N N., "The seismic activity of the Marmara Sea region over the last 2000 Years", *Bulletin of the Seismological Society of America*, Vol. 92, No. 1, pp. 1–18, 2002.

18. Hubert-Ferrari, A., R. Armijo, G. King, B. Meyer, and A. Barka, "Morphology, displacement, and slip rates along the North Anatolian Fault, Turkey", *Journal of Geophysical Research: Solid Earth*, Vol. 107, No. B10, 2002.

19. Zabci, C., V. Karabacak, T. Sancar, H. S. Akyüz, E. Altunel, H. Gürsoy, and O. Tatar, "The possible eastward continuation of the 17 August 1668 Anatolian earthquake on the North Anatolian Fault (NAF), Turkey", In *Geophys. Res. Abstracts*, Vol. 10, 2008.

20. Bakun, W. U., and C. M. Wentworth, "Corrections to 'estimating earthquake location and magnitude from seismic intensity data", *Open-File Report,* 1998.

21. Kreemer, C., G. Blewitt, and E. C. Klein, "A geodetic plate motion and global strain rate model", *Geochemistry, Geophysics, Geosystems*, Vol. 15, No. 10, pp. 3849–3889, 2014.

22. Aktuğ, B., A. Doğru, H. Özener, and M. Peyret, "Slip rates and locking depth variation along Central and easternmost segments of North Anatolian Fault", *Geophysical Journal International*, Vol. 202, No. 3, pp. 2133–2149, 2015.

23. Özdemir, S., "TUSAGA ve TUSAGA-Aktif istasyonlarının hassas koordinat ve hızlarının hesaplanması üzerine", *Harita Dergisi*, Vol. 155, pp. 53-81, 2016.

24. Yavaşoğlu, H. H., M. N. Alkan, S. Bilgi, and Ö. Alkan, "Monitoring aseismic creep trends in the İsmetpaşa and Destek segments throughout the North Anatolian Fault (NAF) with a large-scale GPS network", *Geoscientific Instrumentation, Methods and Data Systems*, Vol. 9, No. 1, pp. 25–40, 2020.

25. Aktug, B., J. M. Nocquet, A. Cingöz, B. Parsons, Y. Erkan, P. England, O. Lenk, M. A. Gürdal, A. Kilicoglu, H. Akdeniz, and A. Tekgül, "Deformation of western Turkey from a combination of permanent and campaign GPS data: Limits to block-like behavior", *Journal of Geophysical Research*, Vol. 114, No. B10, 2009.

26. Aktuğ, B., E. Parmaksız, M. Kurt, O. Lenk, A. Kılıçoğlu, M. A. Gürdal, and S. Özdemir, "Deformation of central anatolia: GPS implications", *Journal of Geodynamics*, Vol. 67, pp. 78–96, 2013.

27. Nocquet, J. M. J.-M. Nocquet, "Present-day kinematics of the Mediterranean: A comprehensive overview of GPS results", *Tectonophysics*, Vol. 579, pp. 220–242, 2012.

28. Dor, O., C. Yıldırım, T. K. Rockwell, Y. Ben-Zion, O. Emre, M. Sisk, and T. Y. Duman, "Geological and geomorphologic asymmetry across the rupture zones of the 1943 and 1944 earthquakes on the North Anatolian Fault: Possible signals for preferred earthquake propagation direction", *Geophysical Journal International*, Vol. 173, No. 2, pp. 483–504, 2008.

29. Stein, R. S., A. A. Barka, and J. H. Dieterich, "Progressive failure on the North Anatolian Fault since 1939 by earthquake stress triggering", *Geophysical Journal International*, Vol. 128, No. 3, pp. 594–604, 1997.

30. Kondo, H., Y. Awata, O. Emre, A. Dogan, S. Özalp, F. Tokay, and C. Yıldırım, "Re-evaluation of Fault Geometry and Slip Distribution of the 1944 Bolu-Gerede Earthquake Rupture, North Anatolian Fault System, Turkey", In *AGU Fall Meeting Abstracts* Vol. 2002, pp. S11B-1154, 2002.

31. Kondo, H., "Slip distribution, fault geometry, and Fault Segmentation of the 1944 bolu-gerede earthquake rupture, North Anatolian Fault, Turkey", *Bulletin of the Seismological Society of America*, Vol. 95, No. 4, pp. 1234–1249, 2005.

32. Barka, A., "The surface rupture and slip distribution of the 17 August 1999 Izmit earthquake (M 7.4), North Anatolian fault", *Bulletin of the Seismological Society of America*, Vol. 92, No. 1, pp. 43–60, 2002.

33. Çakır, Z., J.-B. de Chabalier, R. Armijo, B. Meyer, A. Barka, and G. Peltzer, "Coseismic and early post-seismic slip associated with the 1999 Izmit earthquake (Turkey), from SAR interferometry and tectonic field observations", *Geophysical Journal International*, Vol. 155, No. 1, pp. 93–110, 2003.

34. Aktar, M., S. Özalaybey, M. Ergin, H. Karabulut, M.-P. Bouin, C. Tapırdamaz, F. Biçmen, A. Yörük, and M. Bouchon, "Spatial variation of aftershock activity across the rupture zone of the 17 August 1999 Izmit earthquake, Turkey", *Tectonophysics*, Vol. 391, No. 1-4, pp. 325–334, 2004.

35. Bulut, F., M. Bohnhoff, W. L. Ellsworth, M. Aktar, and G. Dresen, "Microseismicity at the North Anatolian Fault in the Sea of Marmara Offshore Istanbul, NW Turkey", *Journal of Geophysical Research*, Vol. 114, No. B9, 2009.

36. Ergin, K., "A catalogue of earthquakes for Turkey and surrounding area (11AD to 1964AD)", *Tech. Univ. Mining Eng. Fac. Publ.*, Vol. 24, No. 189, 1967.

37. Soysal, H., D. Kolçak, and S. Sipahioğlu, "Some aspects of the North Anatolian Fault Zone derived from the comparison of its instrumental data with historical information", *Multidisciplinary Approach to Earthquake Prediction,* pp. 223–238, 1982.

38. Kase, Y., H. Kondo, and Ö. Emre, "Dynamic rupture process of the great 1668 Anatolian earthquake", In *EGU General Assembly Conference Abstracts*, p. 6520, 2010.

39. Bulut, F., B. Aktuğ, C. Yaltırak, A. Doğru, and H. Özener, "Magnitudes of future large earthquakes near Istanbul quantified from 1500 years of historical earthquakes, present-day microseismicity and GPS slip rates", *Tectonophysics*, Vol. 764, pp. 77–87, 2019.

40. Savage, J. C., and R. O. Burford, "Geodetic determination of relative plate motion in Central California", *Journal of Geophysical Research*, Vol. 78, No. 5, pp. 832–845, 1973.

41. Savage, J. C., "A dislocation model of strain accumulation and release at a subduction zone", *Journal of Geophysical Research: Solid Earth*, Vol. 88, No. B6, pp. 4984–4996, 1983.

42. Doğru, A., F. Bulut, C. Yaltırak, and B. Aktuğ, "Slip distribution of the 2020 Elazığ earthquake (MW 6.75) and its influence on earthquake hazard in the Eastern Anatolia", *Geophysical Journal International*, Vol. 224, No. 1, pp. 389–400, 2020.

43. Akyuz, H. S., "Surface rupture and slip distribution of the 12 November 1999 duzce earthquake (M 7.1), North Anatolian Fault, Bolu, Turkey", *Bulletin of the Seismological Society of America*, Vol. 92, No. 1, pp. 61–66, 2002.

44. Hanks, T. C., and H. Kanamori, "A moment magnitude scale", *Journal of Geophysical Research*, Vol. 84, No. B5, p. 2348, 1979.

45. Şengör, A. M. C., O. Tüysüz, C. İmren, M. Sakınç, H. Eyidoğan, N. Görür, X. Le Pichon, and C. Rangin, "The North Anatolian Fault: A new look", *Annual Review of Earth and Planetary Sciences*, Vol. 33, No. 1, pp. 37–112, 2005.

46. Kuşçu, I., "Geologic evidence for five large earthquakes on the north Anatolian fault at Ilgaz, during the last 2000 years--a result of GSJ-MTA international cooperative research", In *Program of Workshop on Paleoseismology*, p. 66, 1999.

47. Kozacı, Ö., J. F. Dolan, and R. C. Finkel, "A late holocene slip rate for the central North Anatolian fault, at Tahtaköprü, Turkey, from Cosmogenic 10be

geochronology: Implications for fault loading and strain release rates", *Journal of Geophysical Research: Solid Earth*, Vol. 114, No. B1, 2009.

48. Hussain, E., T. J. Wright, R. J. Walters, D. P. Bekaert, R. Lloyd, and A. Hooper, "Constant strain accumulation rate between major earthquakes on the North Anatolian Fault", *Nature Communications*, Vol. 9, No. 1, 2018.

49. Barka, A., and R. Reilinger, "Active tectonics of the Eastern Mediterranean Region: Deduced from GPS, neotectonic and Seismicity Data", *Annals of Geophysics*, Vol. 40, No. 3, 1997.

50. Reilinger, R. E., S. C. McClusky, M. B. Oral, R. W. King, M. N. Toksoz, A. A. Barka, I. Kinik, O. Lenk, and I. Sanli, "Global Positioning System measurements of present-day crustal movements in the arabia-africa-eurasia plate collision zone", *Journal of Geophysical Research: Solid Earth*, Vol. 102, No. B5, pp. 9983–9999, 1997.

51. Bulut, F., M. Bohnhoff, M. Aktar, and G. Dresen, "Characterization of aftershock-fault plane orientations of the 1999 ïzmit (Turkey) earthquake using high-resolution aftershock locations", *Geophysical Research Letters*, Vol. 34, No. 20, 2007.

52. Kahraman, M., D. G. Cornwell, D. A. Thompson, S. Rost, G. A. Houseman, N. Türkelli, U. Teoman, S. Altuncu Poyraz, M. Utkucu, and L. Gülen, "Crustal-scale shear zones and heterogeneous structure beneath the North Anatolian Fault Zone, Turkey, revealed by a high-density seismometer array", *Earth and Planetary Science Letters*, Vol. 430, pp. 129–139, 2015.

53. Savage, J. C., and M. Lisowski, "Viscoelastic coupling model of the San Andreas Fault along the Big Bend, Southern California", *Journal of Geophysical Research: Solid Earth*, Vol. 103, No. B4, pp. 7281–7292, 1998.

54. Ergintav, S., S. McClusky, E. Hearn, R. Reilinger, R. Cakmak, T. Herring, H. Ozener, O. Lenk, and E. Tari, "Seven years of postseismic deformation following

the 1999,M= 7.4 andm= 7.2, Izmit-Düzce, Turkey earthquake sequence", *Journal of Geophysical Research*, Vol. 114, No. B7, 2009.

55. Özarpacı, S., U. Doğan, S. Ergintav, Z. Çakır, A. Özdemir, M. Floyd, and R. Reilinger, "Present GPS velocity field along 1999 izmit rupture zone: Evidence for continuing afterslip 20 yr after the earthquake", *Geophysical Journal International*, Vol. 224, No. 3, pp. 2016–2027, 2020.

56. Klinger, Y., "Paleoseismic evidence of characteristic slip on the western segment of the North Anatolian Fault, Turkey", *Bulletin of the Seismological Society of America*, Vol. 93, No. 6, pp. 2317–2332, 2003.

57. Rockwell, T., D. Ragona, G. Seitz, R. Langridge, M. E. Aksoy, G. Ucarkus, M. Ferry, A. J. Meltzner, Y. Klinger, M. Meghraoui, D. Satir, A. Barka, and B. Akbalik, "Palaeoseismology of the North Anatolian Fault near the Marmara Sea: Implications for fault segmentation and seismic hazard", *Geological Society, London, Special Publications*, Vol. 316, No. 1, pp. 31–54, 2009.

58. Yamasaki, T., T. J. Wright, and G. A. Houseman, "Weak ductile shear zone beneath a major strike-slip fault: Inferences from earthquake cycle model constrained by geodetic observations of the western North Anatolian fault zone", *Journal of Geophysical Research: Solid Earth*, Vol. 119, No. 4, pp. 3678–3699, 2014.

59. Parsons, T., "Recalculated probability OFM≥ 7 earthquakes beneath the Sea of Marmara, Turkey", *Journal of Geophysical Research: Solid Earth*, Vol. 109, No. B5, 2004.

60. Guidoboni, E., and A. Comastri, *Catalogue of Earthquakes and Tsunamis in the Mediterranean Area from the 11th to the 15th Century*, Istituto nazionale di geofisica e vulcanologia, Rome, 2005.

61. Başarır Baştürk, N., and N. M. Özel, "A Compilation of the Historical Earthquakes Database for Marmara Region from 2000 B.C. and 1900 A.D. in frame of Marsite and Mardim Projects", 2016.

62. Papazachos, B. C., "Seismicity of the Aegean and surrounding area", *Tectonophysics*, Vol. 178, No. 2-4, pp. 287–308, 1990.

63. Tan, O., M. C. Tapirdamaz, and A. Yörük, "The earthquake catalogues for Turkey", *Turkish Journal of Earth Sciences*, Vol. 17, No. 2, pp. 405-418. 2008.

64. Grünthal, G., C. Bosse, S. Sellami, D. Mayer-Rosa, and D. Giardini, "Compilation of the GSHAP regional seismic hazard for Europe, Africa and the Middle East", *Annals of Geophysics*, Vol. 42, No. 6, 1999.

65. Yaltırak, C., "Marmara Denizi ve çevresinde tarihsel depremlerin yerleri ve anlamı", *İTÜ Vakfi Dergisi*, 2015.

66. Ambraseys, N., *Earthquakes in the Mediterranean and Middle East: a multidisciplinary study of seismicity up to 1900*, Cambridge University Press, 2009.

67. Hartleb, R. D., "A 2000-year-long paleoseismologic record of earthquakes along the central North Anatolian fault, from trenches at Alayurt, Turkey", *Bulletin of the Seismological Society of America*, Vol. 93, No. 5, pp. 1935–1954, 2003.

68. Gutzwiller, O. W., *Beiträge zur geologie der umgebung von merfete am Marmara-Meere*, Universitat Basel, 1921.

69. Hartleb, R. D., J. F. Dolan, O. Kozaci, H. S. Akyuz, and G. G. Seitz, "A 2500-yr-long paleoseismologic record of large, infrequent earthquakes on the North Anatolian Fault at Cukurcimen, Turkey", *Geological Society of America Bulletin*, Vol. 118, No. 7-8, pp. 823–840, 2006.

70. Fraser, J., J. S. Pigati, A. Hubert-Ferrari, K. Vanneste, U. Avsar, and S. Altinok, "A 3000-year record of ground-rupturing earthquakes along the central North Anatolian fault near Lake Ladik, Turkey", *Bulletin of the Seismological Society of America*, Vol. 99, No. 5, pp. 2681–2703, 2009.

71. Avşar, U., *Lacustrine paleoseismic records from the North Anatolian Fault,* Ph.D dissertation, Ghent University, 2013.

72. Zabcı, C., *Dokurcun-beldibi (adapazarı) Arasının Morfotektonik Ve Paleosismolojik Özellikleri*, M.S. thesis, Eurasia Institute of Earth Sciences, Istanbul Technical University, 2005.

73. Pucci, S., P. M. De Martini, and D. Pantosti, "Preliminary slip rate estimates for the düzce segment of the North Anatolian Fault Zone from offset geomorphic markers", *Geomorphology*, Vol. 97, No. 3-4, pp. 538–554, 2008.

74. Dikbaş, A., H. S. Akyüz, M. Meghraoui, M. Ferry, E. Altunel, C. Zabcı, R. Langridge, and C. Ç. Yalçıner, "Paleoseismic history and slip rate along the Sapanca-akyazı segment of the 1999 İzmit earthquake rupture (M W = 7.4) of the North Anatolian Fault (Turkey)", *Tectonophysics*, Vol. 738-739, pp. 92–111, 2018.

75. Palyvos, N., D. Pantosti, C. Zabci, and G. D'Addezio, "Paleoseismological evidence of recent earthquakes on the 1967 Mudurnu Valley earthquake segment of the North Anatolian Fault Zone", *Bulletin of the Seismological Society of America*, Vol. 97, No. 5, pp. 1646–1661, 2007.

76. Fraser, J., K. Vanneste, and A. Hubert-Ferrari, "Recent behavior of the North Anatolian Fault: Insights from an integrated paleoseismological data set", *Journal of Geophysical Research*, Vol. 115, No. B9, 2010.

77. Gökten, E., V. Özaksoy, and R. Demirtas, "Some neotectonical properties of the North Anatolian fault zone between bayramoren-abant (Turkey)", in *Active Tectonic Research Group first meeting proceeding,* pp. 68-77.

78. Fraser, J. G., A. Hubert-Ferrari, K. Verbeeck, D. Garcia Moreno, U. Avşar, N. Maricq, A. Coudijzer, N. Vlamynck, and K. Vanneste, "A 3000-year record of surface-rupturing earthquakes at Günalan: Variable Fault-rupture lengths along the 1939 erzincan earthquake-rupture segment of the North Anatolian Fault, Turkey", *Annals of Geophysics*, Vol. 55, No. 5, 2013.

79. Hubert-Ferrari, A., U. Avşar, M. El Ouahabi, G. Lepoint, P. Martinez, and N. Fagel, "Paleoseismic record obtained by coring a sag-pond along the North Anatolian Fault (Turkey)", *Annals of Geophysics*, vol 55, No. 5, pp. 929-953, 2013.

80. Meghraoui, M., M. E. Aksoy, H. S. Akyüz, M. Ferry, A. Dikbaş, and E. Altunel, "Paleoseismology of the North Anatolian Fault at Güzelköy (Ganos segment, Turkey): Size and recurrence time of earthquake ruptures west of the Sea of Marmara", *Geochemistry, Geophysics, Geosystems*, Vol. 13, No. 4, 2012.

81. McHugh, C. M., L. Seeber, M. Cormier, J. Dutton, N. Cagatay, A. Polonia, W. Ryan, And N. Gorur, "Submarine earthquake geology along the North Anatolia Fault in the Marmara Sea, Turkey: A model for transform basin sedimentation", *Earth and Planetary Science Letters*, Vol. 248, No. 3-4, pp. 661–684, 2006.

82. Komut, T., and E. Karabudak, "Paleo-earthquake evidence and earthquake recurrence for Düzce Fault, Turkey", 2021.

83. Özalp, S., A. Kürçer, E. Özdemir, and T. Y. Duman, "The Bekten Fault: The palaeoseismic behaviour and kinematic characteristics of an intervening segment of the North Anatolian Fault Zone, Southern Marmara Region, Turkey", *Geodinamica Acta*, Vol. 28, No. 4, pp. 347–362, 2016.

84. Doğru, A., "Deformation of Eastern Turkey from seismic and geodetic strain rates", *Scientific Research and Essays*, Vol. 5, No. 9, 2010.

85. Yavaşoğlu, H., E. Tarı, and F. Masson, "Slip Partition on the North Anatolian Fault and Its Splays in Central Anatolia Using GPS Data", in *FIG Congress 2010 Facing the Challenges – Building the Capacity*, 2010.

86. Tatar, O., F. Poyraz, H. Gürsoy, Z. Çakır, S. Ergintav, Z. Akpınar, F. Koçbulut, F. Sezen, T. Türk, K. Ö. Hastaoğlu, A. Polat, B. L. Mesci, Ö. Gürsoy, İ. E. Ayazlı, R. Çakmak, A. Belgen, and H. Yavaşoğlu, "Crustal deformation and kinematics of the

eastern part of the North Anatolian Fault Zone (Turkey) from GPS measurements", *Tectonophysics*, Vol. 518-521, pp. 55–62, 2012.

87. Walters, R. J., B. Parsons, and T. J. Wright, "Constraining crustal velocity fields with insar for eastern Turkey: Limits to the block-like behavior of Eastern Anatolia", *Journal of Geophysical Research: Solid Earth*, Vol. 119, No. 6, pp. 5215–5234, 2014.

88. Çakır, Z., S. Ergintav, A. M. Akoglu, E. Cetin, M. Meghraoui, and R. E. Reilinger, "Onset and Mechanisms of Surface Creep on Strike Slip Faults: Clues from the North Anatolian Fault and Comparisons with the San Andreas Fault", Vol. 2014, 2014.

89. Yavasoglu, H., E. Tari, H. Karaman, M. Sahin, O. Baykal, T. Erden, S. Bilgi, G. Ruzgar, C. D. Ince, S. Ergintav, R. Çakmak, U. Tari, and O. Tuysuz, "GPS measurements along the North Anatolian Fault Zone on the mid-anatolia segment", *International Association of Geodesy Symposia*, pp. 166–171, 2006.

90. Ahadov, B., and S. Jin, "Slip rates and seismic potential along main faults in the eastern Mediterranean and Caucasus from dense GPS observations and seismic data", *Pure and Applied Geophysics*, Vol. 178, No. 1, pp. 39–54, 2021.

91. Kozaci, O., J. Dolan, R. Finkel, and R. Hartleb, "Late holocene slip rate for the North Anatolian Fault, Turkey, from Cosmogenic 36Cl geochronology: Implications for the constancy of fault loading and strain release rates", *Geology*, Vol. 35, No. 10, p. 867, 2007.

92. Zabcı, C., T. Sançar, M. Yazıcı, A. M. Friedrich, and N. Akçar, "Deformation of continental blocks within convergent plates: Anatolia as a case study", 2020.

93. Peyret, M., F. Masson, H. Yavasoglu, S. Ergintav, and R. Reilinger, "Present-day strain distribution across a segment of the central bend of the North Anatolian Fault Zone from a persistent-scatterers insar analysis of the ERS and Envisat Archives", *Geophysical Journal International*, Vol. 192, No. 3, pp. 929–945, 2012.

94. Kaneko, Y., Y. Fialko, D. T. Sandwell, X. Tong, and M. Furuya, "Interseismic deformation and creep along the central section of the North Anatolian Fault (Turkey): Insar observations and implications for rate-and-state friction properties", *Journal of Geophysical Research: Solid Earth*, Vol. 118, No. 1, pp. 316–331, 2013.

95. Çetin, E., Z. Çakır, M. Meghraoui, S. Ergintav, and A. M. Akoglu, "Extent and distribution of aseismic slip on the Ismetpaşa segment of the North Anatolian Fault (Turkey) from persistent Scatterer Insar", *Geochemistry, Geophysics, Geosystems*, Vol. 15, No. 7, pp. 2883–2894, 2014.

96. Straub, C., H.-G. Kahle, and C. Schindler, "GPS and geologic estimates of the tectonic activity in the Marmara Sea Region, NW Anatolia", *Journal of Geophysical Research: Solid Earth*, Vol. 102, No. B12, pp. 27587–27601, 1997.

97. Meade, B. J., "Estimates of seismic potential in the Marmara Sea region from block models of secular deformation constrained by global positioning system measurements", *Bulletin of the Seismological Society of America*, Vol. 92, No. 1, pp. 208–215, 2002.

98. Le Pichon, X., N. Chamot-Rooke, C. Rangin, and A. M. Sengör, "The North Anatolian Fault in the Sea of Marmara", *Journal of Geophysical Research: Solid Earth*, Vol. 108, No. B4, 2003.

99. Ergintav, S., R. E. Reilinger, R. Çakmak, M. Floyd, Z. Çakır, U. Doğan, R. W. King, S. McClusky, and H. Özener, "Istanbul's earthquake hot spots: Geodetic constraints on strain accumulation along faults in the Marmara Seismic Gap", *Geophysical Research Letters*, Vol. 41, No. 16, pp. 5783–5788, 2014.

100. Armijo, R., B. Meyer, A. Hubert, and A. Barka, "Westward propagation of the North Anatolian Fault into the northern Aegean: Timing and Kinematics", *Geology*, Vol. 27, No. 3, p. 267, 1999.

101. Polonia, A., L. Gasperini, A. Amorosi, E. Bonatti, G. Bortoluzzi, N. Çagatay, L. Capotondi, M.-H. Cormier, N. Gorur, C. McHugh, and L. Seeber, "Holocene slip

rate of the North Anatolian Fault Beneath the Sea of Marmara", *Earth and Planetary Science Letters*, Vol. 227, No. 3-4, pp. 411–426, 2004.

102. Diao, F., T. R. Walter, G. Solaro, R. Wang, M. Bonano, M. Manzo, S. Ergintav, Y. Zheng, X. Xiong, and R. Lanari, "Fault locking near Istanbul: Indication of earthquake potential from insar and GPS observations", *Geophysical Journal International*, Vol. 205, No. 1, pp. 490–498, 2016.

103. Grall, C., P. Henry, Y. Thomas, G. K. Westbrook, M. N. Çağatay, B. Marsset, H. Saritas, G. Çifçi, and L. Géli, "Slip rate estimation along the western segment of the Main Marmara Fault over the last 405-490 ka by correlating mass transport deposits", *Tectonics*, Vol. 32, No. 6, pp. 1587–1601, 2013.

104. Karabacak, V., U. Ring, and I. T. Uysal, "The off-fault deformation on the North Anatolian Fault Zone and assessment of slip rate from carbonate veins", *Tectonophysics*, Vol. 795, p. 228633, 2020.

APPENDIX A: HISTORICAL EARTHQUAKE CATALOGUE AND PALEO-SEISMIC OBSERVATIONS

Table A.1. Historical earthquakes along the NAFZ.

Year	**Month**	**Day**	**Lat**	**Lon**	**M**	**I**	M_w **(this study)**	**Rupture Length (km)**	**Ref.**
1236	-	-	39.70	39.50	6.2	-	-	7	[60]
1254	-	-	39.70	39.50	7.5	-	-	131	[60]
1254	-	-	40.00	38.30	7.2	-	-	67	[61]
1265	-	-	40.70	27.40	6.6	-	-	17	[62]
1268	-	-	39.80	40.40	7.4	-	-	105	[63]
1296	6	1	40.50	30.50	7.1	-	-	43	[17]
1308	-	-	39.70	39.50	6.5	-	-	14	[64]
1343	-	-	40.70	27.10	7.0	-	-	34	[17]
1343	10	18	40.90	28.00	7.1	-	-	43	[17]
1354	3	1	40.70	27.00	7.5	-	-	105	[17]
1419	-	-	41.00	34.00	7.5	-	-	131	[64]
1422	-	-	39.70	39.50	6.7	-	-	22	[64]
1437	-	-	40.20	28.20	6.8	-	-	27	[62]
1481	-	-	39.90	40.40	7.7	-	-	205	[17]
1481	-	-	41.00	29.00	6.5	-	-	14	[62]
1490	1	6	40.73	29.98	7.4	-	-	110	[65]
1509	10	14	40.70	28.80	7.5	-	-	95	[65]
1509	-	-	40.90	35.00	7.2	-	-	105	[17]
1556	5	10	40.86	28.41	7.3	-	-	65	[65]
1569	12	13	40.82	27.83	7.3	-	-	60	[65]

Year	**Month**	**Day**	**Lat**	**Lon**	**M**	**I**	M_w **(this study)**	**Rupture Length (km)**	**Ref.**
1625	-	-	40.50	26.40	7.1	-	-	53	[17]
1659	2	17	40.50	26.40	7.3	-	-	55	[65]
1666	11	24	39.74	39.50	7.5	7.5	7.3	131	[16]
1667	6	28	39.75	39.50	-	7.5	7.0	-	[37]
1668	7	3	40.70	31.60	-	8	7.2	-	[37]
1668	7	10	41.30	33.80	-	7	6.7	-	[37]
1668	8	12	40.20	31.90	-	9	7.3	-	[66]
1668	8	15	40.40	32.90	-	8	7.0	-	[66]
1668	8	17	40.50	36.60	8.1	9.5	8.1	480	[66]
1668	8	18	41.20	33.80	-	7	6.7	-	[37]
1672	2	2	41.70	32.40	-	7	7.1	-	[16]
1684	9	14	40.70	35.85	-	7	7.1	-	[16]
1705	8	8	40.20	29.50	-	7	7	-	[16]
1719	5	25	40.68	30.13	7.4	8.5	7.5	110	[65]
1737	3	6	40.10	27.30	-	8	7	50	[67]
1754	9	2	40.80	29.20	-	8.5	6.7	36	[67]
1766	5	22	40.92	28.58	7.3	8.5	7.2	65	[16]
1766	8	5	40.75	27.75	7.4	8.5	7.3	60	[16]
1794	8	5	40.35	29.50	-	8	7.2	-	[16]
1850	4	19	40.10	28.30	-	7	6.8	6	[16]
1855	2	28	40.10	28.70	-	8.5	6.8	59	[16]
1912	8	9	40.65	27.20	7.4	9	7.5	55	[68]
1939	12	26	39.80	39.51	7.9	-	7.7	360	[11]
1942	12	20	40.87	36.47	7.1	-	7.9	50	[11]
1943	11	26	41.05	33.72	7.7	-	7.7	260	[11]

Year	**Month**	**Day**	**Lat**	**Lon**	**M**	**I**	M_w **(this study)**	**Rupture Length (km)**	**Ref.**
1944	2	1	40.90	32.60	7.4	-	7.4	180	[11]
1957	5	26	40.60	31.00	7.0	-	7.0	40	[11]
1967	7	22	40.70	30.70	7.2	-	7.2	80	[11]
1999	8	17	40.70	30.00	7.5	-	7.5	145	[32]
1999	11	12	40.80	31.20	7.1	-	7.1	40	[43]

Table A.2. Paleo-seismic records revealing the 1668 earthquake.

Lon	**Lat**	**Correlation**[2]	**Temporal Window**	**Last Rupture**	**Reference**
40.96	35.86	1668	1495-1850	1943	[67]
39.95	38.98	1668	1520-1960	1939	[69]
39.95	38.98	1668	1650-1960	1939	[69]
39.95	38.98	1668	1670-1960	1939	[69]
40.95	35.80	1668	1438-1787	1943	[70]
40.77	32.03	1668	1650-1730	1944	[71]
40.41	31.33	1668	1681-1938	1944	[71]
39.96	38.94	1668	-	1939	[47]
40.58	30.76	1668	1668-1872	1957-67	[72]
40.58	30.76	1668	1394-1668	1957-67	[72]
40.60	31.25	1668	784-1668	1957-67	[47]
40.67	31.27	1668-67	784-1668	1944	[47]
40.69	31.56	1668-67	784-1668	1944	[47]
40.39	37.35	1668	1618-1778	1939-42	[14]
40.32	37.59	1668-66	1618-1778	1939-43	[14]
40.76	31.11	1719-54	1445-1900	1999	[73]
40.70	29.87	1719-54-66	1668-1894	1999	[56]
40.70	29.87	1719-54-66	1620-1680	1999	[56]
40.70	30.40	1719	1668-1947	1999	[74]
37.85	27.93	1653	1488-1668	1999	[74]
40.47	31.21	1668	1394-1782	1967	[75]
40.39	37.47	1668	1580-1720	1939	[71]
40.98	33.50	1668	1495-1850	1943-44	[46]
40.75	36.47	1668	1409-1803	1942	[76]
40.50	30.28	1668	1488-1788	1957-67	[74]
40.58	30.71	1668	1630-1670	1957-67	[74]

[2]Identified historical earthquake

Lon	**Lat**	**Correlation**	**Temporal Window**	**Last Rupture**	**Reference**
39.86	39.61	1668	1305-1670	1939	[74]
40.8	32.55	1668	-	1944	[77]
40.82	32.33	1668	1640-1668	1944	[31]
40.82	32.34	1668	1171-1668	1944	[74]
41.02	35.64	1668	-	1943	[70]
40.82	32.33	1668	1640-1668	1944	[13]
40.63	36.86	1668	1640-1668	1942	[13]
41.27	32.70	1668	-	1944	[78]
40.03	38.63	1668	1408-1804	1939	[78]
40.04	38.60	1668	1650-1668	1939	[79]

Table A.3. Paleo-seismic records revealing the penultimate earthquake cycle.

Lon	**Lat**	**Correlation**[3]	**Temporal Window**	**Last Rupture**	**Reference**
40.96	35.86	-	1292-1401	1943	[67]
40.96	35.86	-	1327-1485	1943	[67]
40.96	35.86	1254	1300-1660	1939	[69]
39.95	38.98	1254	1330-1490	1939	[69]
40.61	26.89	1719-1879	1542-1634	1999	[56]
40.70	29.87	1754-19-1509	1350-1950	1999	[56]
40.95	35.80	-	1302-1482	1939	[70]
40.03	38.63	-	1227-1388	1939	[78]
40.03	38.63	-	1337-1440	1939	[78]
40.03	38.63	-	1324-1428	1939	[78]
40.03	38.63	-	1305-1413	1939	[78]
40.03	38.63	-	1189-1280	1939	[78]
40.58	30.76	-	1220-1410	1957-67	[72]
40.58	30.76	-	1394-1668	1957-67	[72]
40.32	37.59	-	1423-1523	1939-1942	[14]
40.32	37.59	-	1582-1591	1939-1942	[14]
40.32	37.59	-	1415-1451	1939-1942	[14]
40.76	31.11	-	1495-1700	1999	[73]
40.47	31.21	-	1217-1408	1967	[75]
40.47	31.21	-	1440-1632	1967	[75]
40.39	37.47	-	1418-1419	1939	[71]
40.39	37.47	1254	-	1939	[71]
40.98	33.50	1254	1495-1850	1943	[46]
40.61	26.89	1766-1509	1409-1529	1999	[46]
39.86	39.61	-	1305-1670	1939	[70]
40.82	32.34	-	1171-1668	1944	[70]

[3]Identified historical earthquake

Lon	**Lat**	**Correlation**	**Temporal Window**	**Last Rupture**	**Reference**
40.77	27.28	1766	1429-1766	1912	[80]
40.77	27.28	1766	1311-1397	1912	[80]
40.61	26.89	1509	1381-1451	1912	[46]
40.58	30.71	-	1480-1690	1957-67	[80]
40.70	28.20	1343	1220-1550	1999	[81]
40.50	29.40	1509	1450-1670	1999	[81]
40.70	28.20	1343	1029-1411	1999	[70]
40.90	32.80	1254	1027-1428	1939	[70]
40.60	26.80	1509	1357-1548	1999	[70]
40.70	30.40	1567	1480-1651	1999	[74]
40.78	31.33	-	1400-1800	1999	[82]
39.94	27.32	-	1320-1410	1999	[83]

APPENDIX B: GPS VELOCITIES

Table B.1. GPS velocities.

Lon	**Lat**	**v_e (mm/y)**	**v_n (mm/y)**	**S_ve**	**S_vn**	**Rho**	**Site**	**Ref.**
26.380	40.918	-2.38	0.38	0.14	0.13	0	IPSA	[23]
26.373	38.304	-20.21	-19.84	0.14	0.13	0.001	CESM	[23]
26.386	40.921	-18.81	-6.87	7.67	7.62	0	IPS1	[23]
26.414	40.111	-27.95	-2.7	0.79	1.02	-0.012	CANA	[23]
26.551	41.677	-1.51	3.62	0.31	1.16	0	EDIR	[23]
26.686	39.311	-20.75	-10.04	0.21	0.12	0	AYVL	[23]
27.082	38.395	-22.95	-14.82	0.14	0.12	0	IZMI	[23]
27.960	37.629	-21.18	-18.46	0.13	0.14	0.001	CINC	[23]
27.218	41.738	-0.65	0.84	0.11	0.17	0.002	KIRL	[23]
27.242	39.936	-22.71	-3.64	0.83	0.89	-0.016	YENC	[23]
27.269	37.372	-19.77	-22.85	0.13	0.12	0.002	DIDI	[23]
27.497	40.958	-1.75	-1.15	0.12	0.15	0	TEKR	[23]
27.587	40.611	-18.07	-4.31	0.13	0.14	0	MADT	[23]
27.672	39.106	-22.61	-8.61	0.17	0.14	0	KIKA	[23]
27.692	36.709	-13.15	-25.1	0.43	0.53	-0.002	DATC	[23]
27.808	40.393	-18.54	-3.85	0.17	0.16	0.001	ERDT	[23]
27.838	37.841	-21.42	-14.91	0.16	0.15	0	AYD1	[23]
27.894	39.639	-21.78	-4.21	0.19	0.15	0	BALK	[23]
27.916	41.443	-1.01	0.56	0.13	0.12	0	SARY	[23]
27.962	40.967	-0.92	2.36	0.12	0.13	0.001	MER1	[23]
27.975	40.349	-24.58	-2.38	0.73	1.16	0	BAN1	[23]
27.997	40.331	-19.74	-4.02	0.12	0.24	-0.001	BAND	[23]
28.01	38.962	-23.5	-7.43	0.18	0.15	0	AKHI	[23]
28.124	38.483	-25.24	-9.14	0.13	0.15	0.002	SALH	[23]
28.333	40.265	-20.78	-2.44	0.13	0.11	0	KART	[23]

Lon	**Lat**	**v_e (mm/y)**	**v_n (mm/y)**	**S_ve**	**S_vn**	**Rho**	**Site**	**Ref.**
28.364	37.216	-18.93	-17.22	0.18	0.28	0.001	MUGL	[23]
28.648	39.035	-23.49	-6.02	0.13	0.14	0	DEIR	[23]
28.683	41.347	-0.61	0.32	0.13	0.13	0	KARB	[23]
28.724	40.989	-4.72	-0.11	0.55	0.5	-0.005	AVCT	[23]
28.782	40.534	-17.87	-1.72	0.16	0.18	-0.002	BOZT	[23]
28.832	40.991	-1.71	1.15	0.17	0.14	0	ISTN	[23]
28.994	38.505	-23.04	-6.81	0.13	0.16	0.001	ESME	[23]
29.015	40.214	-22.51	-2.35	0.24	0.18	0	BURS	[23]
29.019	41.104	-30.18	-7.27	0.12	0.12	0	ISTA	[23]
29.061	41.061	-0.44	0.02	0.17	0.18	-0.018	KANT	[23]
29.69	37.156	-16.94	-7.16	0.16	0.3	0	CAVD	[23]
29.092	37.762	-21.28	-10.47	0.41	0.58	0	DENI	[23]
29.118	40.852	-3.18	1.6	0.12	0.24	-0.001	BAD1	[23]
29.124	36.626	-14.79	-14.49	0.13	0.26	0.001	FETH	[23]
29.131	40.098	-22.82	-2.49	0.17	0.15	-0.001	ULUT	[23]
29.135	37.41	-19.57	-11.56	0.31	0.2	-0.002	TVAS	[23]
29.153	39.678	-23.11	-2.37	0.41	0.18	0	HARC	[23]
29.372	40.566	-19.93	-0.62	0.35	0.15	-0.001	DUM2	[23]
29.405	38.679	-22.56	-7.04	0.17	0.3	0	USAK	[23]
29.451	40.787	-5.61	-0.07	0.15	0.15	0	TUBI	[23]
29.601	41.169	-0.49	-2.41	0.25	1.39	0	SLEE	[23]
29.689	37.159	-17.69	-8.69	0.25	0.38	-0.001	CAV1	[23]
29.811	36.789	-14.97	-7.24	0.19	0.37	0	ELMI	[23]
29.899	39.481	-22.73	-2.58	0.13	0.15	0	KUTA	[23]
29.951	40.802	-5	-2.1	0.1	0.1	0	IZMT	[24]
29.951	40.802	-5.26	-0.29	0.15	0.14	0	IZMT	[23]
29.962	40.846	-2.65	0.56	0.28	0.28	-0.001	UCG2	[23]

Lon	**Lat**	**v_e (mm/y)**	**v_n (mm/y)**	**S_ve**	**S_vn**	**Rho**	**Site**	**Ref.**
29.977	40.141	-22.8	-4.3	0.1	0.1	0	BILE	[24]
29.977	40.141	-23.13	-2.17	0.12	0.13	0	BILE	[23]
30.3	40.78	-8.461	1.885	1	1	0	0042	[21]
30.05	39.88	-23.79	-3.035	1.13	1.22	0	BOZU	[21]
30.13	40.745	-8.325	-0.257	0.89	0.92	0	SISL	[21]
30.13	40.745	-8.328	-0.201	0.8	0.83	0	SISL	[21]
30.026	40.465	-16.62	-1.280	0.66	0.61	0	MEKE	[21]
30.026	40.465	-16.62	-1.224	0.59	0.55	0	MEKE	[21]
30.32	40.61	-16.58	-1.020	1	1	0	0041	[21]
30.049	39.881	-23.42	-2.63	0.17	0.2	-0.001	BOZU	[23]
30.52	40.35	-16.64	-5.148	1	1	0	0040	[21]
30.57	40.028	-25.95	-1.430	0.3	0.4	0	MHGZ	[21]
30.63	40.65	-11.40	-1.764	1	1	0	0039	[21]
30.67	40.57	-15.52	-0.970	1	1	0	0034	[21]
30.68	40.538	-16.91	-0.212	0.6	0.63	0	AGUZ	[21]
30.71	40.83	-3.88	-0.477	1	1	0	0032	[21]
30.87	40.58	-14.04	-3.299	1	1.5	0	0028	[21]
30.96	40.6	-11.54	-1.411	1	1	0	0026	[21]
30.134	40.69	-12.8	0.471	0.71	0.73	0	SMAS	[21]
30.134	40.69	-12.79	0.414	0.79	0.81	0	SMAS	[21]
30.146	36.302	-9.74	-4.81	0.17	0.25	0	FINI	[23]
30.166	38.069	-20.35	-4.98	0.14	0.15	0.001	DINA	[23]
30.387	39.431	-21.88	0.587	0.6	0.8	0	TRMN	[21]
30.387	39.431	-22.57	-0.726	1.35	1.67	0	TRMN	[21]
30.404	40.88	-12.05	-6.118	0.8	0.9	0	CLTK	[21]
30.464	39.746	-23.1	-4.2	0.1	0.1	0	ESKS	[24]
30.464	39.746	-23.16	-2.28	0.13	0.12	0.001	ESKS	[23]

Lon	**Lat**	**v_e (mm/y)**	**v_n (mm/y)**	**S_ve**	**S_vn**	**Rho**	**Site**	**Ref.**
30.468	38.534	-21.5	-3.72	0.15	0.14	-0.001	SHUT	[23]
30.561	38.738	-21.37	-2.71	0.17	0.2	-0.001	AFYN	[23]
30.567	37.785	-19.8	-5.37	0.24	0.12	0	ISPT	[23]
30.617	39.26	-21.71	-3.235	1	1.2	0	KRCT	[21]
30.617	39.26	-23.74	-5.880	1.83	2.16	0	KRCT	[21]
30.637	39.658	-23.70	-1.407	0.81	0.74	0	ESKI	[21]
30.637	39.658	-23.94	-1.321	0.87	0.81	0	ESKI	[21]
30.637	39.658	-27.08	-1.836	0.4	0.5	0	ESKI	[21]
30.638	40.614	-13.47	-0.850	0.57	0.58	0	KTOP	[21]
30.638	40.614	-13.47	-0.791	0.51	0.52	0	KTOP	[21]
30.655	40.628	-13.42	-0.911	0.57	0.58	0	KKAP	[21]
30.655	40.628	-13.42	-0.852	0.51	0.52	0	KKAP	[21]
30.666	36.888	-12.96	-4.45	0.13	0.11	0.002	ANTL	[23]
30.679	40.552	-16.90	-0.272	0.67	0.7	0	BOZS	[21]
30.679	40.552	-16.90	-0.212	0.6	0.63	0	BOZS	[21]
30.718	37.321	-15.58	-4.64	0.13	0.12	0.002	BCAK	[23]
30.741	40.795	-5.87	-0.03	0.2	0.25	-0.001	HEND	[23]
30.741	40.795	-6	-2.2	0.1	0.1	0	HEND	[24]
30.745	40.652	-11.06	1.464	0.99	1.01	0	KMAL	[21]
30.745	40.652	-11.06	1.524	0.89	0.91	0	KMAL	[21]
30.761	40.589	-12.96	-0.788	0.78	0.79	0	AGOK	[21]
30.761	40.589	-12.96	-0.728	0.7	0.71	0	AGOK	[21]
30.804	40.386	-19.46	-1.431	0.57	0.57	0	TEBA	[21]
30.804	40.386	-19.46	-1.491	0.63	0.63	0	TEBA	[21]
30.827	40.735	-7.847	-0.172	0.73	0.74	0	KDER	[21]
30.827	40.735	-7.849	-0.111	0.66	0.67	0	KDER	[21]

Lon	**Lat**	**v_e (mm/y)**	**v_n (mm/y)**	**S_ve**	**S_vn**	**Rho**	**Site**	**Ref.**
30.862	40.555	-17.11	0.256	0.86	0.87	0	PINA	[21]
30.862	40.555	-17.10	0.196	0.96	0.97	0	PINA	[21]
30.916	40.118	-28.47	-1.159	0.3	0.4	0	CMLN	[21]
31	40.58	-14.15	-2.917	1	1	0	0025	[21]
31.01	40.58	-12.75	-2.819	1.5	1.5	0	0024	[21]
31.02	40.57	-13.45	0.481	2.5	3.5	0	0021	[21]
31.02	40.57	-14.85	-1.620	1	1	0	0022	[21]
31.02	40.58	-12.95	-3.620	1	1	0	0023	[21]
31.05	40.55	-15.05	-1.124	1	1	0	0020	[21]
31.24	40.52	-17.77	-3.551	1	1	0	0019	[21]
31.26	40.6	-11.76	-1.053	1	1	0	0018	[21]
31.34	40.76	-7.651	0.136	1	1	0	0017	[21]
31.43	38.369	-21.48	-4.17	0.34	0.13	0	AKHR	[23]
31.46	40.148	-25.50	1.796	0.2	0.3	0	NALL	[21]
31.49	39.87	-24.03	-1.220	0.89	0.87	0	MIHA	[21]
31.52	40.66	-14.18	-1.591	1	1	0	0015	[21]
31.67	40.55	-15.91	-4.712	1	1	0	0014	[21]
31.68	40.83	-5.87	0.387	1.5	2	0	0013	[21]
31.69	40.88	-4.864	0.087	1	1	0	0011	[21]
31.73	38.802	-21.32	-1.84	0.19	0.16	-0.002	YUNA	[23]
31.78	41.45	-12.2	-3.3	1.9	2.1	0	YYLA	[24]
31.81	39.56	-20.46	-2.831	1	1.5	0	0010	[21]
31.144	39.022	-21.94	-1.9	0.13	0.13	0.001	EMIR	[23]
31.261	39.503	-24.44	0.812	0.9	1.2	0	KYMZ	[21]
31.332	40.173	-23.1	-3.2	0.1	0.1	0	NAHA	[24]
31.332	40.173	-23.11	-1.33	0.15	0.12	-0.001	NAHA	[23]
31.438	40.937	-3.314	0.439	0.55	0.53	0	YIGI	[21]

Lon	**Lat**	**v_e (mm/y)**	**v_n (mm/y)**	**S_ve**	**S_vn**	**Rho**	**Site**	**Ref.**
31.438	40.937	-3.317	0.502	0.5	0.48	0	YIG2	[21]
31.495	39.871	-20.83	0.693	0.3	0.4	0	MIHX	[21]
31.495	39.871	-23.04	-1.23	0.15	0.12	0	MIHA	[23]
31.535	39.445	-22.8	-3.6	0.1	0.2	0	SIHI	[24]
31.535	39.445	-22.59	-1.77	0.15	0.15	-0.001	SIHI	[23]
31.536	39.447	-22	-0.88	0.4	0.38	0.009	SIH1	[23]
31.536	39.447	-22.8	-3.6	0.1	0.2	0	SIH1	[24]
31.602	40.734	-12.8	-0.2	0.1	0.1	0	BOLU	[24]
31.602	40.734	-13.02	1.66	0.13	0.21	-0.001	BOLU	[23]
31.726	38.82	-21.25	-2.22	0.15	0.23	0	YUNK	[23]
31.747	37.677	-16.61	-2.1	0.13	0.14	0.001	BEYS	[23]
31.778	41.45	-0.32	0.38	0.17	0.23	0.001	ZONG	[23]
31.788	37.048	-12.38	-2.51	0.24	0.41	-0.002	AKSI	[23]
31.814	39.564	-20.43	-1.960	0.71	0.61	0	SIVR	[21]
31.814	39.564	-20.47	-2.040	0.64	0.53	0	SIVR	[21]
31.814	39.564	-21.17	-1.934	0.2	0.3	0	SIVR	[21]
32.1	40.65	-16.63	-3.272	1	1	0	0006	[21]
32.1	40.77	-13.71	-0.672	1	1	0	0007	[21]
32.5	39.43	-16.6	-2.5	2	2.3	0	DVBY	[24]
32.5	40.81	-17.6	-2.3	1.9	2.1	0	EREN	[24]
32.05	40.8	-8.906	-0.966	1	1	0	0009	[21]
32.06	40.98	-2.98	1.134	1	1	0	0008	[21]
32.6	40.9	-14.9	-2.5	2	2	0	HMMP	[24]
32.15	40.8	-11.11	-0.780	1	1	0	0005	[21]
32.18	40.79	-12.22	-1.584	1	1	0	0004	[21]
32.24	39.099	-23.14	1.132	0.9	1.1	0	YEME	[21]
32.24	39.099	-24.05	0.947	0.55	0.58	0	YEME	[21]

Lon	**Lat**	**v_e (mm/y)**	**v_n (mm/y)**	**S_ve**	**S_vn**	**Rho**	**Site**	**Ref.**
32.48	40.49	-6.8	-1	2.1	2.4	0	BYYY	[24]
32.57	40.95	-11.5	1.6	2.3	2.6	0	IMLR	[24]
32.57	40.881	-6.465	0.509	0.75	0.69	0	ISME	[21]
32.57	40.881	-6.467	0.578	0.68	0.62	0	ISME	[21]
32.72	41.85	-8.2	-1.7	2	2.3	0	SLYE	[24]
32.76	39.89	-7.8	1.1	1.7	1.9	0	BDRG	[24]
32.85	39.86	-19.2	-0.4	3.5	3.7	0	CGCS	[24]
32.85	40.83	-6.1	-0.7	1.5	1.8	0	BYKY	[24]
32.97	40.81	-6.6	0.2	2.1	2.5	0	KVKK	[24]
32.226	41.52	-5.161	11.848	0.87	0.86	0	HALI	[21]
32.349	40.018	-24.97	0.623	0.5	0.6	0	AYAS	[21]
32.421	40.236	-23.36	0.618	0.3	0.3	0	GUDU	[21]
32.475	40.491	-21.1	-3	0.1	0.1	0	CMLD	[24]
32.475	40.491	-21.14	-1.47	0.13	0.12	-0.001	CMLD	[23]
32.476	37.859	-26.46	11.62	1.51	1.69	-0.001	KNY1	[23]
32.496	39.435	-20.9	-2.7	0.1	0.1	0	HYMN	[24]
32.496	39.435	-20.80	-0.365	1.352	1.328	0	HYMN	[21]
32.496	39.435	-21.13	-0.61	0.19	0.13	-0.001	HYMN	[23]
32.505	38.022	-20.17	1.26	1.53	1.58	-0.01	KNYA	[23]
32.577	39.869	-23.20	0.805	0.3	0.3	0	MESE	[21]
32.617	36.697	-11.85	5.31	0.33	2.21	0	SARV	[23]
32.652	40.871	-15.20	-1.429	0.39	0.43	0	ISP1	[21]
32.654	40.875	-7.691	0.461	0.42	0.48	0	ISP2	[21]
32.658	40.874	-7.871	-0.260	0.41	0.46	0	ISP3	[21]
32.659	40.868	-14.99	-1.060	0.51	0.61	0	ISP6	[21]
32.664	40.874	-8.091	0.801	0.51	0.59	0	ISP4	[21]
32.676	41.232	-2.3	0.1	0.1	0.1	0	KRBK	[24]

Lon	**Lat**	**v_e (mm/y)**	**v_n (mm/y)**	**S_ve**	**S_vn**	**Rho**	**Site**	**Ref.**
32.676	41.232	-2.09	1.7	0.13	0.16	-0.002	KRBK	[23]
32.718	41.846	-0.88	2	0.13	0.13	-0.001	KURU	[23]
32.756	40.322	-24.78	-0.611	0.2	0.3	0	PAZR	[21]
32.758	39.887	-24.17	-1.411	0.488	0.561	0	ANKR	[21]
32.759	39.887	-22.47	-0.26	0.18	0.23	-0.001	LDML	[23]
32.812	39.66	-25.48	1.454	0.68	0.72	0	AYAG	[21]
32.812	39.66	-26.53	-0.315	0.3	0.3	0	AYAG	[21]
32.846	39.856	-21.84	1.02	0.19	0.21	-0.002	ANRK	[23]
32.846	39.856	-22.1	-0.5	0.1	0.1	0	ANRK	[24]
32.865	36.069	-9.61	1.81	0.19	0.13	0.002	ANMU	[23]
32.922	38.65	-19.26	1.41	0.17	0.32	0	CIHA	[23]
32.989	35.201	-5.87	2.07	0.45	0.27	0	GYUR	[23]
33.12	41.03	-10.1	-1.1	2.1	2.5	0	SRKY	[24]
33.18	40.97	-15.5	2.8	2	2.4	0	CYLC	[24]
33.22	37.193	-12.77	4.33	0.26	0.23	0	KAMN	[23]
33.26	40.93	-13.4	-5.8	1.8	2.1	0	HMSL	[24]
33.61	40.609	-19.4	0.5	0.1	0.1	0	CANK	[24]
33.61	40.609	-19.19	1.87	0.27	0.37	0	CANK	[23]
33.62	40.614	-20.37	2.322	0.92	0.94	0	CNKR	[21]
33.065	39.079	-19.05	1.74	0.15	0.24	0	KLUU	[23]
33.101	40.246	-22.91	1.862	0.3	0.3	0	CBUK	[21]
33.256	39.238	-22.99	5.351	0.2	0.3	0	PASD	[21]
33.294	40.484	-19.91	0.747	0.3	0.3	0	SBNZ	[21]
33.353	35.195	-6.14	4.15	0.15	0.14	0.002	LEFK	[23]
33.405	39.942	-22.65	5.038	0.4	0.5	0	IRMA	[21]
33.518	39.843	-20.46	1.75	0.2	0.32	0	KKAL	[23]
33.527	37.715	-14.47	6.34	1.35	0.73	0	KAPN	[23]

Lon	**Lat**	**v_e (mm/y)**	**v_n (mm/y)**	**S_ve**	**S_vn**	**Rho**	**Site**	**Ref.**
33.553	40.713	-18.7	0.6	0.7	0.9	-0.090	KORG	[22]
33.558	41.208	-2.766	0.847	0.66	0.63	0	IHGZ	[21]
33.558	41.208	-2.8	1.3	0.7	0.6	-0.078	IHGZ	[22]
33.610	40.609	-18.5	0.6	0.2	0.2	0.013	CANK	[22]
33.620	40.614	-20.4	2.7	0.9	0.9	-0.100	CNKR	[22]
33.668	40.905	-13.4	1.3	1.0	1.2	-0.160	ILGZ	[22]
33.703	40.163	-22.46	3.915	0.4	0.6	0	AYRN	[21]
33.703	40.163	-22.6	3.6	0.4	0.6	-0.182	SULA	[22]
33.706	41.635	-0.5	2.9	0.7	0.9	-0.100	SLGM	[22]
33.711	41.021	-10.8	6.4	1.1	1.3	-0.130	MULM	[22]
33.743	41.930	-0.1	3.7	0.5	0.7	-0.120	INBO	[22]
33.751	41.101	-6.0	3.9	1.1	1.4	-0.120	BOST	[22]
33.759	41.322	-3.1	4.5	0.7	0.9	-0.050	KUMR	[22]
33.763	41.979	-1.42	4.68	0.31	0.66	-0.007	INE1	[23]
33.763	41.979	-16.77	9.86	1.81	0.75	-0.001	INEB	[23]
33.763	41.979	0.0	-5.7	2.8	3.2	-0.064	INE1	[22]
33.776	41.371	-1.9	0.6	0.1	0.1	0	KSTM	[24]
33.776	41.371	-2.34	2.48	0.44	0.26	-0.001	KSTM	[23]
33.776	41.371	-0.8	2.1	0.2	0.2	-0.037	KSTM	[22]
33.786	41.217	-2.1	2.7	0.6	0.7	-0.110	KAYI	[22]
33.788	40.439	-19.95	2.408	0.5	0.6	0	DDKY	[21]
33.843	39.084	-22.75	5.803	0.4	0.5	0	UZUN	[21]
33.907	35.146	-6.01	5.63	0.19	0.15	0.001	MGOS	[23]
33.936	36.382	-9.8	3.22	0.26	0.14	0.001	SILF	[23]
33.998	38.37	-18.16	4.37	0.13	0.15	0	AKSR	[23]
34.78	40.888	-15.38	3.888	0.83	0.93	0	DDRG	[21]
34.155	39.165	-19.69	3.21	0.25	0.19	0	KIRS	[23]

Lon	**Lat**	**v_e (mm/y)**	**v_n (mm/y)**	**S_ve**	**S_vn**	**Rho**	**Site**	**Ref.**
34.183	37.445	-13.39	4.99	0.13	0.19	0.003	HALP	[23]
34.195	35.537	-8.01	4.56	0.21	0.2	0	DIPK	[23]
34.256	36.566	-22.13	-11.4	1.39	0.19	-0.001	MERS	[23]
34.272	41.031	-13.20	2.693	1.09	1.26	0	ORTC	[21]
34.272	41.031	-13.2	3.2	1.1	1.3	-0.084	ORTC	[22]
34.369	40.154	-20.02	3.42	0.13	0.16	0	SUNL	[23]
34.369	40.154	-20.4	2.4	0.1	0.1	0	SUNL	[24]
34.369	40.154	-19.9	3.3	0.2	0.3	-0.033	SUNL	[22]
34.379	40.155	-21.72	3.323	0.7	0.67	0	SNGR	[21]
34.379	40.155	-21.6	3.8	0.7	0.7	-0.094	SNGR	[22]
34.408	39.574	-20.15	6.159	0.3	0.4	0	CICE	[21]
34.422	41.150	-7.6	-2.6	1.8	2.3	-0.141	KRGI	[22]
34.458	40.439	-20.09	4.256	0.3	0.4	0	UGRL	[21]
34.458	40.439	-20.1	4.0	0.3	0.4	-0.096	UGRL	[22]
34.593	37.961	-15.11	5.16	0.13	0.12	0.001	NGDE	[23]
34.603	36.781	-11.68	4.73	0.21	0.17	0.001	MRSI	[23]
34.679	37.959	-15.14	5.27	0.15	0.16	0.001	NIGD	[23]
34.688	39.303	-22.49	7.737	0.5	0.6	0	KAHA	[21]
34.703	38.617	-17.36	5.2	0.15	0.12	0	NEVS	[23]
34.707	41.022	-11.70	1.444	0.83	0.92	0	OSMC	[21]
34.707	41.022	-11.7	1.9	0.8	0.9	-0.087	OSMC	[22]
34.780	40.888	-15.3	4.4	0.8	0.9	-0.104	DDRG	[22]
34.797	41.461	-2.5	-0.1	0.1	0.1	0	BOYT	[24]
34.797	41.461	-2.18	0.79	0.17	0.18	-0.002	BOYT	[23]
34.797	41.461	-1.7	0.7	0.2	0.2	-0.035	BOYT	[22]
34.798	39.781	-19.33	4.65	0.15	0.12	0	YZGT	[23]
34.803	39.106	-18.7	5.792	0.3	0.3	0	ABDI	[21]

Lon	**Lat**	**v_e (mm/y)**	**v_n (mm/y)**	**S_ve**	**S_vn**	**Rho**	**Site**	**Ref.**
34.803	39.106	-19.41	7.128	0.2	0.2	0	ABDI	[21]
34.813	39.801	-20.76	5.428	0.1	0.1	0	YOZG	[21]
34.813	39.801	-20.82	5.012	0.27	0.27	0	YOZG	[21]
34.813	39.801	-18.8	5.4	0.7	0.6	0.005	YOZG	[22]
34.813	39.801	-20.8	5.2	0.1	0.1	-0.097	YOZG	[22]
34.814	40.145	-19.89	3.205	0.93	1.03	0	ALA1	[21]
34.814	40.145	-20.14	4.629	0.3	0.4	0	ALAC	[21]
34.814	40.145	-19.8	3.7	0.9	1.0	-0.084	ALAC	[22]
34.814	40.145	-20.2	4.4	0.3	0.4	-0.139	ALAC	[22]
34.816	39.824	-19.72	4.52	0.16	0.13	0	YOZT	[23]
34.816	39.824	-19.2	4.1	0.2	0.2	-0.036	YOZT	[22]
34.872	37.422	-13.03	5.24	0.13	0.14	-0.003	POZA	[23]
34.875	40.453	-17.75	4.881	0.94	0.91	0	KKIR	[21]
34.875	40.453	-18.52	5.023	0.2	0.2	0	KKIR	[21]
34.875	40.453	-17.6	4.8	0.9	0.9	-0.016	KKIR	[22]
34.881	41.264	-2.3	3.5	0.7	0.9	-0.140	YAYL	[22]
34.982	40.57	-16.84	3.99	0.14	0.24	-0.001	CORU	[23]
34.982	40.57	-17.2	3.1	0.1	0.1	0	CORU	[24]
34.982	40.570	-17.0	3.8	0.2	0.2	-0.027	CORU	[22]
35.032	39.523	-22.50	7.212	0.4	0.4	0	BTTL	[21]
35.054	40.802	-14.97	4.483	0.86	0.96	0	HMMZ	[21]
35.054	40.802	-14.9	5.0	0.9	1.0	-0.088	HMMZ	[22]
35.83	40.681	-14.33	6.895	0.91	1.02	0	GBAG	[21]
35.87	39.66	-14.4	1.8	2.2	2.6	0	OZBR	[24]
35.113	40.949	-14.00	5.648	1.04	1.15	0	GHAC	[21]
35.113	40.949	-13.9	6.2	1.0	1.2	-0.101	GHAC	[22]
35.154	42.03	-0.7	0.5	0.1	0.1	0	SINP	[24]

Lon	**Lat**	**v_e (mm/y)**	**v_n (mm/y)**	**S_ve**	**S_vn**	**Rho**	**Site**	**Ref.**
35.154	42.03	-0.65	1.67	0.16	0.25	0	SINP	[23]
35.154	42.030	-0.4	1.2	0.2	0.2	-0.017	SINP	[22]
35.166	41.146	-8.093	4.393	1.01	1.2	0	GOL1	[21]
35.166	41.146	-8.0	4.9	1.0	1.2	-0.117	GOL1	[22]
35.205	42.020	0.7	3.1	0.2	0.2	0.000	SINO	[22]
35.205	42.020	-0.6	1.7	0.9	0.8	0.007	SINO	[22]
35.255	39.194	-17.29	5.95	0.16	0.46	-0.001	BOGZ	[23]
35.267	40.272	-19.57	5.993	0.4	0.4	0	ORTK	[21]
35.267	40.272	-19.6	5.7	0.4	0.4	-0.100	ORTK	[22]
35.316	40.666	-15.70	5.160	1.02	1.19	0	GKCB	[21]
35.316	40.666	-15.6	5.7	1.0	1.2	-0.053	GKCB	[22]
35.334	39.723	-20.81	6.888	0.3	0.3	0	SORG	[21]
35.344	37.004	-11.89	-5.13	1.59	2.74	0	ADAN	[23]
35.467	41.138	-4.91	2.93	0.13	0.14	-0.005	VEZI	[23]
35.467	41.138	-5.3	2.1	0.1	0.1	0	VEZI	[24]
35.467	41.138	-4.8	2.7	0.2	0.2	-0.080	VEZI	[22]
35.498	40.077	-18.89	7.277	0.3	0.3	0	CKRK	[21]
35.498	40.077	-18.9	7.0	0.3	0.3	-0.140	CKRK	[22]
35.524	38.708	-16.13	6.22	0.14	0.14	-0.001	KAYS	[23]
35.568	39.102	-19.57	8.771	0.3	0.3	0	FELA	[21]
35.604	40.471	-20.5	2.8	1.0	1.2	-0.154	GYNC	[22]
35.645	40.919	-11.46	6.662	0.99	1.12	0	HVZA	[21]
35.645	40.919	-11.3	7.2	1.0	1.1	-0.105	HVZA	[22]
35.657	39.339	-19.66	8.364	0.4	0.4	0	ATEK	[21]
35.803	39.86	-20.23	7.954	0.3	0.3	0	DOLK	[21]
35.803	39.860	-20.2	7.7	0.3	0.3	-0.077	DOLK	[22]
35.830	40.681	-14.2	7.5	0.9	1.0	-0.077	GBAG	[22]

Lon	**Lat**	**v_e (mm/y)**	**v_n (mm/y)**	**S_ve**	**S_vn**	**Rho**	**Site**	**Ref.**
35.849	40.666	-13.9	6.9	0.2	0.2	-0.080	AMAS	[22]
35.849	40.666	-14.04	6.97	0.16	0.15	-0.005	AMAS	[23]
35.849	40.666	-14.5	6.2	0.1	0.1	0	AMAS	[24]
35.872	39.66	-19.5	5.7	0.1	0.1	0	AKDG	[24]
35.872	39.66	-19.09	6.49	0.14	0.13	-0.001	AKDG	[23]
35.875	40.355	-19.30	8.647	0.4	0.4	0	KRLK	[21]
35.875	40.355	-19.3	8.4	0.4	0.4	-0.099	KRLK	[22]
35.912	37.815	-13.29	7.19	0.16	0.15	0.002	FEEK	[23]
36.2	40.9	-10.6	0.6	2.3	2.6	0	BRBY	[24]
36.2	40.82	-6.4	5.2	1.8	2.1	0	KRBS	[24]
36.17	40.71	-9.1	3.9	1.7	1.9	0	HCGR	[24]
36.18	36.593	-16.97	-5.11	3.68	3.72	-0.014	ISKD	[23]
36.046	41.065	-3.953	4.216	1.1	1.29	0	KVAK	[21]
36.046	41.065	-3.8	4.8	1.1	1.3	-0.097	KVAK	[22]
36.055	39.183	-17.30	9.434	0.3	0.3	0	GMRK	[21]
36.58	39.894	-19.39	9.395	0.3	0.3	0	YLDZ	[21]
36.77	40.68	-4.869	3.857	0.41	0.48	0	PBYL	[21]
36.081	39.185	-19.07	6.32	0.58	0.37	0	GEME	[23]
36.146	36.538	-7.14	11.49	0.36	0.22	-0.001	ISKN	[23]
36.153	36.208	-6.41	10.53	0.16	0.22	0	HATA	[23]
36.156	36.2	-5.79	5.64	3.55	3.79	0.019	HAT1	[23]
36.208	38.261	-17.71	8.15	1.26	0.9	-0.001	TUF1	[23]
36.221	38.261	-13.6	6.75	0.24	0.23	0	TUFA	[23]
36.254	37.102	-11.26	7.83	0.15	0.16	0.002	ONIY	[23]
36.256	41.344	-0.79	-0.17	0.39	0.71	-0.002	SAMN	[23]
36.318	40.136	-19.55	8.615	0.3	0.3	0	TSPN	[21]
36.318	40.136	-19.5	8.4	0.3	0.3	-0.065	TSPN	[22]

Lon	**Lat**	**v_e (mm/y)**	**v_n (mm/y)**	**S_ve**	**S_vn**	**Rho**	**Site**	**Ref.**
36.324	39.553	-18.09	8.615	0.3	0.4	0	AKCK	[21]
36.334	41.309	-1.9	1.3	0.2	0.2	0	SAM1	[24]
36.334	41.309	-1.33	1.99	0.31	0.39	-0.006	SAM1	[23]
36.334	41.309	-1.3	1.2	2.7	3.2	-0.078	SAM1	[22]
36.336	41.299	-4.693	8.360	0.98	0.99	0	SAMS	[21]
36.336	41.299	0.3	2.8	1.0	1.0	0.049	SAMS	[22]
36.479	39.307	-16.52	7.203	0.3	0.4	0	CEML	[21]
36.485	40.617	-16.26	5.547	0.39	0.46	0	KZLU	[21]
36.485	40.617	-16.6	5.5	0.4	0.5	-0.095	KZLU	[22]
36.554	40.237	-17.36	9.798	0.3	0.3	0	CORD	[21]
36.554	40.237	-19.81	7.825	0.25	0.23	0	CRDK	[21]
36.554	40.237	-17.3	9.6	0.3	0.3	-0.032	CORD	[22]
36.554	40.237	-20.1	7.8	0.3	0.2	-0.032	CRDK	[22]
36.557	40.331	-17.74	7.06	0.16	0.15	-0.002	TOKA	[23]
36.557	40.331	-18.4	6.4	0.1	0.1	0	TOK1	[24]
36.557	40.331	-18.21	5.17	1.11	1.88	-0.001	TOK1	[23]
36.580	39.894	-19.3	9.2	0.3	0.3	-0.073	YLDZ	[22]
36.752	40.476	-13.51	7.478	0.45	0.54	0	GKDE	[21]
36.752	40.476	-13.8	7.4	0.5	0.5	-0.097	GKDE	[22]
36.770	40.680	-5.2	3.8	0.4	0.5	-0.090	PBYL	[22]
36.804	40.557	-12.62	5.966	0.48	0.57	0	TALN	[21]
36.804	40.557	-12.9	5.9	0.5	0.6	-0.103	TALN	[22]
36.892	39.797	-18.32	8.36	0.15	0.15	0	SVAS	[23]
36.912	40.447	-19.05	6.822	0.97	1.28	0	ATKY	[21]
36.912	40.447	-15.6	8.4	0.7	0.9	-0.090	ATKY	[22]
36.912	40.447	-19.3	6.8	1.0	1.3	-0.088	ATKY	[22]
36.931	37.581	-10.27	9.37	0.21	0.18	0.001	MARA	[23]

Lon	**Lat**	**v_e (mm/y)**	**v_n (mm/y)**	**S_ve**	**S_vn**	**Rho**	**Site**	**Ref.**
37.001	40.685	-4.592	4.799	0.45	0.55	0	OZDM	[21]
37.001	40.685	-3.7	4.7	0.9	1.0	-0.090	OZDM	[22]
37.001	40.685	-4.9	4.8	0.5	0.6	-0.088	OZDM	[22]
37.003	39.744	-18.8	7	0.1	0.1	0	SIVS	[24]
37.003	39.744	-18.13	7.4	0.14	0.14	0	SIVS	[23]
37.003	39.744	-18.3	7.4	0.2	0.2	-0.034	SIVS	[22]
37.011	39.433	-18.15	9.565	0.3	0.4	0	ULAS	[21]
37.47	39.283	-17.09	10.132	0.3	0.3	0	KVKK	[21]
37.054	40.863	-4.37	11.271	0.43	0.53	0	AKKS	[21]
37.054	40.863	-0.5	-0.1	0.4	0.5	-0.104	AKKS	[22]
37.095	39.786	-18.63	10.559	0.3	0.3	0	SIVA	[21]
37.095	39.786	-19.44	9.307	0.26	0.24	0	SIVA	[21]
37.095	39.786	-18.5	10.3	0.3	0.3	-0.069	SIVA	[22]
37.095	39.786	-19.7	9.3	0.3	0.2	-0.035	SIVA	[22]
37.112	36.709	-7.65	13.64	0.9	0.78	0	KLIS	[23]
37.188	38.059	-13.13	8.62	0.28	0.14	0	EKIZ	[23]
37.265	40.547	-8.217	5.902	0.41	0.48	0	BRKT	[21]
37.265	40.547	-8.5	5.9	0.4	0.5	-0.090	BRKT	[22]
37.308	38.717	-14.69	8.39	0.26	0.15	-0.001	GURU	[23]
37.336	40.385	-10.59	5.62	0.15	0.17	-0.002	RDIY	[23]
37.336	40.385	-11.4	5.1	0.1	0.1	0	RDIY	[24]
37.336	40.385	-10.6	6.1	0.3	0.3	-0.030	RDIY	[22]
37.374	37.065	-6.32	12.57	0.24	0.13	0.001	ANTE	[23]
37.394	39.921	-20.41	6.676	0.45	0.54	0	KSDR	[21]
37.394	39.921	-20.6	6.7	0.5	0.5	-0.090	KSDR	[22]
37.485	41.046	-1.2	1.97	0.56	0.16	-0.001	FASA	[23]
37.485	41.046	-2.2	1.8	0.1	0.1	0	FASA	[24]

Lon	**Lat**	**v_e (mm/y)**	**v_n (mm/y)**	**S_ve**	**S_vn**	**Rho**	**Site**	**Ref.**
37.485	41.046	-0.5	2.3	0.2	0.2	-0.040	FASA	[22]
37.535	40.229	-15.9	7.3	0.8	0.9	-0.070	DOGA	[22]
37.549	40.221	-16.61	8.442	0.41	0.48	0	DOSA	[21]
37.549	40.221	-16.8	8.4	0.4	0.5	-0.085	DOSA	[22]
37.604	40.778	-3.35	9.029	0.26	0.24	0	GURE	[21]
37.604	40.778	-1.5	2.1	0.3	0.2	-0.027	GURE	[22]
37.757	39.867	-16.68	11.411	0.3	0.3	0	TEKK	[21]
37.757	39.867	-17.97	10.835	0.46	0.56	0	TEKK	[21]
37.757	39.867	-16.5	11.2	0.3	0.3	-0.079	TEKK	[22]
37.757	39.867	-18.2	10.8	0.5	0.6	-0.101	TEKK	[22]
37.771	40.463	-3.614	5.685	0.46	0.54	0	MSDY	[21]
37.771	40.463	-3.8	5.7	0.5	0.5	-0.067	MSDY	[22]
37.776	40.400	-3.5	5.7	0.7	0.9	-0.090	DYLI	[22]
37.869	40.313	-6.899	5.572	0.45	0.53	0	IKYK	[21]
37.869	40.313	-7.1	5.6	0.5	0.5	-0.082	IKYK	[22]
37.958	39.454	-16.52	11.297	0.2	0.2	0	SINC	[21]
37.958	39.454	-17.34	10.579	0.5	0.58	0	SINC	[21]
37.958	39.454	-17.34	9.943	0.32	0.32	0	SINC	[21]
37.958	39.454	-17.0	10.0	0.4	0.4	0.001	SINC	[22]
38.23	37.746	-6.85	12.66	0.38	0.14	0	ADIY	[23]
38.067	40.162	-13.90	7.725	0.55	0.68	0	SUSE	[21]
38.067	40.162	-14.1	7.8	0.6	0.7	-0.102	SUSE	[22]
38.075	40.163	-11.97	6.28	0.17	0.2	-0.001	SSEH	[23]
38.075	40.163	-12.8	6.1	0.1	0.1	0	SSEH	[24]
38.075	40.163	-12.1	6.8	0.2	0.2	-0.042	SSEH	[22]
38.104	39.394	-15.3	9.2	0.19	0.17	0	DIVR	[23]
38.104	39.394	-15.3	9.7	0.3	0.3	-0.019	DIVR	[22]

Lon	**Lat**	**v_e (mm/y)**	**v_n (mm/y)**	**S_ve**	**S_vn**	**Rho**	**Site**	**Ref.**
38.121	39.882	-12.52	8.174	0.55	0.69	0	IMRN	[21]
38.121	39.882	-12.7	8.2	0.6	0.7	-0.108	IMRN	[22]
38.217	38.338	-13.42	10.19	0.43	0.14	0	MALY	[23]
38.264	39.178	-16.51	14.800	1.4	1.64	0	DIVR	[21]
38.388	40.923	-0.28	2.19	0.18	0.14	-0.007	GIRS	[23]
38.388	40.923	-1	2.1	0.1	0.1	0	GIRS	[24]
38.388	40.923	-0.5	2.6	0.2	0.2	-0.064	GIRS	[22]
38.425	38.328	-13.31	10.67	0.14	0.22	0.002	MLTY	[23]
38.448	40.316	-4.241	-1.017	0.46	0.55	0	SBKH	[21]
38.448	40.316	-4.4	-1.0	0.5	0.6	-0.087	SBKH	[22]
38.487	39.041	-14.8	9.64	0.26	0.3	-0.001	ARPK	[23]
38.515	39.614	-17.95	8.702	0.48	0.58	0	ILIC	[21]
38.515	39.614	-18.70	11.126	0.41	0.49	0	DIVR	[21]
38.515	39.614	-15.7	11.3	0.4	0.5	-0.113	DIVR	[22]
38.645	39.31	-18.92	11.673	1.61	1.93	0	DBAS	[21]
38.645	39.31	-20.62	10.088	1.37	1.67	0	ILIC	[21]
38.645	39.310	-17.8	10.2	1.4	1.7	-0.085	ILIC	[22]
38.743	39.82	-17.59	10.275	0.45	0.53	0	ARPY	[21]
38.743	40.047	-9.786	0.794	0.51	0.64	0	AYDG	[21]
38.743	39.820	-17.7	10.3	0.5	0.5	-0.082	ARPY	[22]
38.743	40.047	-9.9	0.9	0.5	0.6	-0.088	AYDG	[22]
38.771	39.906	-12.64	5.97	0.13	0.15	0	RHIY	[23]
38.771	39.906	-13.0	6.4	0.2	0.2	-0.035	RHIY	[22]
38.774	39.914	-13.07	6.594	0.44	0.54	0	RFHY	[21]
38.774	39.914	-13.2	6.7	0.4	0.5	-0.081	RFHY	[22]
38.818	37.192	-8.02	13.57	0.18	0.15	0.002	SURF	[23]
38.836	40.136	-3.301	3.371	0.49	0.61	0	KRDK	[21]

Lon	**Lat**	**v_e (mm/y)**	**v_n (mm/y)**	**S_ve**	**S_vn**	**Rho**	**Site**	**Ref.**
38.836	40.136	-3.4	3.4	0.5	0.6	-0.092	KRDK	[22]
38.922	39.059	-17.82	12.853	0.83	0.98	0	DBAS	[21]
38.922	39.059	-15.1	12.9	0.8	1.0	-0.089	DBAS	[22]
38.931	39.026	-14.77	16.752	1.52	1.83	0	CMGK	[21]
38.931	39.026	-17.82	12.851	0.83	0.98	0	CMG1	[21]
38.997	37.175	-25.9	-10.88	0.18	0.2	0	HRRN	[23]
39.006	37.171	-6.23	16.53	0.38	0.27	-0.003	HRN1	[23]
39.42	40.151	-3.613	2.599	0.35	0.38	0	KLKT	[21]
39.42	40.151	-3.794	2.254	0.27	0.26	0	KLKT	[21]
39.164	39.613	-10.09	8.372	0.47	0.57	0	KMAH	[21]
39.164	39.613	-13.50	8.972	0.4	0.51	0	CMGK	[21]
39.164	39.613	-16.42	9.133	0.32	0.32	0	KMAH	[21]
39.164	39.613	-18.7	9.7	0.9	0.9	-0.026	KMAH	[22]
39.217	39.074	-18.22	13.291	1.46	1.74	0	HZAT	[21]
39.217	39.074	-19.41	12.335	1.5	1.86	0	HZAT	[21]
39.217	39.074	-16.7	12.2	1.5	1.9	-0.069	HZAT	[22]
39.256	38.645	-15.15	9.8	0.14	0.14	0.001	ELAZ	[23]
39.258	39.35	-17.99	4.349	1.28	1.59	0	SRTS	[21]
39.258	39.35	-18.53	7.769	1.48	1.79	0	SRTS	[21]
39.329	37.752	-6.34	12.9	0.22	0.31	0.001	SIVE	[23]
39.349	39.762	-12.80	4.026	0.61	0.77	0	BHCL	[21]
39.349	39.762	-12.9	4.1	0.6	0.8	-0.078	BHCL	[22]
39.361	39.902	-3.478	-0.605	0.52	0.64	0	AHMD	[21]
39.361	39.902	-3.6	-0.5	0.5	0.6	-0.090	AHMD	[22]
39.420	40.151	-3.9	2.3	0.3	0.3	-0.034	KLKT	[22]
39.482	39.793	-9.765	1.422	0.52	0.64	0	ER98	[21]
39.482	39.793	-9.9	1.5	0.5	0.6	-0.083	ER98	[22]

Lon	**Lat**	**v_e (mm/y)**	**v_n (mm/y)**	**S_ve**	**S_vn**	**Rho**	**Site**	**Ref.**
39.494	39.652	-14.83	6.002	0.82	1.07	0	BNKC	[21]
39.494	39.652	-14.9	6.1	0.8	1.1	-0.055	BNKC	[22]
39.506	39.746	-10.26	4.88	0.18	0.18	-0.004	ERZI	[23]
39.506	39.746	-11.88	4.78	0.33	0.7	0.002	ERZ1	[23]
39.506	39.746	-12.8	2.7	3.0	3.5	-0.009	ERZ1	[22]
39.516	40.437	0.05	1.33	0.21	0.16	0.002	GUMU	[23]
39.516	40.437	-0.1	2.1	0.2	0.3	0.020	GUMU	[22]
39.524	39.071	-17.97	11.639	1.31	1.16	0	KCMZ	[21]
39.524	39.824	-6.054	-1.206	1.18	1.47	0	TUNC	[21]
39.524	39.824	-6.684	0.819	1.33	1.6	0	KCMZ	[21]
39.546	39.11	-14.16	8.72	0.15	0.29	-0.001	TNCE	[23]
39.593	39.733	-9.771	4.019	0.57	0.73	0	EKSU	[21]
39.593	39.733	-9.9	4.1	0.6	0.7	-0.098	EKSU	[22]
39.688	39.724	-10.61	4.206	0.54	0.67	0	UZUM	[21]
39.688	39.724	-10.7	4.3	0.5	0.7	-0.083	UZUM	[22]
39.711	41.005	0.57	1.61	0.21	0.19	0	TRBN	[23]
39.725	39.582	-11.44	10.205	0.54	0.67	0	CLYN	[21]
39.725	39.582	-11.5	10.3	0.5	0.7	-0.084	CLYN	[22]
39.751	37.234	-5.71	13.84	0.13	0.15	0.003	VIRA	[23]
39.758	38.27	-7.28	14.16	0.27	0.16	0	ERGN	[23]
39.776	40.995	-4.222	8.658	0.372	0.312	0	TRB0	[21]
39.853	39.591	-12.37	8.811	0.54	0.67	0	MUTU	[21]
39.957	39.538	-11.52	3.010	1.52	1.88	0	KTAS	[21]
40.33	39.039	-19.05	7.973	1.96	2.58	0	USVT	[21]
40.038	39.43	-12.08	8.620	3.25	4.24	0	BLYM	[21]
40.079	39.852	-4.988	3.365	0.52	0.65	0	CYRL	[21]
40.187	37.954	-6.73	13.69	0.2	0.22	0.003	DIYB	[23]

Lon	**Lat**	**v_e (mm/y)**	**v_n (mm/y)**	**S_ve**	**S_vn**	**Rho**	**Site**	**Ref.**
40.191	40.25	0.44	1.58	0.19	0.14	-0.001	BAYB	[23]
40.254	39.731	-3.262	5.451	0.6	0.53	0	MRCN	[21]
40.493	41.037	-0.75	1.54	0.62	0.17	-0.001	RZE1	[23]
40.501	38.885	-9.53	10.95	0.22	0.23	0.001	BING	[23]
40.515	39.215	-16.84	5.389	1.62	2.13	0	ATAP	[21]
40.728	37.311	-5.13	13.65	0.18	0.12	0.002	MARD	[23]
40.733	39.182	-14.56	4.742	1.67	2.13	0	KRPR	[21]
40.809	40.437	-4.8	8.052	0.56	0.51	0	ISPI	[21]
41.154	37.864	-5.58	14.15	0.2	0.14	0.001	BTMN	[23]
41.255	39.906	0.87	2.37	0.34	0.13	0	ERZR	[23]
41.357	37.417	-4.95	13.9	0.2	0.12	0.002	MIDY	[23]
41.502	38.793	-11.61	12.11	0.52	1.4	0	MUUS	[23]
41.548	40.531	1.7	1.56	0.2	0.24	-0.004	UDER	[23]
41.696	39.369	0.66	5.51	0.22	0.32	0	HINI	[23]
41.818	41.175	6.5	3.69	0.42	0.23	0	ARTV	[23]
41.936	37.932	-4.58	13.84	0.21	0.21	0	SIRT	[23]
42.29	38.529	-5.85	11.58	0.54	0.43	-0.011	TVAN	[23]
42.167	40.042	2.77	3.57	0.35	0.63	-0.001	HORS	[23]
42.291	38.53	-5.04	11.12	1.23	1.91	0.001	TVA1	[23]
42.457	37.525	-6.74	8.92	0.27	0.32	0.001	SIRN	[23]
42.531	39.143	4.5	6.29	0.71	1.67	0	MALZ	[23]
42.541	39.146	-13.46	2.76	1.46	1.75	-0.005	MLZ1	[23]
42.699	41.111	1.9	1.04	0.23	0.3	0	ARDH	[23]

APPENDIX C: SLIP RATES AND LOCKING DEPTHS ALONG THE NAFZ FROM PREVIOUS STUDIES

Table C.1. Slip rate and locking depth estimations along the NAFZ.

NAFZ Segment	**Slip and/or Creep Rate (mm/y)**	**Locking Depth (km)**	**Method**	**Reference**
Eastern	16 – 24 slip	-	GPS	[84]
Eastern	18.7±1.6 – 21.5±2.1 slip	16	GPS	[85]
Eastern	16.3±2.3 – 24.0±2.9 slip	8.1±3.3 - 12.8±3.9	GPS	[86]
Eastern	22.8±0.4 slip	11.9±3.5 - 19.1±3.4	GPS	[22]
Eastern	6.5 slip	-	Paleo-seismology	[18]
Eastern	17.5±4 slip	-	Paleo-seismology	[14]
Eastern	20±3 slip	18±9	InSar	[87]
Eastern	20±3 slip	7±2	InSar	[88]
Central	20 – 24 slip	-	GPS	[89]
Central	23±2 slip	21	GPS	[4]
Central	15 – 20 slip and 13.2±3.3 creep	-	GPS	[24]
Central	25±0.5 slip	9±3.2	GPS, Seismol-ogy	[90]
Central	12.5±2.5 slip	-	Paleo-seismology	[46]

NAFZ Segment	**Slip and/or Creep Rate (mm/y)**	**Locking Depth (km)**	**Method**	**Reference**
Central	17 – 18.5 slip	-	Paleo-seismology	[18]
Central	20.5±5.5 slip	-	Paleo-seismology	[91]
Central	18.6±3.3 slip	-	Paleo-seismology	[47]
Central	18.9±3 slip	-	Paleo-Seismology	[92]
Central	20 – 23±2 slip	15 – 20	InSar	[93]
Central	20 – 25 slip and 9 creep	5.5 – 7 shallow creep	InSar	[102]
Central	25±1 slip and 8±2 creep	5 shallow creep	InSar	[103]
Western	20±3 - 22±3 slip	-	GPS	[94]
Western	24.4 – 24.8 slip	6—7	GPS	[95]
Western	22.8 slip	13±2	GPS	[96]
Western	24.6 – 27.9 slip		GPS	[4]
Western	15±2 – 25±2 slip	11±2	GPS	[97]
Western	12.7±1.2 creep	-	GPS	[55]
Western	17 – 28 slip	-	GPS, Seismol-ogy	[90]
Western	17- 19 slip	-	Paleo-seismology	[98]

NAFZ Segment	**Slip and/or Creep Rate (mm/y)**	**Locking Depth (km)**	**Method**	**Reference**
Western	17 slip	-	Paleo-seismology	[18]
Western	14 – 20 slip	-	Paleo-seismology	[99]
Western	15 slip	-	Paleo-Seismology	[73]
Western	16.9±1 slip	-	Paleo-Seismology	[92]
Western	18.9±7.2 slip	12.1±7.0	GPS, In-Sar	[100]
Western	25 – 29 slip	20 - 27	GPS, In-Sar	[48]
Western	15.1–19.7 slip	-	Seismology	[101]